Technische Universität München
TUM School of Natural Sciences, Physics Department
Bayerische Akademie der Wissenschaften
Walther-Meißner-Institut für Tieftemperaturforschung

Master's Thesis in Condensed Matter Physics

Microwave Manipulation of Magnon Transport and Spin Pumping

Franz Weidenhiller

11.05.2023

Supervisor: Prof. Dr. Rudolf Gross
Advisors: Dr. Matthias Althammer, Manuel Müller, Janine Gückelhorn

Contents

Chapter 1

Introduction

"If everything you try works, you aren't trying hard enough."

Gordon Moore

This quote by the late Gordon Moore, co-founder of Intel and namesake for the famous Moore's law, who recently passed away aged 94, captures well the spirit of scientific advance, which can only be achieved by trying things, that might not always work from the start. This is even more apparent, when a reliably advancing technology reaches the boundaries imposed by the laws of physics. Moore's law, which predicts a doubling in the transistor count and therefore speed of integrated circuits every two years [Moo06], seems to be coming to an end, as a further miniaturization of the transistors becomes much harder due to the boundaries imposed by the size of atoms and quantum tunneling of electrons [Wal16]. This has sparked an ever growing interest in the field of spintronics, where the use of spin currents for information processing and storage promises to overcome some of the limitations imposed by the usage of charge currents [San+17]. Pure spin currents can be used to transport information without moving electrons in magnetic insulators, enabling devices with lower energy dissipation compared to charge current based electronics [Wim21]. Some recent examples for the realization of operational spintronic devices are the magnon transistor first demonstrated by Chumak et al. in 2014 [CSH14] as well as the implementation of magnetic random access memory, which is already a commercially available product [Bha+17].

Yttrium iron garnet ($Y_3Fe_5O_{12}$, YIG), the magnetic insulator material platform used in this work, has been studied extensively over the past decades [Bra+20] and still remains the material with the lowest damping for spin waves [CKL93; Kli+17]. It thereby enables the transport of spin information across large distances up to millimeters [Cor+15] and the efficient microwave excitation of its magnetization up to the THz-regime [Hen+73; Sei+18]. These properties also render YIG of great interest for research into computing applications, where the modulation of magnon transport between two electrodes is desirable [Gan+16; Cor+18].

This thesis investigates the magnon transport properties of YIG, which have been extensively studied in recent years [Wim+19b; Wim+19a; Güc+20; Güc+21], while modulating the magnonic transport via the dynamic magnetic field of a microwave

antenna. We expand upon the work described in Ref. [Rub21] and the outlook of Ref. [Wim21], by optimizing the device geometry, investigating the magnonic transport in the bulk limit for our YIG thin films and analyzing the magnonic transport over a wide temperature range from 5 K to 280 K. There, we explore, how the magnon transport properties are altered by the additional insulating layer and microwave antenna as compared to previous work [Goe+15; Wim+19a; Rub21]. We observe the manifestation of comb-like features in our microwave magnetic field modulated magnon transport and spin pumping experiments, which can be related to the generation of perpendicular standing spin waves (PSSWs) [Wie+94; Kli+15], enabling the extraction of the spin wave stiffness parameter from magnon transport and spin pumping voltages as a function of temperature.

We start our discussion with a brief introduction to the theoretical background of our experiments in Chapter 2, which is divided into two main parts: (i) first the basics of all-electrical magnon transport is introduced and (ii) second we describe dynamic magnetization effects due to a microwave excitation. We begin by introducing the concept of spin currents and their transport across heavy metal/ferromagnetic insulator interfaces and lateral transport within the ferromagnetic insulator. Following this introduction to all-electrical magnon transport, we turn our focus to the effects of a dynamically excited magnetization by a microwave magnetic driving field. Then, the dispersion relation of spin waves is motivated and the concept of perpendicular standing spin waves is introduced. When the microwave driving power is increased above a certain threshold, parametric pumping effects become relevant. In detail, parallel and perpendicular pumping manifest in the respective driving field geometries. The introduction into the theory is concluded with a discussion of spin angular momentum injection by a dynamically excited magnetization into an adjacent normal metal, which is called spin pumping.

In Chapter 3, the applied experimental techniques and recorded measurement results are discussed. In the beginning, we detail the fabrication processes for our devices and discuss problems with the durability of the devices. Then, the lock-in measurement technique used for the all-electrical magnon transport experiments, is introduced, before discussing the measurement results of angle dependent magnetoresistance (ADMR) measurements. Furthermore, the measurements of the transport voltages, while sweeping the external magnetic field, are discussed. We then turn our attention to field-sweep measurements of the spin pumping voltage, which is induced by the dynamically precessing magnetization in the ferromagnetic insulator. Here, we also analyze results of spin pumping measurements, where a DC charge current bias is simultaneously applied in one of the Pt-strips with the goal of better understanding the influence of transported magnons on the detected spin pumping voltage. Next, we discuss the physical origin of the fine structure, which emerges in the field-sweep measurements of the magnon transport and spin pumping voltages. From this, the spin wave stiffness is extracted as a function of the temperature. Finally, we compare our spin pumping results to those recorded for a structure with a

wider antenna, which enables a more parallel pumping geometry as a stepping stone toward the implementation of a magnon Bose-Einstein condensate.

We conclude this thesis with a summary of the main experimental results in Chapter 4, before giving an outlook on possible starting points for future experiments in Chapter 5.

Chapter 2

Theory

In this chapter we discuss the theoretical background on all-electrical magnon transport in Sec. 2.1 and on magnetization dynamics in Sec. 2.2, which is necessary to understand the experimental results in the following chapters. In the first section, we begin by introducing the concept of (pure) charge and (pure) spin currents in Sec. 2.1.1. Next, we review the mechanism, which converts charge currents into spin currents and vice versa called the (inverse) spin Hall effect in Sec. 2.1.2. Following that, we introduce the theory concerning spin currents across the interface between normal metals and ferromagnetic insulators in Sec. 2.1.3, which leads into the explanation of the physics behind the SHE and Joule-heating induced magnon transport in Sec. 2.1.4. In the second part of this chapter, we present the Karlqvist equations in Sec. 2.2.1, which describe the microwave magnetic field generated by an on-chip microwave antenna. We then discuss, how the microwave fields created by the antenna affect the magnetization dynamics in ferromagnetic insulator layers in Sec. 2.2.2 [Kit48]. Thereafter, we calculate the dispersion relation for dipolar-exchange spin waves (Sec. 2.2.3) [KS86], using the thus obtained dispersion relation to understand the concept of perpendicular standing spin waves (PSSWs). Finally, the parametric pumping process is introduced in Sec. 2.2.4, before finishing our overview of the relevant theory with a discussion of spin pumping from a ferromagnetic insulator into an adjacent normal metal in Sec. 2.2.5

2.1 All-Electrical Magnon Transport

2.1.1 Charge and Spin Currents

In this section, we define the physical concepts of spin currents and charge currents. The electrons, that form the basis for electronic charge currents, not only carry charge, but also spin information. In a simple two spin channel model, we describe a charge current density $\mathbf{j}_c$ as the sum of the charge current densities of electrons with spin up $\mathbf{j}_\uparrow$ and electrons with spin down $\mathbf{j}_\downarrow$ [Cze11]

$$\mathbf{j}_c = \mathbf{j}_\uparrow + \mathbf{j}_\downarrow. \tag{2.1}$$

Charge currents are generated by applying a voltage across an electrical conductor. If the two spin current densities are not equal, the electrons also mediate information
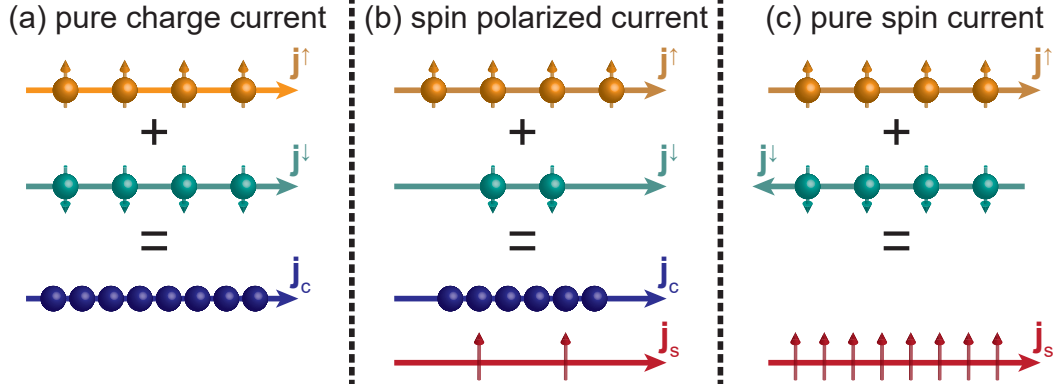
Figure 2.1: The two cases of **(a)** a pure charge current and **(c)** a pure spin current. Panel **(b)** schematically shows a spin polarized current, where both a spin and a charge current flow simultaneously. Taken from Ref. [Rub21].

in form of a net spin current density $\mathbf{j}_s$, which is defined as [Cze11]

$$\mathbf{j}_s = -\frac{\hbar}{2e} \left(\mathbf{j}_\uparrow - \mathbf{j}_\downarrow\right). \tag{2.2}$$

Here, $\hbar$ is the reduced Planck constant and $e > 0$ is the elementary charge. The prefactor $-\hbar/(2e)$ stems from the fact that a single electron carries an angular momentum of $(\hbar/2)$ and a charge of $-e$ in the charge current picture. The relations above hold, if spin-flip scattering in the transport medium can be neglected. Note, that the pure spin current is a tensor quantity because it not only consists of the charge current direction, but also the orientation of the spins [Alt18]. In the simplified model of Eq. (2.1) we assume a fixed orientation of the spin polarization and only take the vector direction of the spin current flow into account, simplifying the considerations.

With these equations in mind, we now look at the three cases shown in Fig. 2.1, where a pure charge current (spin up and spin down electrons move in the same direction) is depicted in Fig. 2.1(a) and a pure spin current (spin up and spin down electrons move in opposite directions) is shown in Fig. 2.1(c). The third case describes a spin polarized current, where the current densities of the two spin species are not equal as depicted in Fig. 2.1(b).

In this thesis we make use of the fact that pure spin currents can flow in electric conductors, but also in magnetically ordered insulators via elementary excitations of the magnetic lattice, the so called magnons, instead of relying on charge transport [Alt18].

2.1.2 (Inverse) Spin Hall Effect

In our experiments we generate a spin current from a pure charge current via a process called the spin Hall effect (SHE), which describes the process of spatially separating the two spin species perpendicular to the charge current direction and spin polarization in a heavy metal with large spin-orbit interaction. This effect was first introduced by Dyakonov and Perell [DP71] and later theoretically described and simplified by Hirsch [Hir99]. First experimental confirmations were achieved a few years later [Kat+04; Wun+05], which has sparked large research interest in this area in recent years [Sin+15]. The SHE is visualized in Fig. 2.2(a), where a charge current with the density $\mathbf{j_c}$ with a particular spin polarization along $\mathbf{s}$ creates a spin current with density $\mathbf{j_s}$. The resulting spin current density $\mathbf{j_s^{SHE}}$ generated from an applied charge current density $\mathbf{j_c}$ is given by [Alt18]

$$\mathbf{j_s^{SHE}} = \alpha_{SH} \left(\frac{\hbar}{2e} \right) \mathbf{j_c} \times \mathbf{s}. \tag{2.3}$$

Here, α_{SH} is the spin Hall angle, a material dependent parameter describing the efficiency of the spin to charge current conversion and $\mathbf{s}$ denotes the spin orientation.

The opposite effect is the inverse spin Hall effect (ISHE) depicted in Fig. 2.2(b), where a pure spin current with spin current density $\mathbf{j_s}$, again with spin polarization along $\mathbf{s}$, flowing through a normal metal with finite spin orbit coupling leads to a deflection of the two spin species in opposite directions, thereby creating a pure charge current density $\mathbf{j_c^{ISHE}}$ [Alt18]

$$\mathbf{j_c^{ISHE}} = \alpha_{SH} \left(\frac{-2e}{\hbar} \right) \mathbf{j_s} \times \mathbf{s}. \tag{2.4}$$

Note, that due to Onsager's law of reciprocity, the efficiency of converting spin currents back into charge currents via the ISHE is the same as for the SHE and is given by the spin Hall angle α_{SH}.

The heavy metal used in the samples of this thesis is Platinum (Pt). It has been chosen, because its spin Hall angle is quite large $\alpha_{SH} \simeq 0.1$ [Mor+11] leading to the generation of a larger spin current density from the same charge current density according to Eq. (2.3). Also, it is an established material platform for all-electrical magnon transport experiments at WMI [Wim+19a; Güc+21; Rub21].

2.1.3 Interfacial Spin Currents

By applying a charge current to a normal metal (NM) strip patterned on top of a ferromagnetic insulator (FMI), a spin current is created in the NM via the SHE, which can cross the NM/FMI-interface, giving rise to a spin accumulation beneath this injector strip. The charge current also leads to Joule-heating of the conductor, which in turn excites magnons in the FMI. A more detailed analysis of these processes can be found in [Wim21]. The injected spin current then diffuses through the system
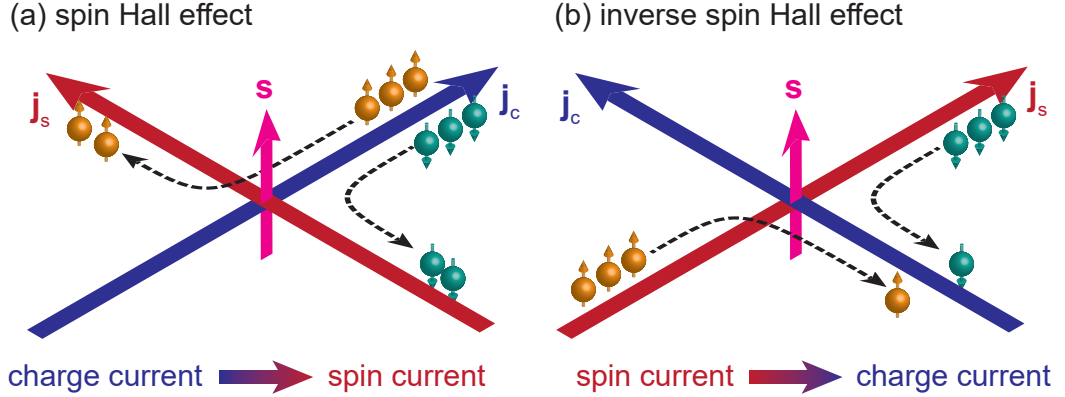
(a) spin Hall effect

(b) inverse spin Hall effect

charge current ➡ spin current

spin current ➡ charge current

Figure 2.2: Schematic sketch of **(a)** the spin Hall effect, where a pure charge current with density $\mathbf{j}_c$ is transformed into a pure spin current with spin current density $\mathbf{j}_s$ and **(b)** the inverse spin Hall effect, where a pure spin current with the density $\mathbf{j}_s$ is transformed into a pure charge current with density $\mathbf{j}_c$. Taken from Ref. [Rub21].

until they reach another NM-strip, the detector strip, where they pass the FMI/NM-interface as a spin current which is transformed back into a charge current via the ISHE in the NM. In this chapter we take a closer look at how the spin current crosses the interfaces out of the injector and back into the detector.

We define the spin current density $\mathbf{j}_{s,\text{int}}$ across the interface using the geometry depicted in Fig. 2.3 as

$$
\begin{aligned}
\mathbf{j}_{s,\text{int}} = &\frac{1}{4\pi}\left(\tilde{g}_i^{\uparrow\downarrow} + \tilde{g}_r^{\uparrow\downarrow}\mathbf{m}\times\right)\left(\mu_s^0\mathbf{s}\times\mathbf{m} - \hbar\dot{\mathbf{m}}\right), \\
&+ \left[g\left(\mu_m + \mu_s^0\mathbf{s}\cdot\mathbf{m}\right) + S\left(T_m - T_e\right)\right]\mathbf{m}
\end{aligned}
\tag{2.5}
$$

closely following the approaches of Refs. [BT15; Wim21; Rub21]. Here, $\mathbf{m}$ is the magnetization, $\tilde{g}_r^{\uparrow\downarrow}$ and $\tilde{g}_i^{\uparrow\downarrow}$ are the effective real and imaginary spin mixing conductances, $\mu_s^0\mathbf{s}$ is the spin accumulation at the interface, with μ_s^0 the spin chemical potential at the interface and $\mathbf{s}$ the unit vector of spin. Furthermore, T_m and T_e are the temperatures of the magnons and the electrons respectively, while S is the spin Seebeck coefficient. Moreover, g is the spin conductance and μ_m denotes the magnon chemical potential. One important thing to note is, that the vector $\mathbf{j}_{s,\text{int}}$ points along the spin polarization direction and hence not along the spin current direction, which is always oriented perpendicular to the interface.

The first line in Eq. (2.5) is the mathematical description of the spin-flip scattering at the interface, which is maximal, when $\mathbf{m} \perp \mathbf{s}$. This situation is depicted in panel (a) of Fig. 2.3. The electrons that comprise the spin current elastically scatter at the interface "producing" an excess angular momentum $\hbar$ in the system due to angular momentum conservation. This excess angular momentum can only be compensated for by the FMI. Thus the two torques $\tau_r = \tilde{g}_r^{\uparrow\downarrow}\mathbf{m}\times(\mathbf{m}\times\mathbf{s})$ and $\tau_i = \tilde{g}_i^{\uparrow\downarrow}(\mathbf{m}\times\mathbf{s})$ are
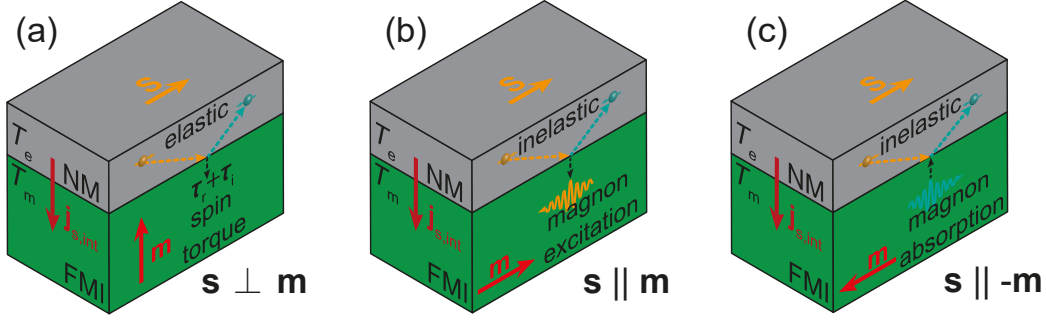
Figure 2.3: Spin-flip scattering processes of the electrons in a NM electrode on top of a FMI. In the case of **(a) s ⊥ m**, the spins scatter elastically off the interface, exerting a torque on the FMI. In the case of (anti)parallel alignment of **s** and **m (b)**, **(c)** the electrons scatter inelastically. In the parallel (antiparallel) case, magnons are excited in (absorbed from) the FMI. Independent of the geometry, thermal magnon excitation is possible in all three cases. Adapted from Ref. [Rub21].

acting on the magnetization of the FMI. Here τ_r has the symmetry of a damping-like torque [Slo89; Ber96] due to the dephasing of the of the electron spins that occurs when they are scattered, whereas τ_i has the symmetry of a field like torque, which emerges because of the incomplete dephasing of spins after scattering at the interface. The terms proportional to $\dot{\mathbf{m}}$ are responsible for the spin pumping effect due to a dynamically precessing magnetization, which is discussed in more detail in Sec. 2.2.5.

The first term in the second line of Eq. (2.5) scales with the spin conductance g and is used to account for inelastic spin-flip scattering events at the interface as depicted in Fig. 2.5(b) and (c). Moreover, g scales $\propto (T/T_C)^{3/2}$ [Cor+16], where T_C is the Curie temperature. This effect is maximal, when **s** ∥ **m** and shows a cosine dependence on the direction of the applied external magnetic field.

The second term in the second line of Eq. (2.5) scales with the spin Seebeck coefficient S (for finite Temperatures) and describes a transport effect across the interface. It is driven by different temperatures in the magnonic (T_m) and electronic (T_e) systems and is called the spin Seebeck effect (SSE) [Xia+10; Uch+10]. Such a temperature difference is created by the Joule-heating of the injector strip, when driving a charge current through it. The spin polarization of the so created spin current points antiparallel to **m** (for positive **s**) and does not depend on the angle of the applied magnetic field.

At low temperatures, both g and S become vanishingly small, while $\tilde{g}_r^{\uparrow\downarrow}$ and $\tilde{g}_i^{\uparrow\downarrow}$ remain finite [BT15]. For that reason, we expect the magnon transport signal to vanish at very low temperatures [Alt18], because it depends on the second line of Eq. (2.5) (cf. Sec. 2.1.4).
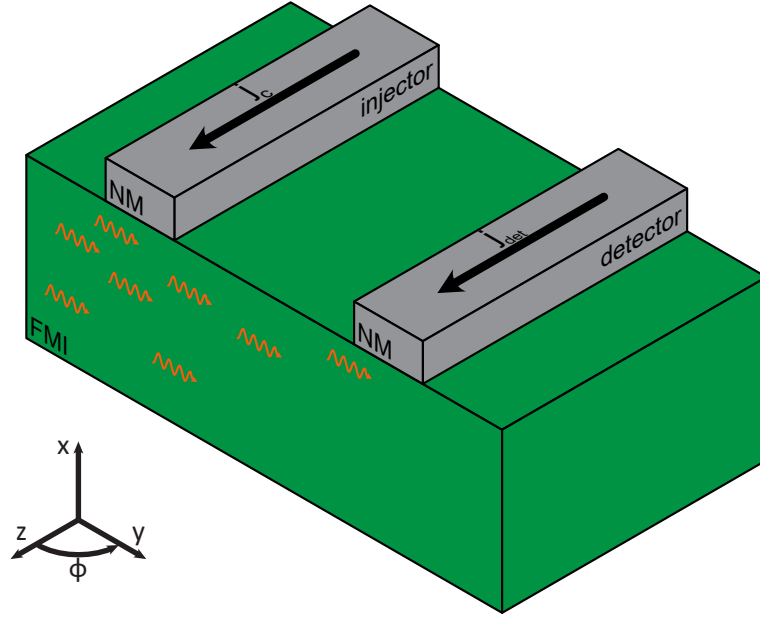
Figure 2.4: Schematic depiction of the two strip structure used in magnon transport experiments. On top of the FMI two NM-strips act as injector and detector of the magnon spin transport. The orange arrows indicate the magnetic excitations, which carry the spin information.

2.1.4 Spin Hall Effect and Joule-Heating Induced Magnon Transport

This section deals with the transport of magnons in a FMI. The most basic device for such magnon transport experiments consists of two NM-strips patterned on top of a FMI as shown in Fig. 2.4. In this regard, it is apparent, that the interfacial spin currents discussed in Sec. 2.1.3 play an important role here as well. Also shown in that figure is the coordinate system with the definition of the in-plane rotation angle ϕ, that will be used throughout this thesis. This angle represents the orientation of the external magnetic field with respect to the sample. In the following discussion, we assume that the external magnetic field is large enough, such that we can assume, that the magnetization in the FMI and the external magnetic field are always oriented parallel to each other. The first theoretic proposal of these magnon transport effects was introduced by Zhang and Zhang [ZZ12a; ZZ12b], which was later confirmed experimentally by Cornelissen et al. [Cor+15] and Goennenwein et al. [Goe+15].

We deal with the case of nonzero temperatures here, where the electronic spin current can couple to thermal fluctuations in the magnetic lattice of the FMI, the so-called magnons. Magnons are quasiparticles, that are used to describe excitations of the magnetic lattice in FMIs. A more detailed discussion of magnons will be given in Sec. 2.2.3, where their dispersion relation is calculated. In the following, we will

closely follow the approach of Ref. [Wim21], where a more detailed analysis can also be found.

The magnons are injected into the FMI at the injector NM-strip, because the electronic spin current described by Eq. (2.5) couples to the thermal magnon gas, which is always present in the FMI at finite temperatures. This coupling occurs only for the case of longitudinal magnons, where $\mathbf{m} \parallel \mathbf{s}$. We now define the interfacial magnon flux $j_{\mathrm{m,int}} = \mathbf{j}_{\mathrm{s,int}}^{\mathrm{z}} \cdot (-\mathbf{m})$, which for finite temperatures is given by [BT15]

$$j_{\mathrm{m,int}} = -g \left(\mu_{\mathrm{m}} + \mu_{\mathrm{s}}^0 \mathbf{s} \cdot \mathbf{m} \right) - S \left(T_{\mathrm{m}} - T_{\mathrm{e}} \right). \tag{2.6}$$

The two terms in this equation are the same as the two terms in the second line of Eq. (2.5) already discussed in Sec. 2.1.3 describing the SHE induced magnon injection and the thermally (Joule-heating) induced magnon injection, respectively.

We now focus on the setup depicted in Fig. 2.4, where one NM-strip acts as an injector, injecting magnons across the NM/FMI-interface via the SHE and thermal excitation, while the other strip acts as a detector of the magnons via the ISHE. By locally injecting magnons, a non-equilibrium magnon accumulation is created (orange arrows in Fig. 2.4), which leads to a diffusive transport of magnons in the FMI towards areas with lower magnon densities. This transport is theoretically described by Boltzmann transport theory, a discussion of which can be found in Ref. [Wim21]. These considerations for injection, transport and detection allow us to describe the the expected signature for the angle-dependent spin detection signal (proportional to the voltage drop V_{det} across the detector NM-strip) in all-electrical magnon transport experiments.

The first term in Eq. (2.6), proportional to g, describes the magnon injection via a spin current introduced by the SHE from a charge current with density $\mathbf{j}_{\mathrm{c}}$. This effect is largest when $\mathbf{s} \parallel \mathbf{m}$. As the detection utilizes the exact inverse process (also depending on the angle of the external field), the net angle dependence of the SHE induced magnon transport voltage is given by

$$V_{\mathrm{det}}^{\mathrm{SHE}} \propto \cos^2(\phi), \tag{2.7}$$

which is 180°-symmetric.

The second possible magnon injection process present in these devices occurs from the resistive Joule-heating due to the charge current flowing through the NM-strip, which in turn locally heats the FMI beneath the NM-strip. This induces a temperature difference between the magnon temperature T_{m} and the electron temperature T_{e}, which is accounted for by the term proportional to the spin Seebeck coefficient S in Eq. (2.6). From Eq. (2.6) it is apparent, that this contribution does not depend on the direction of the spin polarization $\mathbf{s}$ in the injector. Therefore, the Joule-heating induced magnon transport voltage only gains an angular dependence from the detection process via the ISHE

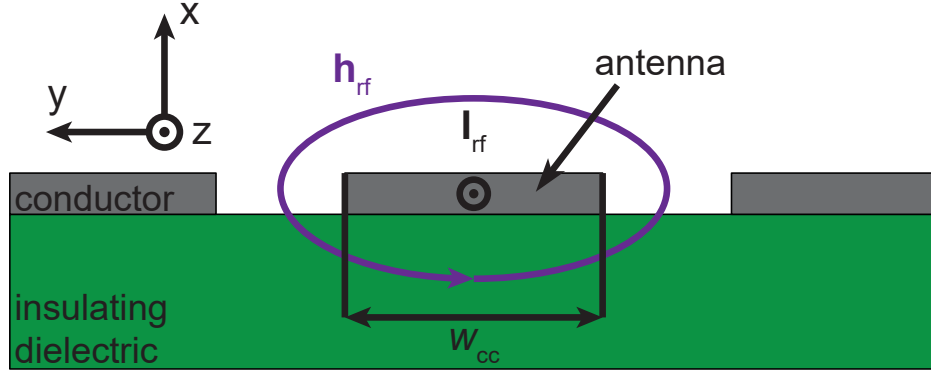$$V_{\mathrm{det}}^{\mathrm{therm}} \propto \cos(\phi) \tag{2.8}$$

Figure 2.5: Schematic depiction of the microwave magnetic field $\mathbf{h}_{\mathrm{rf}}$ around a center conductor of a coplanar waveguide carrying a microwave charge current $\mathbf{I}_{\mathrm{rf}}$. Adapted from Ref. [Rub21].

and is thereby 360°-symmetric.

Consequently, in our experiments we measure a superposition of these voltages (and higher order effects) and need to distinguish between them. For that purpose, we use a lock-in detection method which is explained in more detail in Sec. 3.2.2.

2.2 Magnetization Dynamics and AC Modulation

2.2.1 Karlqvist Equations

The devices used in this thesis rely on an on-chip microwave antenna for creating a microwave magnetic field, with the goal of modulating the magnon transport between injector and detector strip. In order to understand the microwave creation process, we here discuss a simple picture used to calculate the dynamic magnetic driving field $\mathbf{h}_{\mathrm{rf}}$ generated by an oscillatory charge current $\mathbf{I}_{\mathrm{rf}}$ running through a thin metallic antenna structure, the so called Karlqvist equations [Kar54]

$$
\begin{aligned}
h_{\mathrm{rf,oop}}(x,y) &= \frac{h_0}{2\pi} \ln\left(\frac{(y + w_{\mathrm{cc}}/2)^2 + x^2}{(y - w_{\mathrm{cc}}/2)^2 + x^2} \right), \\
h_{\mathrm{rf,ip}}(x,y) &= \frac{h_0}{\pi} \left[\arctan\left(\frac{y + w_{\mathrm{cc}}/2}{x} \right) - \arctan\left(\frac{y - w_{\mathrm{cc}}/2}{x} \right) \right],
\end{aligned}
\tag{2.9}
$$

where w_{cc} is the width of the center conductor of the coplanar waveguide (CPW), and x (y) are the out-of-plane (in-plane) distance from the center of the antenna structure. The dimensions and coordinate system are shown in Fig. 2.5, together with the shape of the microwave magnetic field $\mathbf{h}_{\mathrm{rf}}$. The magnetic field h_0 in the center of the current carrying conductor is calculated from the microwave power P_{rf}

and the input impedance Z_0 of the CPW via

$$h_0 = \frac{I_{\mathrm{rf}}}{2w_{\mathrm{cc}}} = \frac{1}{2w_{\mathrm{cc}}}\sqrt{\frac{P_{\mathrm{rf}}}{Z_0}}. \tag{2.10}$$

2.2.2 Magnetization Dynamics and Ferromagnetic Resonance

We start off our considerations of the magnetization dynamics by introducing the macrospin model. In a bulk ferromagnet (FM), neighboring spins orient themselves parallel to each other due to the exchange interaction described by the Heisenberg model [Hei26]. In this picture, the total magnetization $\mathbf{M}$ of the FM is defined as the sum over all magnetic moments $\boldsymbol{\mu}_{\mathrm{j}}$ in the volume V [Wim21]

$$\mathbf{M} = \frac{1}{V}\sum_{\boldsymbol{\mu}_{\mathrm{j}} \in V} \boldsymbol{\mu}_{\mathrm{j}}. \tag{2.11}$$

For the following discussion, we define the unit vector of magnetization $\mathbf{m} = \mathbf{M}/M_{\mathrm{s}}$ by normalizing the total magnetization to the saturation magnetization M_{s}, which is the magnetization in the case of parallel alignment of all magnetic moments.

The magnetization in the steady state aligns parallel to the an effective magnetic field $\mathbf{H}_{\mathrm{eff}}$, which consists of multiple different magnetic field contributions [Wim21]

$$\mathbf{H}_{\mathrm{eff}} = \mathbf{H}_{\mathrm{ext}} + \mathbf{H}_{\mathrm{ani}} + \mathbf{H}_{\mathrm{D}} + \mathbf{H}_{\mathrm{ex}}, \tag{2.12}$$

where $\mathbf{H}_{\mathrm{ext}}$ is the external magnetic field, $\mathbf{H}_{\mathrm{ani}}$ the magnetic anisotropy field induced by the magnetic material, $\mathbf{H}_{\mathrm{D}}$ the demagnetization field given by the shape of the sample and $\mathbf{H}_{\mathrm{ex}}$ the exchange field from the Heisenberg model [Hei26].

When the magnetic material is dynamically driven by the microwave magnetic field around an antenna structure, we need to include the microwave magnetic field $\mathbf{h}_{\mathrm{rf}}$ to the effective magnetic field of Eq. (2.12). Conversely, we do not include the exchange field in the following discussion, because $\mathbf{m} \parallel \mathbf{H}_{\mathrm{ex}} \rightarrow \mathbf{m} \times \mathbf{H}_{\mathrm{ex}} = 0$ [GM18] under the assumption of saturated magnetization in the sample and a small precession cone angle. Moreover, we omit the anisotropy contribution $\mathbf{H}_{\mathrm{ani}}$, as its contribution is small for the YIG grown in the (111)-direction on Gadolinium Gallium Garnet ($\mathrm{Gd_3Ga_5O_{12}}$, abbreviated as GGG) substrates used in this thesis [Lee+16]. The resulting effective magnetic field then is

$$\mathbf{H}_{\mathrm{eff}} = \mathbf{H}_{\mathrm{ext}} + \mathbf{H}_{\mathrm{D}} + \mathbf{h}_{\mathrm{rf}}. \tag{2.13}$$

If $\mathbf{m}$ is excited out of equilibrium, a torque $\mathbf{T} = V\mathbf{m} \times \mu_0\mathbf{H}_{\mathrm{eff}}$ starts acting on it [GM18]. We also define the angular momentum $\mathbf{L}$ as
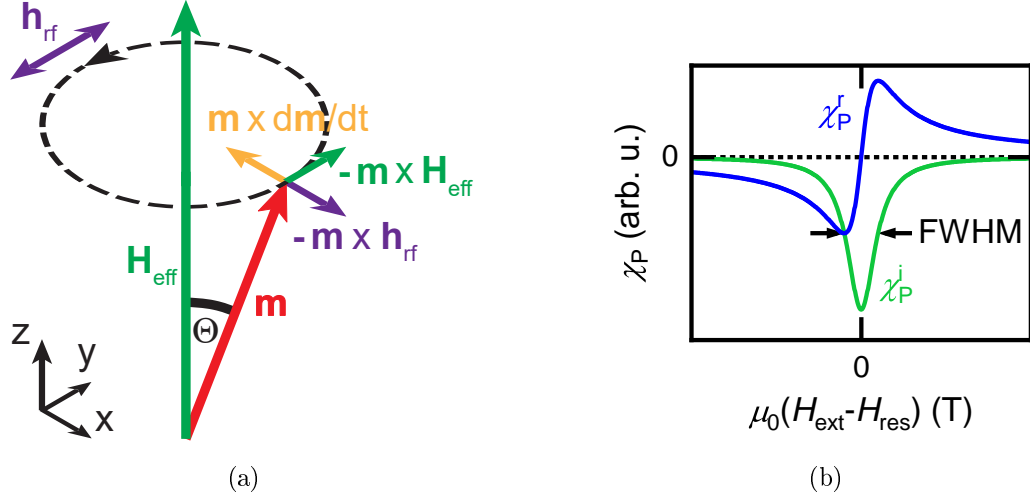
$$\mathbf{L} = -\frac{V}{\gamma}\mathbf{m}, \tag{2.14}$$

Figure 2.6: **(a)** Schematic representation of the ferromagnetic resonance in the macrospin model. The magnetization **m** starts to precess, when a static effective field $\mathbf{H}_{\text{eff}}$ is applied. This precession is damped by the Gilbert damping of the LLG Eq. (2.16) (yellow arrow). In our experiments, we add a dynamic contribution $\mathbf{h}_{\text{rf}}$ to the magnetic field which gives rise to an additional torque $-\mathbf{m} \times \mathbf{h}_{\text{rf}}$, which counteracts the damping contribution. **(b)** Real (blue) and imaginary (green) part of the Polder susceptibility (Eq. (2.21)) plotted as a function of the external field. Taken from Ref. [Rub21].

with $\gamma = g\mu_{\text{B}}/\hbar$ the gyromagnetic ratio, where g is the g-factor and μ_{B} is the Bohr magneton. We now combine the torque and the angular momentum in the relation $\mathbf{T} = \mathrm{d}\mathbf{L}/\mathrm{d}t$, which yields

$$\frac{\mathrm{d}\mathbf{m}}{\mathrm{d}t} = -\gamma\mathbf{m} \times \mu_0\mathbf{H}_{\text{eff}}. \tag{2.15}$$

This is the Landau-Lifshitz equation [LL65], which describes the precession of a magnetic moment in the effective magnetic field defined in Eq. (2.13). Note, that this simplified picture does not account for angular momentum dissipation in the form of damping, which is an integral part of any real system.

This damping of the magnetization precession is phenomenologically described by adding a second term to Eq. (2.15), which is proportional to a damping parameter α, called the Gilbert damping parameter [Gil04]

$$\frac{\mathrm{d}\mathbf{m}}{\mathrm{d}t} = -\gamma\mathbf{m} \times \mu_0\mathbf{H}_{\text{eff}} + \alpha\mathbf{m} \times \frac{\mathrm{d}\mathbf{m}}{\mathrm{d}t}. \tag{2.16}$$

The effect of this is a torque acting on the magnetization directed into the center of the precession cone as shown by the yellow contribution in Fig. 2.6(a).

In resonance, this damping induced relaxation of the magnetic moments towards

the effective magnetic field direction is counterbalanced by the microwave magnetic field $\mathbf{h}_{\text{rf}}$ perpendicular to the external magnetic field, creating a torque $-\mathbf{m} \times \mathbf{h}_{\text{rf}}$ (purple contribution in Fig. 2.6(a)). Another result from these considerations is, that the precession cone angle Θ depicted in Fig. 2.6(a) increases with increasing microwave magnetic field magnitude.

Without loss of generality, we now set the static components of the effective magnetic field (2.13) to point along the z-direction as depicted in Fig. 2.6(a) and the time dependent magnetic field $\mathbf{h}_{\text{rf}}$ in the x-y-plane. We can then also consider the magnetization to only vary in the x-y-plane, while its z-component remains constant, which is valid for small transverse components of $\mathbf{m}$, i.e. small Θ. This can be expressed as

$$\mathbf{H}_{\text{eff}}(t) = \begin{pmatrix} h_{\text{rf,x}}e^{i\omega_{\text{rf}}t} \\ h_{\text{rf,y}}e^{i\omega_{\text{rf}}t} \\ H_{\text{ext}} + H_{\text{D}} \end{pmatrix}, \ \mathbf{m}(t) = \begin{pmatrix} m_{\text{x}}e^{i\omega_{\text{rf}}t} \\ m_{\text{y}}e^{i\omega_{\text{rf}}t} \\ 1 \end{pmatrix}, \ m_{\text{x,y}} \ll 1, \qquad (2.17)$$

where ω_{rf} is the frequency of the microwave magnetic field $\mathbf{h}_{\text{rf}}$ and i is the imaginary unit, whereas m_{x} and m_{y} describe the magnetization precession in the x-y-plane.

In the linear regime, we define the Polder susceptibility matrix $\hat{\chi}_{\text{P}}$ as

$$\begin{pmatrix} h_{\text{rf,x}} \\ h_{\text{rf,y}} \end{pmatrix} = \hat{\chi}_{\text{P}}^{-1} \begin{pmatrix} m_{\text{x}} \\ m_{\text{y}} \end{pmatrix}. \qquad (2.18)$$

We now take Eq. (2.17) in combination with Eq. (2.18) and plug them into the LLG-equation (2.16). This is then solved for the Polder susceptibility matrix, yielding

$$\hat{\chi}_{\text{P}}^{-1} = \begin{pmatrix} A_1 & -\frac{i\omega_{\text{rf}}}{\gamma\mu_0} \\ \frac{i\omega_{\text{rf}}}{\gamma\mu_0} & A_2 \end{pmatrix} \qquad (2.19)$$

with the matrix elements

$$\begin{aligned} A_1 &= H_{\text{ext}} + M_{\text{s}}(N_{\text{y}} - N_{\text{x}}) + \frac{i\omega_{\text{rf}}\alpha}{\gamma\mu_0} \\ A_2 &= H_{\text{ext}} + M_{\text{s}}(N_{\text{z}} - N_{\text{x}}) + \frac{i\omega_{\text{rf}}\alpha}{\gamma\mu_0}. \end{aligned} \qquad (2.20)$$

Here, the generalized demagnetization tensor elements N_{x}, N_{y} and N_{z} are used to describe the demagnetization field as $\mathbf{H}_{\text{D}} = -\hat{N}M_{\text{s}}\mathbf{m}$ [MD66]. The matrix in Eq. (2.19) is then inverted, to obtain the unitless Polder susceptibility $\hat{\chi}_{\text{P}}$, describing the linear response of the magnetization $\mathbf{m}$ to the microwave excitation field $\mathbf{h}_{\text{rf}}$ [Pol49]

$$\hat{\chi}_{\text{P}} = \frac{M_{\text{s}}}{\det(\hat{\chi}_{\text{P}}^{-1})} \begin{pmatrix} A_2 & \frac{i\omega_{\text{rf}}}{\gamma\mu_0} \\ -\frac{i\omega_{\text{rf}}}{\gamma\mu_0} & A_1 \end{pmatrix}, \qquad (2.21)$$

where $\det(...)$ is the determinant of the matrix. The Polder susceptibility $\hat{\chi}_{\text{P}}$ can be

split into its real (dispersive) part χ_P^r and its imaginary (dissipative) part χ_P^i, as shown in Fig. 2.6(b).

In order to obtain the resonance condition $f_{res} = \omega_{res}/(2\pi)$ and the linewidth $\Delta\omega_{rf}$, we solve $\det(\hat{\chi}_P) \overset{!}{=} 0$ either for the external magnetic field H_{ext} or the microwave frequency ω_{rf} [Lie21]. The result of this is the famous Kittel equation [Kit48] for the resonance frequency

$$f_{res} = \frac{\omega_{res}}{2\pi} = \frac{\gamma\mu_0}{2\pi} \sqrt{[H_{ext} + (N_z - N_x)\,M_s]\,[H_{ext} + (N_y - N_x)\,M_s]}. \qquad (2.22)$$

In the case of a thin film (thickness$\ll$lateral dimensions), using $N_z = N_x = 0$, $N_y = 1$ with magnetic field pointing in plane, Eq. (2.22) reduces to [Lie21]

$$f_{res} = \frac{\gamma\mu_0}{2\pi} \sqrt{H_{ext}\,(H_{ext} + M_s)}. \qquad (2.23)$$

Here, we assume that the x-direction is perpendicular to the sample plane and that the external magnetic field is applied in the y-direction of the sample coordinate system (cf. Fig. 2.11 for the geometry).

In our experiments, however, we sweep the external magnetic field, while applying a constant microwave frequency. We are therefore interested in the resonance field H_{res} which we obtain by solving Eq. (2.23) for H_{ext} and multiplying with μ_0

$$\mu_0 H_{res} = -\frac{\mu_0 M_s}{2} + \sqrt{\left(\frac{\mu_0 M_s}{2}\right)^2 + \left(\frac{2\pi}{\gamma}\right)^2 f^2}. \qquad (2.24)$$

To account for additional shape anisotropy contributions of the thin film sample, we define the ellipticity of the precession cone in the Polder susceptibility [Mül+21]:

$$\hat{\chi}_{ip} = \chi_P \begin{pmatrix} i\epsilon & -1 \\ 1 & i/\epsilon \end{pmatrix}, \qquad (2.25)$$

with the ellipticity

$$\epsilon = \sqrt{1 + \frac{\mu_0 M_s}{\mu_0 H_{ext}}}. \qquad (2.26)$$

In Fig. 2.7, the ellipticity given in Eq. (2.26) is plotted as a function of the external magnetic field H_{ext}. From the graph we see, that the ellipticity is near 1 (circular precession) for large magnetic fields and and becomes strongly elliptical when approaching zero field. A finite ellipticity is required for the parallel pumping process, as we will discuss in more detail in Sec. 2.2.4.
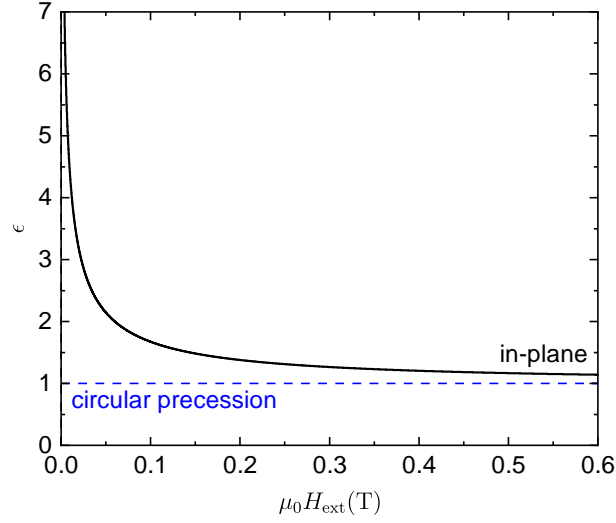
Figure 2.7: Ellipticity ϵ plotted as a function of the external magnetic field $\mu_0 H_{\text{ext}}$ for the magnetic field range measured in the experimental part of this thesis. For the plot we use $\mu_0 M_{\text{s}} = 0.18\,\text{T}$ [Coe10].

2.2.3 Spin Wave Dispersion Relation and Perpendicular Standing Spin Waves

Magnetic excitations travel through magnetic materials in a wave-like manner. Depending on the wavelength λ (and in turn wavevector k) of the spin waves, they are either dominated by the dipolar interaction (long range) or by the exchange interaction (short range) [San+11; Rub21]. In the following, we consider both interactions and their effect on in-plane propagating waves and on perpendicular standing spin waves (PSSWs), forming orthogonal to the film plane.

   The dispersion relation for dipolar-exchange spin waves (in the film plane) is derived from the inverse Polder susceptibility tensor (Eq. (2.19)) by adding the exchange field $H_{\text{ex}} = \tilde{D}k^2$ to its diagonal elements and setting its determinant equal to zero [Wei19]. The resulting so-called Kalinikos-Slavin equation defines the spin-wave dispersion relation for an in-plane magnetized magnetic thin-film [KS86]

$$
\omega_{\text{m}}(k, H_{\text{ext}}) = \mu_0 \gamma \sqrt{\left[H_{\text{ext}} + \tilde{D}k^2 + M_{\text{s}}b_1\right]\left[H_{\text{ext}} + \tilde{D}k^2 + M_{\text{s}}b_2 \sin^2(\beta)\right]},
$$
$$
b_1 = \frac{1 - \exp(-kd)}{kd},
$$
$$
b_2 = 1 - \frac{1 - \exp(-kd)}{kd},
$$

(2.27)

with the spin wave stiffness parameter $\tilde{D} = 2Ag\mu_{\text{B}}/M_{\text{s}}$, the exchange constant A, the length of the wavevector $k = |\mathbf{k}|$, the thickness of the magnetic film d and
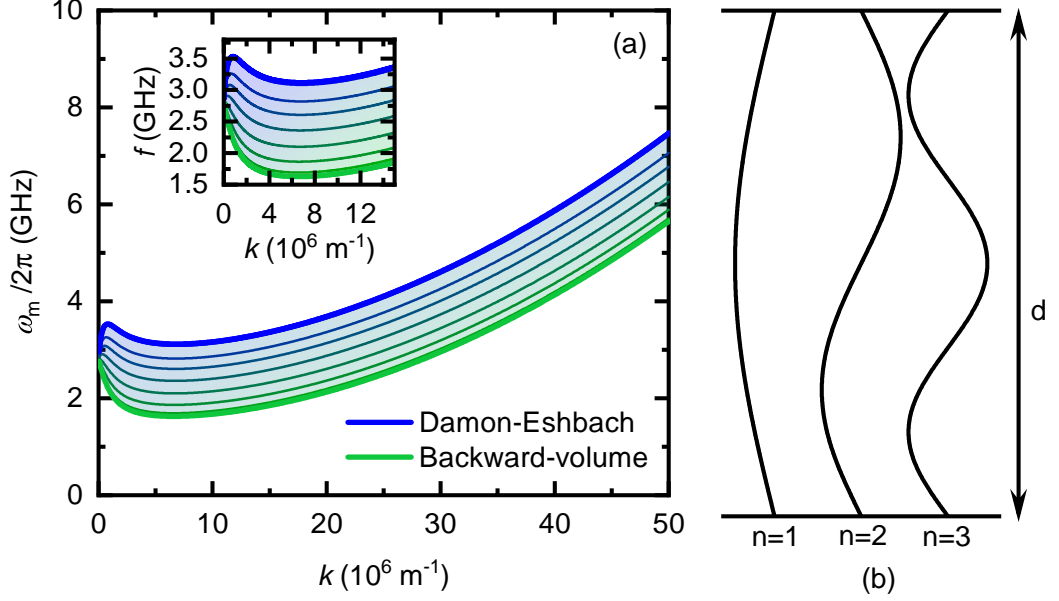
Figure 2.8: **(a)** Spin wave dispersion relation in a YIG thin film with a thickness of $d = 2\,\mu m$ and at an external magnetic field of $\mu_0 H_{ext} = 50\,mT$. The bold lines depict the dispersion in the Damon-Eshbach ($\beta = 90°$) and backward-volume ($\beta = 0°$) geometry. The curves in between are calculated with $\beta = m \cdot 10°$ for m=1,2,...,8. In the inset, a zoom in for small k-vectors is given. Note that some angles are hidden behind the thicker lines of the Damon-Eshbach and the backward-volume geometries. Adapted from Ref. [Rub21] **(b)** Perpendicular standing spin waves in a FMI of thickness d with pinned boundary conditions [Wei19].

the in-plane angle $\beta \triangleleft (\mathbf{k}, \mathbf{m})$ between the spin wave propagation direction and the magnetization direction. In the case of $k \to 0$ (which is true in FMR), the Kalinikos-Slavin equation (2.27) reduces to the Kittel equation (2.22), as $b_1 = 1$ and $b_2 = 0$. For large wavenumbers k, the exchange interaction $\tilde{D}k^2$ dominates, which is the case for the following discussion on PSSWs.

We plot the spin wave dispersion relation (Eq. (2.27)) in Fig. 2.8(a) for various angles of $\beta \triangleleft (\mathbf{k}, \mathbf{m})$ between 0° (backward-volume geometry) and 90° (Damon-Eshbach geometry). The remaining parameters are chosen to represent typical values for our experimental setup ($d = 2\,\mu m$, $\mu_0 H_{ext} = 50\,mT$, $A = 3.7\,pJ\,m^{-1}$ [Kli+15], $\mu_0 M_s = 0.152\,T$). For the backward-volume mode, we observe one clear minimum in the dispersion at finite k, while there are two local minima for the Damon-Eshbach mode, one at $k = 0$ and one at finite k. This two minimum behavior is in contrast with Refs. [Wei19; Rub21], where just one minimum is observed at $k = 0$ for thicknesses of $d = 100\,nm$ and $d = 23.5\,nm$, respectively.

We now focus on the thickness modes of exchange spin waves in magnetic thin

films, the so-called PSSWs. They become relevant due to the long range nature of the exchange interaction at FMI layer thicknesses in the μm regime [Wei19]. Following a similar approach as Ref. [Wei19], we write the dispersion relation of the exchange spin waves as

$$\hbar\omega_0 = \hbar\omega_{\mathrm{FMR}} + \tilde{D}k^2, \tag{2.28}$$

with the ferromagnetic resonance (FMR) frequency ω_{FMR} (cf. Eq. (2.22)). Then we set $\omega_{\mathrm{FMR}} = 0$, yielding the magnetic exchange field

$$\mu_0 H_{\mathrm{ex}} = Dk^2, \tag{2.29}$$

by using $\omega/\gamma = \mu_0 H$ and $\gamma = g\mu_{\mathrm{B}}/\hbar$. Note, that we redefine the spin wave stiffness parameter $D = \tilde{D}/g\mu_{\mathrm{B}} = 2A/M\mathrm{s}$ in Eq. (2.29) in accordance with [Kli+15], removing the $g\mu_{\mathrm{B}}$-factors. In the case of PSSWs, the spin waves are reflected at the top and the bottom surfaces of the FMI. This means, that only certain wavenumbers $k = n\pi/d$ with integer n and film thickness d lead to the creation of PSSWs. The first three PSSWs with pinned boundary conditions and $n = 1, 2, 3$ are shown in Fig. 2.8(b) for reference.

2.2.4 Parametric Pumping: Parallel and Perpendicular Pumping

In this section, we again consider the dynamics of a magnetization $\mathbf{m}$ exposed to an effective magnetic field $\mathbf{H}_{\mathrm{eff}}$. This time however, we differentiate two different geometries between the microwave magnetic field $\mathbf{h}_{\mathrm{rf}}$ and the effective magnetic field $\mathbf{H}_{\mathrm{eff}}$ in the non-linear regime for high powers of the microwave driving field. First, we discuss perpendicular pumping, where $\mathbf{h}_{\mathrm{rf}} \perp \mathbf{H}_{\mathrm{eff}}$, which is the same geometry as in FMR (Sec. 2.2.2). Next, we introduce the case of parallel pumping, where the microwave magnetic field is applied parallel to the static part of the effective magnetic field $\mathbf{h}_{\mathrm{rf}} \parallel \mathbf{H}_{\mathrm{eff}}$.

Both of those cases are shown schematically in Fig. 2.9, where we also display the effect of a finite ellipticity $\epsilon > 1$ on the precession cone. For a perfectly circular precession, the magnetization vector precesses in a circular manner (black dashed line) in the plane perpendicular to $\mathbf{H}_{\mathrm{eff}}$. For a finite ellipticity ϵ however, this precession circle is distorted into an ellipse in the y-z-plane. Due to the fixed magnitude of the vector $\mathbf{m}$, the magnetization vector obtains a finite component $\delta\mathbf{m}_{\parallel}$ (yellow arrow in Fig. 2.9) parallel to the direction of $\mathbf{H}_{\mathrm{eff}}$. For the parallel pumping geometry, we observe in Fig. 2.9 that the microwave magnetic field is able to drive parallel pumping, if its frequency is twice that of the magnetization precession and thus twice the frequency of the microwave field in FMR. In this case, for each complete rotation of the magnetization vector $\mathbf{m}$, the magnetization component $\delta\mathbf{m}_{\parallel}$ reaches its maximum twice. For the perpendicular pumping geometry on the other hand, the frequency of the microwave driving magnetic field is equal to the frequency of the magnetization precession. In the following, a short introduction is given on the basic concepts of
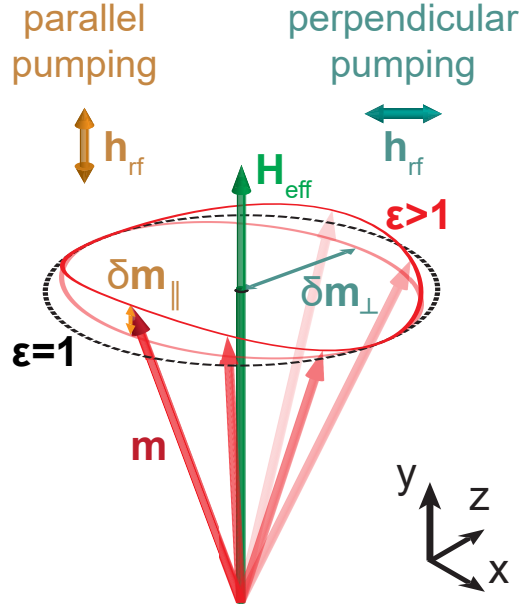
Figure 2.9: Parallel (yellow) and perpendicular (blue) pumping geometries visualized for a unit magnetization **m** precessing around the effective magnetic field **H**$_{\text{eff}}$. Due to a finite ellipticity $\epsilon > 1$, the tip of the magnetization vector is distorted out-of-plane from a perfectly circular precession (black dashed line for $\epsilon = 1$). Adapted from Ref. [Rub21].

parametric pumping in both geometries, while a more detailed theoretical overview of the different parametric pumping processes is available in Ref. [RA90].

Perpendicular Pumping This parametric pumping process occurs in the nonlinear regime of the same geometry as FMR (linear regime), when increasing the power of the driving magnetic field **h**$_{\text{rf}}$ above a certain threshold into the nonlinear regime. First observed experimentally by Damon [Dam53] and Bloembergen and Wang [BW54], the effect was later described theoretically by Suhl [Suh57], who is also the namesake for the two possible perpendicular pumping processes (cf. Fig. 2.10(a) and (b)).

In the perpendicular pumping regime, like in FMR, magnons with $k = 0$ are excited by the photons of the microwave driving field. These magnons then scatter in a three (four) magnon scattering process, which is called the first (second) order Suhl instability, shown schematically in Fig. 2.10(a) and (b). Due to momentum- and energy-conservation, the resulting two magnons possess finite k-vectors with opposite directions.

The first order Suhl instability creates two magnons with half the frequency of the $k = 0$-magnon due to energy conservation [RA90; Rub21]. This means, that the first order Suhl instability only manifests above a certain critical magnetic driving field
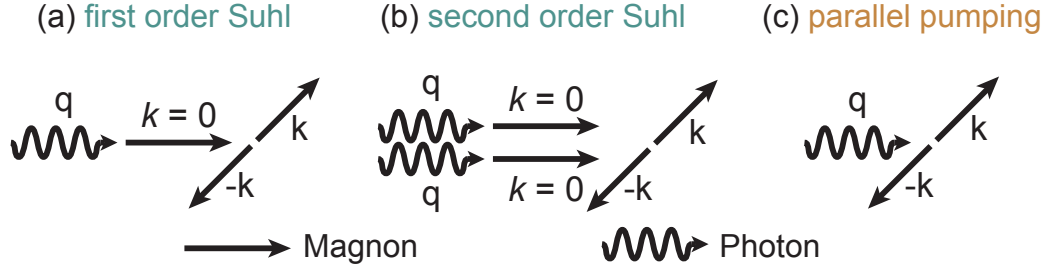
Figure 2.10: Schematic depiction of the parametric pumping processes. Panels **(a)** and **(b)** show the two perpendicular pumping processes, the first and second order Suhl instabilities. There, the microwave photon generated by the microwave driving field first creates one or two magnon(s) of $k = 0$, which then decay into magnons with finite k. The parallel pumping process is depicted in **(c)**, where the photon directly creates two magnons with finite k. Adapted from Ref. [Rub21].

$h_{\mathrm{crit,S1}}$, which is given by [RA90]

$$h_{\mathrm{crit,S1}} = \frac{\omega_{\mathrm{rf}} \Delta H_{\mathrm{k}}}{\gamma M_{\mathrm{s}}}, \tag{2.30}$$

where ω_{rf} is the frequency of the microwave pumping field and ΔH_{k} is the magnon linewidth in units of the applied magnetic field.

The second order Suhl instability describes the generation of two magnons created with the same frequency as the $k = 0$-magnons but finite k in a four-magnon scattering process. Therefore, these two magnons give rise to an additional angular momentum dissipation channel in FMR-experiments, which gives rise to an enhanced FMR-linewidth, when the applied power of the magnetic driving field exceeds a certain critical field, given by [RA90; Rub21]

$$\mu_0 h_{\mathrm{crit,S2}} = \frac{\mu_0 \Delta H_0}{2} \sqrt{\frac{\Delta H_{\mathrm{k}}}{M_{\mathrm{s}}}}. \tag{2.31}$$

Here, ΔH_0 is the magnon linewidth (in units of the magnetic field) of the uniform precession mode, where $k = 0$. In comparison with the value obtained for the first order Suhl instability and parallel pumping, this critical field value is smaller by a factor of 10^{-2} for YIG [RA90].

Parallel Pumping   In contrast with the perpendicular pumping process discussed previously, the parallel pumping process directly creates magnons with finite k, as depicted in Fig. 2.10(c). For this reason, similar to the first order Suhl process, in field-sweep FMR-like experiments, we only expect a parallel pumping signal in a smaller magnetic field range than FMR, for microwave powers above the critical pumping field $h_{\mathrm{crit,pp}}$ for parallel pumping, which has the same value as the critical

pumping field $h_{\text{crit,S1}}$ for the first order Suhl transition [RA90]

$$h_{\text{crit,pp}} = h_{\text{crit,S1}} = \frac{\omega_{\text{rf}} \Delta H_{\text{k}}}{\gamma M_{\text{s}}}. \tag{2.32}$$

For this reason, it is difficult, to differentiate between effects arising from the first order Suhl instability and those arising from parallel pumping. The only difference, that we note is the angle of the propagation direction of the spin waves created by the two processes with respect to the effective magnetic field $\mathbf{H}_{\text{eff}}$. For the first order Suhl, this angle is $\beta = \pi/4$, while it is $\beta = \pi/2$ for parallel pumping, where $\beta \triangleleft (\mathbf{k}, \mathbf{H}_{\text{eff}})$ [RA90]. This propagation direction of the spin waves created by parallel pumping means, that spin waves, which propagate perpendicular to the film plane [Kur+11; Man+15] are also generated, which can lead to the generation of PSSWs [Wie+94] (cf. Sec. 2.2.3). This process is important for the data analysis of the results presented in Sec. 3.4.

Parallel pumping is a well established experimental tool in the field of magnon spintronics, as discussed in the review by Brächer, Pirro and Hillebrands [BPH17]. It enables for example the generation of magnon Bose-Einstein condensates at room-temperature, first realized by Demokritov et al. [Dem+06], due to the high magnon densities, that can be generated by parallel parametric pumping. This has sparked a large research interest, resulting in multiple publications in recent years [Ser+14; Cla+15; Sch+22], where magnon Bose-Einstein condensates have been achieved using parallel parametric pumping.

2.2.5 Spin Pumping

This section is dedicated to an effect called spin pumping, where a precessing magnetization $\mathbf{m}$ near a FMI/NM-interface injects a spin current $\mathbf{j}_s^{\text{pump}}$ into the normal metal directed perpendicular to the NM-plane. Via the ISHE this pure spin current is transformed into a pure charge current, which creates a voltage drop (referred to as the spin pumping voltage V_{SP}) across the length of the NM-strip. Spin pumping was first described theoretically by Tserkovnyak et al. [TBB02a] in 2002. We closely follow the derivation of Ref. [Cze11], in order to introduce a mathematical model for the spin pumping voltage V_{sp} measured in the experiments.

We consider a NM on top of a FMI as depicted in Fig. 2.11. The magnetization in the FMI is excited out of equilibrium by applying a magnetic microwave driving field $\mathbf{h}_{\text{rf}}$. As described in Sec. 2.2.2 this leads to a precessional motion of the magnetization $\mathbf{m}$ around the direction of the effective magnetic field. The precession "pumps" a finite spin current through the FMI/NM-interface orthogonal to the interface plane given by [TBB02b]

$$\mathbf{j}_s^{\text{pump}} = \frac{\hbar}{4\pi} \left[\tilde{g}_{\text{r}}^{\uparrow\downarrow} \left(\mathbf{m} \times \frac{\mathrm{d}\mathbf{m}}{\mathrm{d}t} \right) - \tilde{g}_{\text{i}}^{\uparrow\downarrow} \frac{\mathrm{d}\mathbf{m}}{\mathrm{d}t} \right]. \tag{2.33}$$

Here, $\tilde{g}^{\uparrow\downarrow} = \tilde{g}_{\text{r}}^{\uparrow\downarrow} + i\tilde{g}_{\text{i}}^{\uparrow\downarrow}$ with i the imaginary unit denotes the complex spin mixing con-
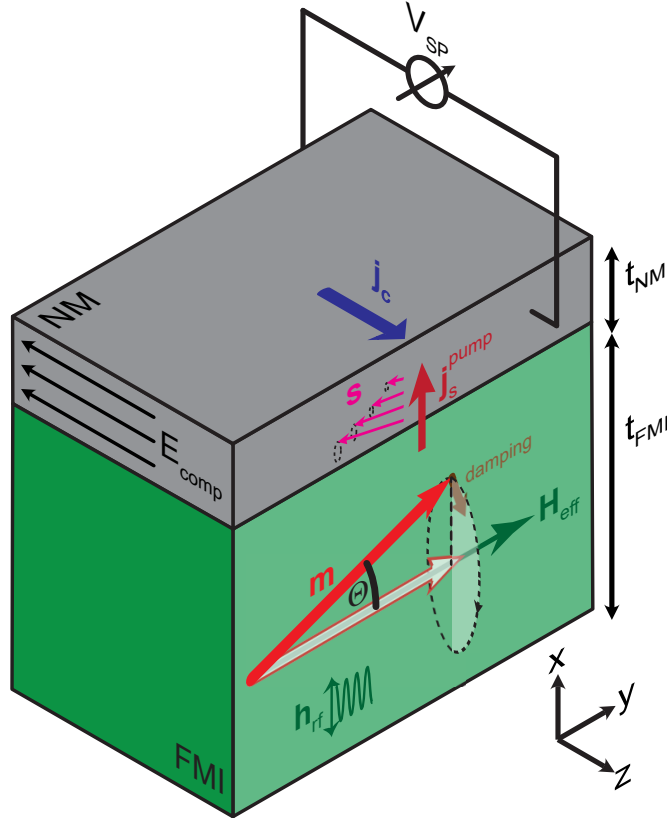
Figure 2.11: Schematic depiction of the effects generating a spin pumping voltage V_{SP} in a FMI/NM bilayer. The magnetization in the FMI is driven out of equilibrium by $\mathbf{h}_{\mathrm{rf}}$ in a precessional motion with cone angle Θ. This gives rise to a spin pumping voltage $\mathbf{j}_{\mathrm{s}}^{\mathrm{pump}}$ into the NM which is transformed into the charge current density $\mathbf{j}_{\mathrm{c}}$ via the ISHE. The charge current creates a charge separation, which in turn leads to the compensating electric field $\mathbf{E}_{\mathrm{comp}}$, which over the length of the NM can be measured as the spin pumping voltage V_{SP}. Adapted from Ref. [Alt18].

ductance, a measure for the spin transport efficiency across the FMI/NM-interface. Note, that the spin current flows from the FMI into the NM here, which is the inverted direction compared to Eq. (2.5), where the spin current flows from the NM into the FMI. When conducting FMR experiments, the first term in Eq. (2.33) acts as an additional damping-like term in the LLG equation (Eq. (2.16)).

The magnitude of the real and imaginary components of $\tilde{g}^{\uparrow\downarrow}$ depend on the material system, that is being studied. In the case of the YIG/Pt-interface in the devices measured in this thesis, the relation $\tilde{g}_r^{\uparrow\downarrow} \gg \tilde{g}_i^{\uparrow\downarrow}$ holds [Alt+13; Che+13]. For this reason, Eq. (2.33) reduces to

$$\mathbf{j}_s^{\text{pump}} = \frac{\hbar}{4\pi} \tilde{g}_r^{\uparrow\downarrow} \left(\mathbf{m} \times \frac{\mathrm{d}\mathbf{m}}{\mathrm{d}t} \right). \tag{2.34}$$

From this equation, it is apparent, that the spin polarization of $\mathbf{j}_s^{\text{pump}}$ is perpendicular to both $\mathbf{m}$ and $\frac{\mathrm{d}\mathbf{m}}{\mathrm{d}t}$. The magnitude of this spin current is proportional to $\tilde{g}_r^{\uparrow\downarrow}$.

By time averaging Eq. (2.34) under the assumption of a simple circular magnetization precession (which is true for large external magnetic fields as can be seen in Fig. 2.7), we obtain a DC spin pumping current [Mos+10]

$$j_s^{\text{pump,DC}} = \frac{\hbar\omega_{\text{rf}}}{4\pi} \tilde{g}_r^{\uparrow\downarrow} \sin^2 \Theta, \tag{2.35}$$

with ω_{rf} the microwave frequency of the driving field and Θ the precession cone angle as shown in Figs. 2.6 and 2.11. Note, that $j_s^{\text{pump,DC}}$ here is a scalar quantity, because the x- and z-component of $\mathbf{j}_s^{\text{pump}}$ vanish when time averaging leaving only the y-component of the polarization.

In the discussion above, we assumed implicitly, that the NM acts as a perfect sink for the spin current. If this is not the case, a nonzero spin current backflow into the FMI is expected due to a spin accumulation in the NM at the interface [TBB02b]. This can however be corrected for by using the effective spin-mixing conductance $\tilde{g}_{\text{eff}}^{\uparrow\downarrow}$ [Rub21], that incorporates this effect, which will be used in the following discussions.

In the following, we derive an explicit expression for the spin pumping voltage V_{SP}. The spin current, that is injected into the NM creates a spin chemical potential bias at the FMI/NM-interface. This potential in turn gives rise to a spin current in the NM, which is transported diffusely according to the one dimensional spin diffusion equation [TBB02b]

$$\frac{\partial \mu_s}{\partial t} = D_{\text{NM}} \frac{\partial^2 \mu_s}{\partial x^2} - \frac{\mu_s}{\tau_{\text{sf}}}. \tag{2.36}$$

Here, μ_s denotes the spin chemical potential, D_{NM} is the spin the diffusion constant in the normal metal and τ_{sf} is the spin-flip scattering time.

For the following calculations, we assume that $\omega_{\text{rf}}\tau_{\text{sf}} \ll 1$, which is called the strong spin-flip scattering limit. In this limit, the left side of Eq. (2.36) vanishes ($\frac{\partial \mu_s}{\partial t} = 0$). We now solve Eq. (2.36) using the following two boundary conditions [TBB02b]: Firstly, we assume, that the spin current is zero at the boundary of the normal metal

and the vacuum

$$j_\text{s}(x = t_\text{NM}) = 0 = \left.\frac{\partial \mu_\text{s}}{\partial x}\right|_{x=t_\text{NM}}, \tag{2.37}$$

where t_NM is the NM thickness in x-direction. Secondly, it is assumed, that the magnitude of the interfacial spin current density is continuous

$$j_\text{s}(x = 0) = j_\text{s}^\text{tot} = -\frac{\hbar \sigma_\text{NM}}{2e^2}\left.\frac{\partial \mu_\text{s}}{\partial x}\right|_{x=0}, \tag{2.38}$$

with σ_NM the normal metal's electrical conductivity. From these boundary conditions it is clear, that the magnitude of the spin chemical potential μ_s decays exponentially across the thickness of the NM. This change in spin chemical potential leads to a spin current along the direction of the spin chemical potential decrease.

Solving the spin diffusion equation (2.36) using the boundary conditions from Eqs. (2.37) and (2.38) we find the following relation for the spin current j_s orthogonal to the interface plane [Cze11]

$$j_\text{s}(x) = j_\text{s}^\text{tot} \frac{\sinh\left(\frac{t_\text{NM}-x}{\lambda_\text{sd}}\right)}{\sinh\left(\frac{t_\text{NM}}{\lambda_\text{sd}}\right)}. \tag{2.39}$$

From this equation, it is apparent, that the spin current depends strongly on the ratio of the NM thickness t_NM and the spin diffusion length λ_sd.

Due to the ISHE, the spin current $j_\text{s}(x)$ is converted into a charge current density $\mathbf{j}_\text{c}^\text{ISHE}$. In order to calculate that charge current density, we insert Eq. (2.39) into Eq. (2.4) and obtain

$$\mathbf{j}_\text{c}^\text{ISHE} = \alpha_\text{SH}\left(\frac{-2e}{\hbar}\right)j_\text{s}(x)\hat{\mathbf{e}}_\text{x} \times \mathbf{s}. \tag{2.40}$$

Here, $\hat{\mathbf{e}}_\text{x}$ is the x-direction unit vector. From this equation, we see, that the charge current will flow in the z-direction, when the spin polarization $\mathbf{s}$ points in the y-direction as illustrated in Fig. 2.11. Another thing to note from Eq. (2.40) is the fact, that the charge current density $\mathbf{j}_\text{c}^\text{ISHE}$ decreases in correspondence to the spin current $j_\text{s}(x)$ across the thickness of the NM.

The charge current density $\mathbf{j}_\text{c}^\text{ISHE}$ gives rise to an imbalance of charges across the z-length of the NM which in turn causes a compensating electrical field

$$\mathbf{E}_\text{comp} = \frac{e\tilde{g}_\text{eff}^{\uparrow\downarrow}\left(\alpha_\text{SH}\lambda_\text{sd}\tanh\frac{t_\text{NM}}{2\lambda_\text{sd}}\right)\hat{\mathbf{e}}_\text{x} \times \mathbf{s}}{\sigma_\text{FMI}t_\text{FMI} + \sigma_\text{NM}t_\text{NM}}\omega_\text{rf}c_\text{corr}\sin^2\Theta, \tag{2.41}$$

pointing in the opposite direction of the charge current flow, with $\sigma_\text{FMI/NM}$ the electrical conductivities of the FMI and the NM. The correction constant c_corr is added to correct for the finite demagnetization fields, which are present in magnetic thin films [Cze11]. A detailed derivation of this relationship can be found in Refs. [Cze11; Mos+10].

Over the entire length L_{NM} of the NM, this in turn gives rise to the spin pumping voltage

$$V_{\mathrm{SP}} = E_{\mathrm{comp}} L_{\mathrm{NM}} = \frac{e \tilde{g}_{\mathrm{eff}}^{\uparrow\downarrow} \left(\alpha_{\mathrm{SH}} \lambda_{\mathrm{sd}} \tanh \frac{t_{\mathrm{NM}}}{2\lambda_{\mathrm{sd}}} \right)}{\sigma_{\mathrm{FMI}} t_{\mathrm{FMI}} + \sigma_{\mathrm{NM}} t_{\mathrm{NM}}} \omega_{\mathrm{rf}} c_{\mathrm{corr}} L_{\mathrm{NM}} \sin^2 \Theta. \qquad (2.42)$$

As we can see here, V_{SP} scales with the sine squared of the precession cone angle Θ, which in turn scales linearly with the microwave magnetic field that excites the system [Cze11]. Using the relation between microwave magnetic field $\mathbf{h}_{\mathrm{rf}}$ and microwave power P_{rf} from the Karlqvist equations (Eq. (2.9)), one expects a linear scaling of Θ with the applied microwave power.

Chapter 3

Experimental Procedures and Results

In this chapter, we present the results obtained from the experiments conducted in this thesis, as well as the experimental procedures used to obtain the results. We begin our discussion by explaining the fabrication of the devices and the challenges encountered therein in the first section. Next, we present the results of our magnon transport experiments in Sec. 3.2. There, we characterize the magnon transport properties of our sample with the well-established angle dependent magnetoresistance (ADMR) measurements, before analyzing field-sweep magnon transport measurements under the influence of an additional microwave magnetic field of varying power levels similar to Ref. [Rub21]. In Sec. 3.3, we investigate the effects induced into the studied system by the spin pumping effect. Furthermore, we aim to separate the effects of transported magnons from the injector Pt-strip from the spin pumping voltage. Then, in Sec. 3.4, the comb-like fine structure, which is observed in all our field-sweep experiments, is analyzed. We use methods similar to Refs. [Wie+94; Kli+15], in order to extract the temperature-dependent spin wave stiffness parameter D from the observed fine structure. Finally, we close the discussion of our experimental results with an analysis of the spin pumping data in a structure with a wider antenna in Sec. 3.5, as a comparison to the earlier spin pumping data, acquired on a device with a narrow antenna. Wide antenna structures are desirable for implementing devices comprising a larger area with a homogeneous in-plane component of the magnetic microwave driving field $h_{\mathrm{rf,ip}}$.

3.1 Device Fabrication and Optimization

In order to discern between parallel and perpendicular pumping contributions, the sample geometry is very important, as it decides the shape of the microwave magnetic field around the antenna and in the FMI. This is apparent from the Karlqvist equations defined in Sec. 2.2.1. From Eq. (2.9) and Fig. 3.19 we deduce, that the width of the antenna should be as large as possible, in order to achieve a predominantly parallel microwave magnetic field distribution in the FMI with a minimal perpendicular contribution beneath the NM-strips. This section first deals with the fabrication of such devices in Sec. 3.1.1, before discussing the challenges that arise, when changing the antenna position from between the strips like in Ref. [Rub21] to a much wider antenna covering both NM-strips in Sec. 3.1.2.

Fabrication Step	Details
resist stack	PMMA 600K (Allresist AR-P 669.04) PMMA 950K (Allresist AR-P 679.02) Electra 92 (Allresist AR-PC 5090.02)
spin coating	1 min, 4000 rpm (same for all resist layers)
bakeout	5 min @ 170°C for PMMA 600K and 950K 2 min @ 90°C for Electra 92
e-beam writing	Base dose: $5.6\,\mathrm{C\,m^{-2}}$ (factors determined by BEAMER software)
development	1. Clean off Electra layer (20 sec in DI-water) 2. Development (2 min in Allresist AR 600-56 developer) 3. Rinse in isopropanol
sputtering	SUPERBOWL sputtering system at WMI
lift-off	Acetone @ 70°C, short ultrasonic pulses at low power

Table 3.1: Detailed parameters for the fabrication steps used to fabricate the samples.

3.1.1 Fabrication Details

The samples used for the experiments shown in the following sections all employ the same general design. In this section, we exemplary show the dimensions of the device discussed in Secs. 3.2, 3.3 and 3.4, while the device measured in Sec. 3.5 employs slightly different dimensions. The basis for our structures comprises a $2\,\mu$m thick YIG-layer with (111)-orientation grown by liquid phase epitaxy (LPE) on top of a $500\,\mu$m thick, (111)-oriented GGG substrate. YIG is a ferrimagnetic material with two different sublattice magnetizations, which is viewed as a ferromagnetic insulator in the scope of this thesis. Before we initiate the device fabrication steps, we first clean off the protective layer and any rough surface dirt by cleaning the sample surface in warm acetone and isopropanol in an ultrasonic bath. After that, a 10 minute Piranha etch (2:1 concentrated sulfuric acid mixed with 30% hydrogen peroxide) in 80°C water bath is performed to remove potential organic contaminants.

On top of the YIG base layer, we then structure two NM-strips (in our case Platinum), similar to the device shown in Fig. 2.4, via electron beam lithography, using a two layer resist stack (PMMA 600K and PMMA 950K), as well as an additional conductive resist (Electra 92). The two layer stack is employed in order to achieve an undercut to facilitate the liftoff process. Details of the type of resists used and their application can be found in Tab. 3.1. Next, proximity effect correction is applied to the strip and antenna layers with the BEAMER and TRACER Software packages [Gmb22], before writing the patterns via electron beam lithography. After development of the resist according to Tab. 3.1, we deposit $t_{\mathrm{Pt}} = 5\,$nm of Platinum (Pt) via magnetron sputtering in the SUPERBOWL Sputtering system at WMI. In a final step, we lift off the remaining resist with the sputtered material on top in warm acetone (cf. Tab. 3.1), leaving only the Pt-strips on the YIG in the desired
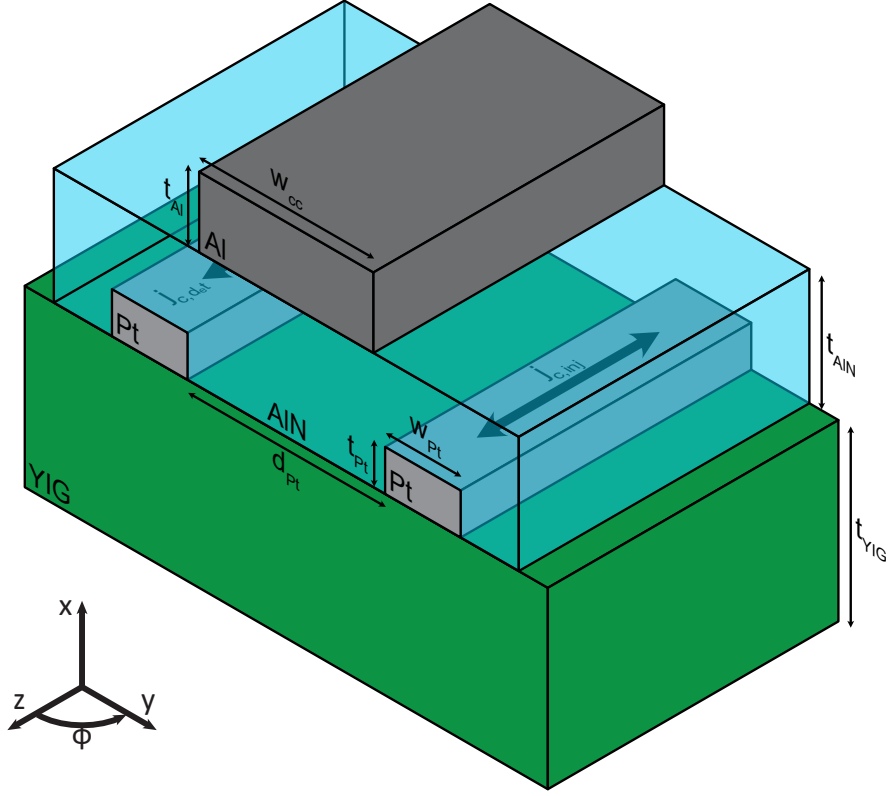
Figure 3.1: Schematic cross section of the two strip structure with a top antenna used for the measurements shown in this thesis. On top of a $t_{\text{YIG}} = 2\,\mu\text{m}$ thick YIG film two Pt-strips with thickness $t_{\text{Pt}} = 5\,\text{nm}$, width $w_{\text{Pt}} = 500\,\text{nm}$ and a spacing of $d_{\text{Pt}} = 1200\,\text{nm}$ are patterned. On top of both strips, there rests an AlN-layer of thickness $t_{\text{AlN}} = 90\,\text{nm}$ for electrical insulation of the strips and the microwave antenna made from Aluminum with a thickness of $t_{\text{Al}} = 50\,\text{nm}$ and a width of $w_{\text{cc}} = 1000\,\text{nm}$.

Device Generation	Insulating Material	Thickness	Sputtering Type
1	AlN	35 nm	reactive
2	SiO$_2$	35 nm	rf
3	AlN	90 nm	reactive
4	AlN	90 nm	reactive

Table 3.2: Overview of the fabrication recipes used for the insulating layers.

pattern. Both Pt-strips have the same dimensions, namely a width of $w_{\mathrm{Pt}} = 500\,\mathrm{nm}$, a thickness of $d_{\mathrm{Pt}} = 5\,\mathrm{nm}$ and a length of $l_{\mathrm{Pt}} = 50\,\mu\mathrm{m}$. This same basic process is employed for all deposition steps of the structure, depositing the different materials as shown in Fig. 3.1.

On top of both Pt-strips, covering the whole length and width of the strips, an insulating layer is deposited by reactive or rf sputtering, using the same resist processing recipe and lift-off procedure as for the Pt-strips. The thickness and materials of this insulating layer have been varied due to problems with the longevity of the samples, which are discussed in more detail in Sec. 3.1.2. Individual parameters for the insulating layers of the specific sample generations are shown in Tab. 3.2.

In the final fabrication step, the Aluminum (Al) antenna is deposited via magnetron sputtering with a thickness of $t_{\mathrm{Al}} = 50\,\mathrm{nm}$ and a width $w_{\mathrm{cc}} = 1000\,\mathrm{nm}$. The length of the antenna is more than double the length of the Pt-strips, meaning we can model the microwave magnetic field as uniform along the length of the Pt-strips. During this same fabrication step, we simultaneously pattern the bondpads for the electric contacts of the structure to the sample holder.

3.1.2 Problems with the First Device Generations

This section deals with the fabrication challenges, that had to be overcome, in order to produce the working samples shown later in this thesis. The first sample generation incorporated the same overall structure as the sample described in Sec. 3.1.1, with the main differences being a thinner insulating layer of thickness $t_{\mathrm{AlN}} = 35\,\mathrm{nm}$ and a wider antenna, which overlaps the Pt-strips. The devices on this sample work, when only the Pt-strips are connected to a sourcemeter, while the antenna is not contacted. They also work when connecting the Pt-strips to nanovoltmeters with high input resistance and connecting the antenna to the vector network analyzer (VNA). However, when we simultaneously connect a current source and the VNA, an electrical discharge burns through the Pt-strips, the insulating layer and the antenna, once the current source is switched on. Observing the broken devices under an optical microscope yields pictures similar to Fig. 3.2, where some of the overlapping area between the antenna and the Pt-strips exhibits a darker shade, hinting towards a physical deformation of the device. This physical deformation is later also confirmed by atomic force microscopy measurements of these areas.

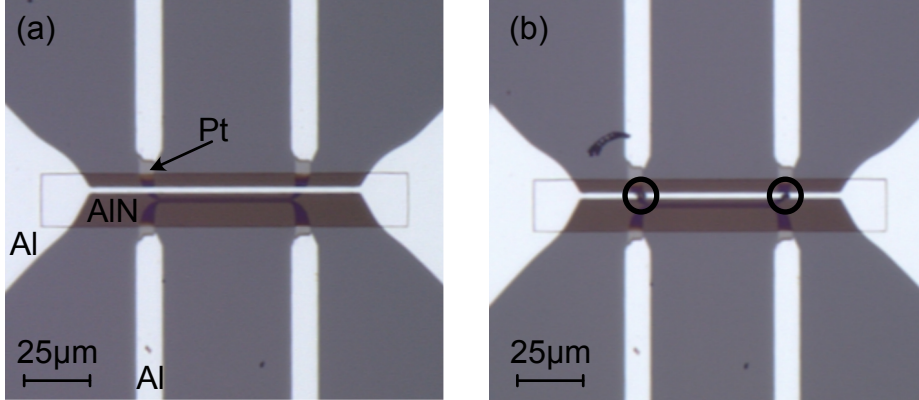Since the simultaneous application of a current at one of the Pt-strips and a mi-

Figure 3.2: Microscope images of a sample with an off-center antenna **(a)** directly after fabrication and **(b)** after the electric contact was lost. In panel (b), the area where the antenna crosses the Pt layer appears darker than before, which we interpret as a destroyed area (marked by black circles).

crowave current through the antenna is essential for reaching the goals of this thesis, several attempts have been made to increase the longevity of the devices. Some of the first measures taken are to change the used equipment, such as the breakout box, microwave cables, sourcemeter and nanovoltmeter, in order to exclude faulty devices as the cause of the problems.

Unfortunately, this did not stop the devices from failing, so in a next step, we have changed the material used for the insulating layer from aluminum nitride (AlN) to silicon dioxide (SiO$_2$), while leaving the rest of the structure unchanged. This is done in order to avoid the possibility of a piezoelectric response of the AlN layer, as sputtered AlN exhibits a rich piezoelectric behavior [Mar+11]. For the devices on this sample we also incorporated a more careful bonding and mounting routine. We for example grounded the contacts on the sample holder while bonding and also shorted the contacts on the sample holder, only removing those shorting bonds shortly before mounting the sample into the cryostat. Furthermore, we tried to set the ground of the microwave to the same potential as the DC current lines using a bias tee element. On top of that, we tried only connecting the signal line of the sample holder CPW to the sample, leaving the ground lines unconnected. All those measures have been taken in order to reduce the likelihood of static electrical discharge leading to a breakdown of the devices, but they had no noticeable effect on the breakdown behavior.

For the next sample we switch the insulating material back to AlN, this time increasing the thickness almost threefold to $t_{AlN} = 90\,\text{nm}$, in order to increase the breakdown voltage between the antenna and the Pt-strips, which are capacitively coupled. We also switch the sample holder to enable us to connect two signal lines to the antenna. However, these changes also did not fix the breakdown behavior.

The final device generation then incorporates the design shown in Fig. 3.1, where we still use the thicker insulating layer, but the antenna does not cover the area of the Pt-strips anymore, in order to avoid the capacitive coupling between antenna and Pt-strips. This layout change has fixed the problem of the devices breaking from an electrical discharge between the antenna and the Pt-strips. Furthermore, it explains, why these described problems were not present in the work by Rubenbauer [Rub21]. There, the microwave antenna is also situated between the Pt-strips, without any overlap with the Pt-strips.

The device used for the experiments shown in Secs. 3.2, 3.3 and 3.4 was fabricated in the fourth generation (cf. Tab. 3.2). In Sec. 3.5 a third generation device is investigated.

3.2 Magnon Transport Experiments

We now turn our focus to magnon transport experiments on the samples fabricated using the recipe given in the previous section. In the beginning, we describe the experimental setup into which the samples are incorporated. We also introduce the lock-in measurement technique, which is the method of choice for the ensuing magnon transport experiments. Next, the transport properties of our sample are tested with the well established ADMR measurements, while applying a microwave magnetic field. Finally, the magnon transport properties of our samples are probed in magnetic field-sweep measurements. The results obtained here are compared to previous work by Liu et al. [Liu+19] and Rubenbauer [Rub21].

3.2.1 Experimental Setup for the Magnon Transport Experiments

In this section, the measurement setup, that is used for the ADMR measurements and the magnon transport field-sweeps is explained. In Fig. 3.3 we see a schematic top view of the device used for the measurements, all electrical connections (which are realized by wirebonding) and the coordinate system together with the definition of the rotation plane for the ADMR measurements.

The two ends of the injector Pt-strip are electrically connected to the output of a Keithley 6221 AC current source, which supplies the oscillating injection charge current of $500\,\mu A$. The two ends of the detector Pt-strip are connected to the two inputs of a Stanford Research Systems SR560 preamplifier. It amplifies the signal for the subsequent detection in a Zurich Instruments MFLI lock-in amplifier. The lock-in also acts as a trigger source for the AC current source, in order to synchronize its demodulator phase with the output current phase of the current source.

The antenna is situated on top of the $90\,nm$ thick AlN insulating layer. It is connected to the first port of the VNA via wirebonds to a CPW printed circuit board (PCB), which in turn is connected to the VNA by a SMA-cable. The signal line and the ground line are shorted on the sample, which means we can measure the S11-Parameter of the VNA.
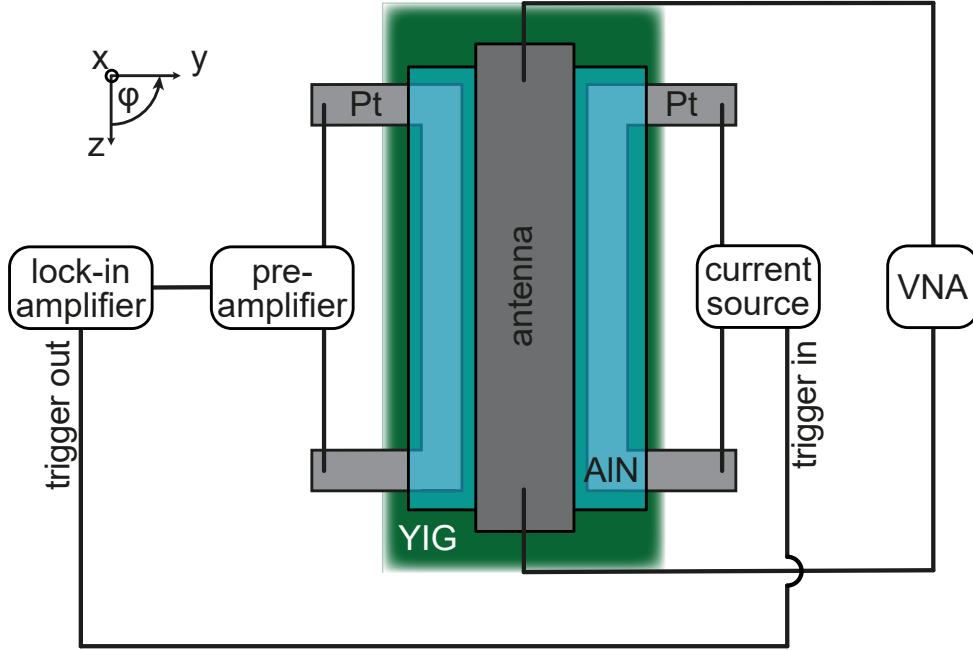
Figure 3.3: Measurement setup for the magnon transport experiments with a top down view of the measured sample geometry. The right Pt-strip is connected to an AC current source injecting a low frequency AC charge current. To the left Pt-strip we connect a preamplifier for amplifying small detection voltages before passing them to the lock-in amplifier, which also acts as a trigger for the charge current source in order to synchronize their clocks. Separated by an AlN insulating layer lies the microwave antenna, which we connect to the VNA, shorting the signal and ground lines on the device.

Having connected the sample in the aforementioned way, we glue it to a sample holder, which in turn can be mounted on a dipstick. This dipstick is then lowered into the variable temperature insert (VTI) of the CHAOS liquid helium cryostat, which allows for the temperature series measurements shown in this thesis. The cryostat also incorporates a three-dimensional superconducting vector magnet, enabling the measurements at arbitrary external magnetic field directions.

3.2.2 Lock-In Measurement Technique

For the detection of the magnon transport signal we apply a slowly varying ($f_{\mathrm{AC}} = 7.121\,\mathrm{Hz}$) AC current to one of the Pt-strips and detect the voltage at the second Pt-strip using a lock-in detection technique. Our description of this measurement technique closely follows Ref. [Wim21]. The AC injector current can be written as $I_{\mathrm{inj}} = I_{\mathrm{inj,0}} \sin(\omega_{\mathrm{AC}} t + \Psi)$ with $\omega_{\mathrm{AC}} = 2\pi f_{\mathrm{AC}}$ and Ψ representing a finite phase shift.

Due to this current modulation, the spin current injected into the FMI and thus the detector current $I_{\text{det}}(t) = I_{\text{det},0} \sin(\omega_{\text{AC}} t + \Psi)$ at the second Pt-strip also varies with the input frequency.

The detector voltage $V_{\text{det}}(t)$ can be written as

$$V_{\text{det}}(t) = R_1 I_{\text{inj}}(t) + R_2 I_{\text{inj}}^2(t) + \mathcal{O}(I_{\text{inj}}^3(t)), \tag{3.1}$$

where R_1 and R_2 are coefficients characterizing the magnon transport from injector to detector. The detector voltage is measured with a lock-in amplifier (after passing through a preamplifier), giving access to the n-th harmonic of the signal, with n an integer number. For each harmonic we measure two quadrature channels X and Y, which corresponds to a multiplication of the detected voltage with two reference signals $\sin(\omega_{\text{AC}} t)$ and $\cos(\omega_{\text{AC}} t)$, respectively. In a second step we integrate the signal over a timeperiod T by low pass filtering

$$V_{\text{X}}^{n\omega} = \frac{\sqrt{2}}{T} \int_t^{t+T} \sin(n\omega_{\text{AC}} t') V_{\text{det}}(t') \mathrm{d}t', \tag{3.2}$$

$$V_{\text{Y}}^{n\omega} = \frac{\sqrt{2}}{T} \int_t^{t+T} \cos(n\omega_{\text{AC}} t') V_{\text{det}}(t') \mathrm{d}t'. \tag{3.3}$$

By plugging Eq. (3.1) into Eqs. (3.2) and (3.3), we obtain the following relations for the first two harmonic voltages:

$$\begin{aligned}
V_{\text{X}}^{1\omega} &= \frac{1}{\sqrt{2}} I_{\text{inj},0} R_1 \cos(\Psi), \qquad V_{\text{Y}}^{1\omega} = \frac{1}{\sqrt{2}} I_{\text{inj},0} R_1 \sin(\Psi), \\
V_{\text{X}}^{2\omega} &= \frac{1}{2\sqrt{2}} I_{\text{inj},0}^2 R_2 \sin(2\Psi), \qquad V_{\text{Y}}^{2\omega} = -\frac{1}{2\sqrt{2}} I_{\text{inj},0}^2 R_2 \cos(2\Psi).
\end{aligned} \tag{3.4}$$

In the experiments conducted in this thesis, we observe a finite phase shift Ψ. This manifests due to the fact, that the detector signal $V_{\text{det}}(t)$ is distributed between the X and Y channels of the lock-in amplifier. However, to be able to analyze the full signal in just one of the channels, we apply a rotation matrix to the signal to account for the phase shift and rotate the signal into just one channel X', Y' for each harmonic

$$\begin{pmatrix} V_{\text{X}'}^{n\omega} \\ V_{\text{Y}'}^{n\omega} \end{pmatrix} = \begin{pmatrix} \cos(n\Psi) & -\sin(n\Psi) \\ \sin(n\Psi) & \cos(n\Psi) \end{pmatrix} \begin{pmatrix} V_{\text{X}}^{n\omega} \\ V_{\text{Y}}^{n\omega} \end{pmatrix}. \tag{3.5}$$

The phase shift Ψ for our experiments is determined iteratively by applying the rotation matrix in Eq. (3.5) with different angles and minimizing the signal in $V_{\text{Y}'}^{1\omega}$ and $V_{\text{X}'}^{2\omega}$. Specifically, for the data shown in the following sections, we employ this method to analyze the ADMR data and then apply the same phase shift for the field-sweep measurements.

3.2.3 Angle-Dependent Magnetoresistance Measurements

This section describes the well-established ADMR measurements (cf. Sec. 2.1.4), used for characterizing the all-electrical magnon transport properties of magnetically ordered materials [Wim+19b; Wim+19a; Güc+20; Güc+21]. Different publications also study the temperature dependence of ADMR measurements in the range below room temperature [Goe+15] and recently also towards temperatures as high as 600 K [Sch+21]. For the measurements discussed in this section, we vary the temperature between 5 K and 280 K in order to extract temperature dependent magnon transport properties. Compared to the sample layouts used in the aforementioned literature, we have added a microwave antenna as shown in Fig. 3.1. By applying a microwave current at varying power levels to the antenna, we study the effect of a microwave magnetic field on the magnon transport properties of YIG. In particular, for the experiments discussed in this section, we apply a continuous wave microwave current with a frequency of 14 GHz at two different power levels of +1 dBm and +15 dBm. If not otherwise stated, all experiments are conducted using a microwave frequency of $f = 14$ GHz.

In our experiments, the first harmonic voltage $V_{\text{det}}^{1\omega}$, measured via lock-in detection technique, corresponds to the SHE induced magnon transport voltage $V_{\text{det}}^{\text{SHE}}$, while the second harmonic voltage $V_{\text{det}}^{2\omega}$ corresponds to the Joule-heating induced magnon transport voltage $V_{\text{det}}^{\text{therm}}$. As detailed in Sec. 2.1.4, we expect a $\sin^2$-behavior for $V_{\text{det}}^{\text{SHE}}$

$$V_{\text{det}}^{1\omega} = V_{\text{det}}^{\text{SHE}} \propto \sin^2(\phi), \tag{3.6}$$

while we expect a sin-behavior for $V_{\text{det}}^{\text{therm}}$

$$V_{\text{det}}^{2\omega} = V_{\text{det}}^{\text{therm}} \propto \sin(\phi), \tag{3.7}$$

when the external magnetic field (and therefore the magnetization of the YIG) is rotated in the plane of the thin film. We define the angle $\phi = 0°$, when the external magnetic field $\mathbf{H}_{\text{ext}}$ points along z-direction and $\phi = 90°$ when $\mathbf{H}_{\text{ext}} \parallel \hat{\mathbf{e}}_{\text{y}}$ as shown in Fig. 3.3.

In Fig. 3.4, the SHE and Joule-heating induced magnon transport voltages $V_{\text{det}}^{\text{SHE}}$ and $V_{\text{det}}^{\text{therm}}$ are plotted as a function of the angle ϕ. We show the data for 5 K and 220 K in panels (a),(b) and (c),(d) respectively. For the ADMR data presented in panels (a) and (c) of Fig. 3.4, we clearly observe a deviation from the expected pure $\sin^2$-dependence in the first harmonic signal. The second lobe for $\phi = 270°$ of the data is higher (lower) than the first one at $\phi = 90°$ for $T = 220$ K ($T = 5$ K). This asymmetry between left and right lobe exhibits a sign change at around 70 K, which is discussed in more detail later on. To account for this asymmetric behavior, we adopt the fit-function that we use for describing the data, adding a sin-contribution, yielding

$$V_{\text{det}}^{\text{SHE}} = y_0 + a_1^{\text{SHE}} \sin^2(\phi_1 + \phi) + a_2^{\text{SHE}} \sin(\phi_2 + \phi), \tag{3.8}$$

where y_0 is a finite voltage offset and ϕ_1, ϕ_2 are finite phase shifts. This expression is
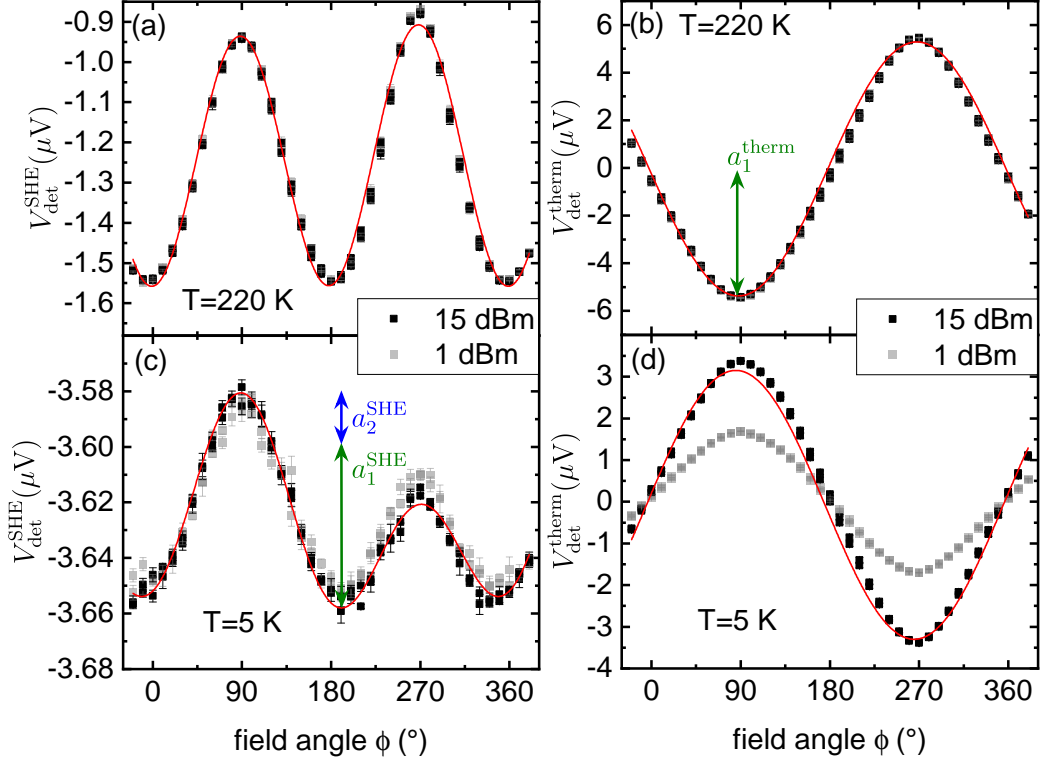
Figure 3.4: Angle dependent magnetoresistance (ADMR) measurements conducted for the applied microwave powers of $+1\,\mathrm{dBm}$ (gray data points) and $+15\,\mathrm{dBm}$ (black data points). For the data shown here, the angle of the external magnetic field is swept up and down from -20° to 380° in 10° steps at a constant magnetic field magnitude of $\mu_0 H_{\mathrm{ext}} = 50\,\mathrm{mT}$. Panels **(a)** and **(c)** show the SHE induced transport voltage $V_{\mathrm{det}}^{\mathrm{SHE}}$ measured at the temperatures $220\,\mathrm{K}$ and $5\,\mathrm{K}$ respectively, while panels **(b)** and **(d)** depict the thermal transport voltages $V_{\mathrm{det}}^{\mathrm{therm}}$ due to the spin Seebeck effect at those same temperatures. For all points, the error bars are the standard deviation of the five sequential measurements performed for each angle. Forward and backward rotation data points are drawn separately. In each panel, the fits for $V_{\mathrm{det}}^{\mathrm{SHE}}$ and $V_{\mathrm{det}}^{\mathrm{therm}}$ to the $+15\,\mathrm{dBm}$ dataset according to Eqs. (3.8) and (3.9) are shown as a continuous red line.
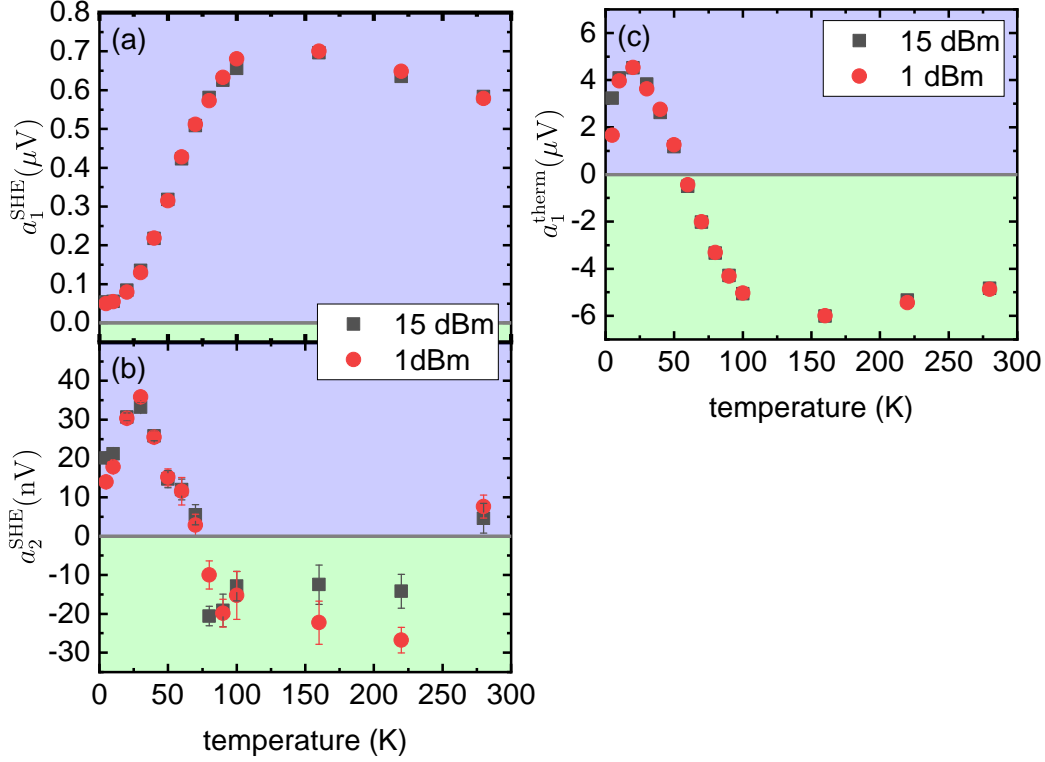
Figure 3.5: Temperature dependence of the amplitudes of the SHE and Joule-heating induced magnon transport voltages extracted from the fit-functions (3.8) and (3.9). Panels **(a)** and **(b)** show the amplitudes for the SHE induced magnon transport $a_{1,2}^{\mathrm{SHE}}$, while panel **(c)** depicts the amplitude of the Joule-heating induced magnon transport a_1^{therm}. All three panels show data acquired at one low microwave power ($+1\,\mathrm{dBm}$) and one high microwave power ($+15\,\mathrm{dBm}$). Background colors are added for better visibility of the sign-change of the amplitudes.

used to generate the fit curves depicted as red lines in panels (a) and (c) of Fig. 3.4, yielding the two amplitude parameters a_1^{SHE} and a_2^{SHE}.

The amplitudes found by fitting $V_{\mathrm{det}}^{\mathrm{SHE}}$ to Eq. (3.8) are then plotted as a function of temperature in panels (a) and (b) of Fig. 3.5. Comparing the data points for $+1\,\mathrm{dBm}$ and $+15\,\mathrm{dBm}$, no significant change is observed, which indicates, that there are no effects related to the microwave magnetic field generated by the antenna. We observe, that the amplitudes a_1^{SHE} of the $\sin^2$-contribution are about an order of magnitude larger, than the amplitudes a_2^{SHE} of the sin-contribution. Comparable with literature [Goe+15], we observe an increase of the amplitude a_1^{SHE} with increasing temperature, which corresponds to the magnon spin transport voltage. Contrary to this publication however, we observe a saturation of a_1^{SHE} at around 100 K. A more

in depth discussion about the effects at play here is given below, when the power law dependence is analyzed.

Furthermore, we note that the amplitude a_1^{SHE} at $280\,\mathrm{K}$ is of a comparable magnitude to other publications [Wim+19a; Güc+20; Rub21] (taking into account the varying driving currents and device geometries). This is surprising, because the YIG films used in this thesis are much thicker than the $d \propto 10\,\mathrm{nm}$ thin films investigated in literature and we expect worse magnon transport signals from thicker films according to Ref. [Wei+22].

The physical origin of the observed deviation from a pure $\sin^2$-dependence in the SHE induced magnon transport ADMR data is discussed in the following. A first possible reason is a leakage of a part of the Joule-heating induced magnon transport voltage $V_{\mathrm{det}}^{\mathrm{therm}}$ into the first harmonic of the lock-in amplifier, which we attribute to the SHE induced magnon transport voltage $V_{\mathrm{det}}^{\mathrm{SHE}}$. This is corroborated by the qualitatively very similar temperature behavior of the two sin-term amplitudes a_2^{SHE} and a_1^{therm} displayed in panels (b) and (c) of Fig. 3.5, respectively. It remains unclear, why such features have not previously been observed in similar experiments [Wim+19a; Wim21; Güc+20; Rub21]. One possible reason might be a crosstalk between the injector and detector Pt-strips, which is enhanced by a capacitive coupling effect between Pt-strips mediated by the microwave antenna.

A second possible origin for the sine-shaped second term in the SHE induced ADMR data is the spin-Peltier effect (SPE), first observed by Flipse et al. in magnetic insulators in 2014 [Fli+14]. The SPE refers to the generation of a heat current from a spin current flowing through the Pt/YIG-interface. The temperature modulation ΔT generated by the SPE shows a sine-dependence [IU18] on the angle between the effective magnetic field $\mathbf{H}_{\mathrm{eff}}$ and the charge current density $\mathbf{j}_{\mathrm{c}}$. This is the same angle dependence observed in the additional term of the ADMR measurements of $V_{\mathrm{det}}^{\mathrm{SHE}}$, which would explain the additional sine-term. To sum it up, the SHE induced spin current passing the Pt/YIG-interface creates a heat current, which in turn generates magnons similar to the Joule-heating process. The thereby created magnons are then transported to the detector Pt-strip and detected in the first harmonic of the lock-in amplifier as a thermovoltage, because their generation depends on the direction of the effective magnetic field $\mathbf{H}_{\mathrm{eff}}$, like the magnons created by the SHE. Yet, further experiments are required to clearly identify the origin of this additional contribution.

The Joule-heating induced magnon transport data, that is extracted from the second harmonic of the lock-in amplifier data, is shown in panels (b) and (d) of Fig. 3.4. We again fit the data, this time using a sin-dependence with the fit function

$$V_{\mathrm{det}}^{\mathrm{therm}} = y_0 + a_1^{\mathrm{therm}} \sin(\phi_1 + \phi), \tag{3.9}$$

where y_0 is a finite voltage offset and ϕ_1 is a finite phase shift. From those fits, we extract the amplitudes of the waveform as a function of temperature for both measured microwave power levels and plot the resulting a_1^{therm} in panel (c) of Fig. 3.5.

It is apparent from Fig. 3.5, that the amplitude of the Joule-heating induced
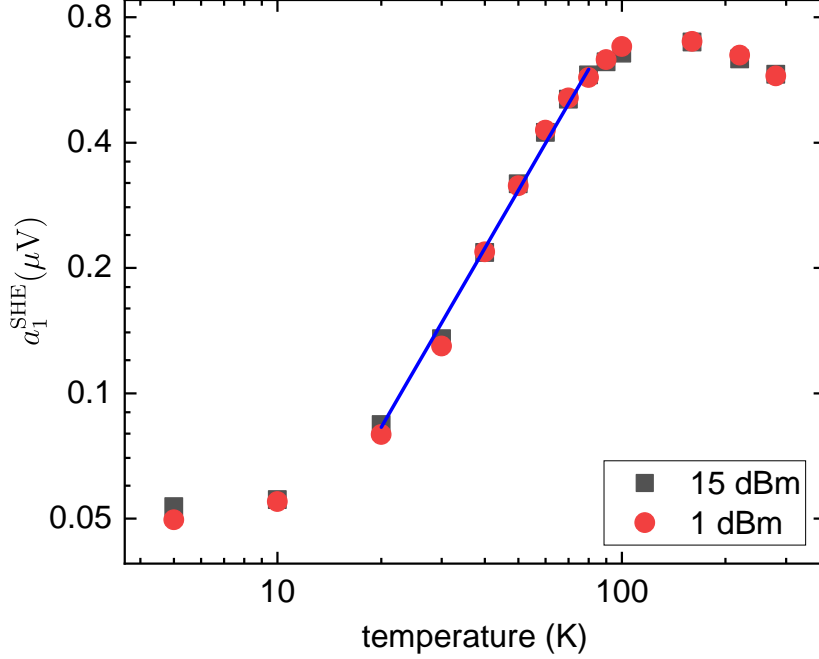
Figure 3.6: Amplitude a_1^{SHE} plotted as a function of temperature on a double logarithmic scale. From a fit of the linear part of this plot, we extract a power law dependence. From the blue linear fit for the $+15\,\mathrm{dBm}$ data, we extract $s = (1.42 \pm 0.05)$.

magnon transport contribution a_1^{therm} changes sign between $50\,\mathrm{K}$ and $60\,\mathrm{K}$. This temperature range is in good agreement with the results reported by Ganzhorn et al. [Gan+17] for devices with a similar injector/detector distance and YIG thickness. In the data shown by them, the sign change of the amplitude of the SSE-induced magnon transport occurs between $50\,\mathrm{K}$ and $100\,\mathrm{K}$. Comparing our data to another paper by Guo et al. [Guo+16], we compare the temperature dependence of the thermal transport amplitude above $50\,\mathrm{K}$ to their data for a $1.51\,\mathrm{\mu m}$ thick YIG thin film. The overall behavior, with a maximum magnitude at around $160\,\mathrm{K}$, a strong decrease in magnitude towards lower temperatures and a small decrease in magnitude towards room temperatures is very similar to our data.

To extract a power law behavior from the temperature dependence of the SHE induced magnon transport amplitudes a_1^{SHE}, in Fig. 3.6 we show a linear fit for the double logarithmic representation of the magnon spin transport amplitude a_1^{SHE} already shown in Fig. 3.4(a). From the fit, we extract the exponent of the power law $s = (1.42 \pm 0.05)$, which gives the relation between a_1^{SHE} and the temperature T via

$$a_1^{\mathrm{SHE}} \propto T^s. \tag{3.10}$$

As the amplitude of the all-electrical transport signal depends on the magnitude

of the interfacial spin current (Eq. (2.5)) and therefore the spin conductance g, it scales in the same way with temperature. For the temperature dependence of the spin conductance, we expect $g \propto (T/T_C)^{3/2}$ [ZZ12b; Cor+16], the exponent of which is in good agreement with the slope s of our fit. The range given for the exponent of the power law $s = 1...1.5$ in Ref. [Goe+15] also matches our result, although they use devices without the insulating layer and antenna.

3.2.4 Field-Sweep Magnon Transport Measurements

In this section, we focus on measurements that were conducted by sweeping the magnitude of the external magnetic field in the y-direction $\mu_0 H_y$ (cf. Figs. 3.1 and 3.3 for the coordinate system). This direction is perpendicular to the Pt-strips and lies in the sample plane. The magnetic field resolution is set to be small in magnetic field areas, where no magnon transport signal is expected above the baseline, while a finer resolution is chosen in magnetic field ranges, where a structure other than the baseline is observed. The data is acquired using the same lock-in measurement technique that is theoretically explained in Sec. 3.2.2 and with the setup shown in Sec. 3.2.1. The phase shift applied in order to rotate the data into only one of the quadratures is the same as for the ADMR measurements. We compare our data with the measurements shown by Liu et al. [Liu+19] and Rubenbauer [Rub21].

In Fig. 3.7(a), the SHE induced magnon transport voltage $V_{\mathrm{det}}^{\mathrm{SHE}}$ is plotted as a function of the magnetic field $\mu_0 H_y$ applied in the y-direction. These measurements have been conducted for several temperatures between $20\,\mathrm{K}$ and $280\,\mathrm{K}$ and for VNA output powers ranging from -1 dBm to +15 dBm. The microwave frequency is kept at $14\,\mathrm{GHz}$ for all measurements in this section. Panel (a) depicts the entire measured field range at $220\,\mathrm{K}$ and $+13\,\mathrm{dBm}$. In these measurements, the field is swept from large positive values through zero to negative values. Deviations from the baseline $\Delta V_{\mathrm{FMR}}^{\mathrm{SHE}}$ and $\Delta V_{\mathrm{param}}^{\mathrm{SHE}}$ are observed in the field range just below $\mu_0 H_{\mathrm{res}}$ of the FMR (in the following called FMR-range) and in the range, where we expect parametric pumping to occur (called parametric-range). Another dip just below $\mu_0 H_y = 0\,\mathrm{T}$ can be attributed to the switching of the magnetization direction that occurs in the YIG film. The insets (b) and (c) show the FMR-range and the parametric-range in more detail, respectively. In both insets, a fine structure in $V_{\mathrm{det}}^{\mathrm{SHE}}$ and $V_{\mathrm{det}}^{\mathrm{therm}}$ is detected. The magnitude of this signal increases with increasing microwave powers, which is discussed in more detail in Sec. 3.4.

We now turn our attention to the Joule-heating induced magnon transport voltage $V_{\mathrm{det}}^{\mathrm{therm}}$ plotted in Fig. 3.8(a) as a function of the applied magnetic field in y-direction $\mu_0 H_y$. This data represents the second harmonic voltage $V_{\mathrm{det}}^{2\omega}$ of the lock-in amplifier, which is recorded simultaneously with the data shown in Fig. 3.7(a). We measure a linear increase of the background for decreasing magnetic fields $\mu_0 H_y$. Just below $\mu_0 H_y = 0\,\mathrm{T}$, the sign of the voltage signal changes, as expected for the SSE. Insets (b) and (c) show zoom-ins for the FMR- and the parametric-range, respectively. The fine structure spacing for both magnetic field ranges in $V_{\mathrm{det}}^{\mathrm{therm}}$ is similar to the
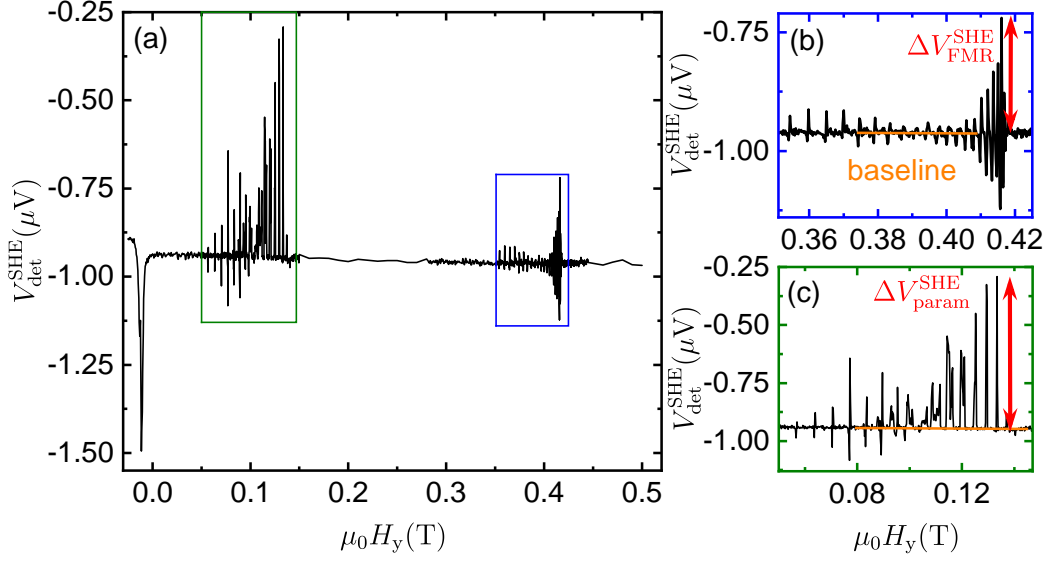
Figure 3.7: Field-sweep data of the SHE induced magnon transport voltage $V_{\text{det}}^{\text{SHE}}$. The external magnetic field points along the y-direction (cf. Fig. 3.3) and is swept from large positive values through zero. The measurement shown here has been conducted at a temperature of $220\,\text{K}$ and while applying a microwave power of $+13\,\text{dBm}$ at a frequency of $14\,\text{GHz}$. Panel **(a)** shows the entire magnetic field range, while panels **(b)** and **(c)** depict magnifications of the field range around the FMR- and in the parametric-range, respectively. Orange lines in panels (b) and (c) indicate the baseline in $V_{\text{det}}^{\text{SHE}}$, whereas red arrows represent the amplitude of the features $\Delta V_{\text{FMR}}^{\text{SHE}}$ and $\Delta V_{\text{param}}^{\text{SHE}}$, respectively.

fine structure spacing observed in the SHE induced magnon transport voltage $V_{\text{det}}^{\text{SHE}}$, hinting towards the shared physical origin of these comb-like features. In panels (b) and (c) the baseline and the maximum deviation $\Delta V_{\text{param}}^{\text{therm}}$ and $\Delta V_{\text{FMR}}^{\text{therm}}$ of the signal from this baseline are shown.

The most striking difference, when comparing our field-sweep data to the results of comparable experiments [Liu+19; Rub21], is the observed fine structure in $V_{\text{det}}^{\text{SHE}}$ and $V_{\text{det}}^{\text{SHE}}$ in both, the FMR- and the parametric-range. Both of the mentioned publications do not observe this comb-like structure. However, the used measurement geometries in these publications are different, with the microwave magnetic field generated by the antenna mostly driving the perpendicular magnetic driving field component $h_{\text{rf,oop}}$. Furthermore, the YIG samples used in their experiments are one to two orders of magnitude thinner, than the thickness $t_{\text{YIG}} = 2\,\mu\text{m}$ of the films used here. Similar to the aforementioned literature however, we observe a peak followed by a dip (peak-dip structure) for each of the fine structure elements.

For the parametric-range, Wiese et al. [Wie+94] also observe a comb-like fine structure in the microwave loss for the parallel pumping geometry. They attribute this
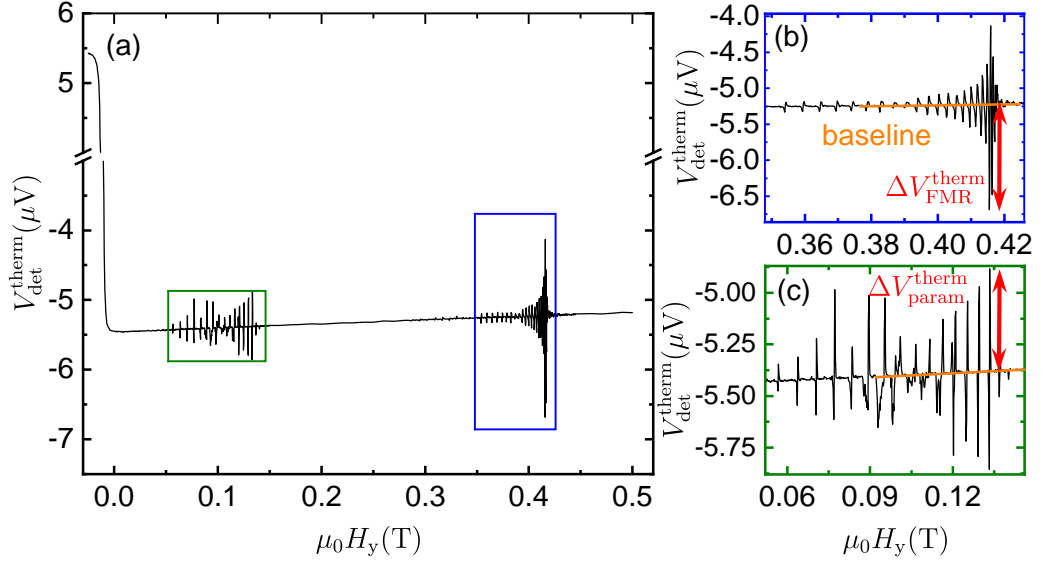
Figure 3.8: Field-sweep data of the Joule-heating induced magnon transport voltage $V_{\text{det}}^{\text{therm}}$. The external magnetic field $\mu_0 H_{\text{y}}$ points along the y-direction (cf. Fig. 3.3) and is swept from large positive values through zero. The measurement shown here has been conducted at a temperature of 220 K, while applying a microwave power of $+13$ dBm at a frequency of 14 GHz. Panel **(a)** shows the entire magnetic field range, while the insets **(b)** and **(c)** depict magnifications of the field range in the parametric-range and around FMR respectively. In the insets, the baseline and the signal magnitudes $\Delta V_{\text{param}}^{\text{SHE}}$ and $\Delta V_{\text{FMR}}^{\text{SHE}}$ are depicted.

fine structure to PSSWs (cf. Sec. 2.2.3), which are efficiently excited in the parallel pumping geometry with finite ellipticities of the magnetization precession. In the FMR-range, Klingler et al. [Kli+15] observe a fine-structure in the S-parameter data of a VNA with similar spacings to ours, the origin of which they also find to be PSSWs. Contrary to both publications however, we do not clearly observe this fine structure in the S11 data of the VNA. We discuss the observed comb-like fine structure in more detail in Sec. 3.4 for all field-sweep measurements.

Temperature and Microwave Field Dependence

From the raw field-sweep data shown in Figs. 3.7 and 3.8, we subtract a baseline (orange lines) and find the peak or dip with the largest deviation ΔV (red arrows) from this baseline. These deviations are then plotted as a function of VNA microwave output power P_{rf} in Fig. 3.9 for the parametric- and the FMR-range for both, the SHE induced and the Joule-heating induced magnon transport voltages. In order to linearize the horizontal axis, we convert the unit of the microwave power from dBm
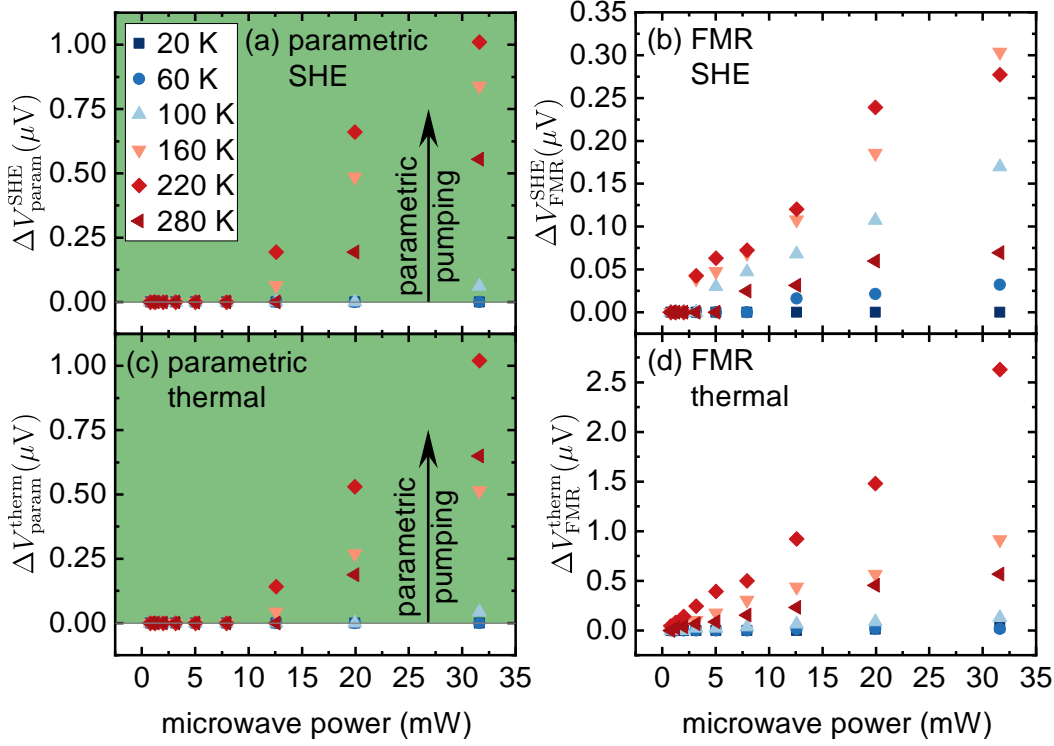
Figure 3.9: Deviation from the baseline ΔV in the field-sweep measurements for the parametric (**(a)**,**(c)**) and the FMR (**(b)**,**(d)**) magnetic field region plotted against the microwave power applied by the VNA. The two top panels show the extracted data from the SHE induced magnon transport data (Fig. 3.7), while the bottom panels are extracted from the Joule-heating induced magnon transport data (Fig. 3.8). All panels depict data of the whole measured temperature range.

into mW with

$$P_{\mathrm{rf}}^{\mathrm{mW}} = 10^{\frac{P_{\mathrm{rf}}^{\mathrm{dBm}}}{10}} \ \mathrm{mW}, \tag{3.11}$$

where $P_{\mathrm{rf}}^{\mathrm{mW}}$ and $P_{\mathrm{rf}}^{\mathrm{dBm}}$ are the microwave power levels in units of mW and dBm, respectively. Each panel shows the respective deviation from the baseline $\Delta V_{\mathrm{param}}^{\mathrm{SHE}}$, $\Delta V_{\mathrm{FMR}}^{\mathrm{SHE}}$, $\Delta V_{\mathrm{param}}^{\mathrm{therm}}$ and $\Delta V_{\mathrm{FMR}}^{\mathrm{therm}}$ as a function of microwave power for varying temperatures.

In panels (a) and (c) of Fig. 3.9, we observe, that in the parametric-range, the signal only manifests after a certain threshold microwave power is reached. This threshold behavior points to either parallel pumping or the first order Suhl instability (Sec. 2.2.4) as the possible origins of this behavior. However, the observed fine structure generated by PSSWs points toward parallel pumping as the origin as discussed in more detail in Ref. [Wie+94]. Moreover, by comparing the critical pumping field

for parallel pumping $h_{\mathrm{crit,pp}}$ (Eq. (2.32)) with the in-plane field $h_{\mathrm{rf,ip}}$ generated by the microwave antenna (Eq. (2.9)), we find critical field values of $h_{\mathrm{crit,pp}} = 1 - 2\,\mathrm{mT}$ similar to the fields expected from the microwave power level at the observed threshold according to the Karlqvist equations (cf. Fig. 3.19). For this estimation, typical values of M_{s} and ΔH_{k} for YIG, as well as in input impedance of $Z_0 = 50\,\Omega$ and a x-y-position under the Pt-strip is chosen. However, these values have large uncertainties attached to them (especially considering that the Karlqvist equations do not take into account the different materials in our sample), which makes a clear quantitative statement impossible here. For higher power, the amplitude seems to increase linearly, but due to the limited number of data points at higher microwave powers, it is difficult to reach a definitive conclusion.

Looking at the FMR-range, which is depicted in Fig. 3.9(b) and (d), the signal magnitude increases already at lower microwave powers than in the parametric-range. We compare our data with the results presented in Ref. [Rub21] for the linear regime (note, that the data presented in Ref. [Rub21] does not exhibit a fine structure). In the linear regime (low microwave power levels, below the threshold for the second order Suhl instability), the amplitude of the peak observed in the magnetic field-sweep measurements in Ref. [Rub21] also increases strongly with increasing power. Similarly, Liu et al. [Liu+19] also observe a strong increase until at a certain microwave power, a saturation is reached. They explain this saturation by a highly nonlinear FMR, where the $k = 0$ magnons transfer their energy to magnons with finite k via the second order Suhl instability. In our data, we do not observe this saturation at high microwave powers. This suggests, that the microwave powers reached in our measurements are not sufficient to surpass the threshold magnetic field $h_{\mathrm{crit,S2}}$ for the second order Suhl instability. Because the critical field for the second order Suhl instability $h_{\mathrm{crit,S2}}$ is about two orders of magnitude smaller than that of the first order Suhl instability $h_{\mathrm{crit,S1}}$ (Sec. 2.2.4), this supports our conclusion that the features we observe in the parametric-range are indeed due to the parallel contribution $h_{\mathrm{rf,ip}}$ of the pumping field.

For the temperature dependence of $V_{\mathrm{det}}^{\mathrm{SHE}}$ and $V_{\mathrm{det}}^{\mathrm{therm}}$, we observe that the signal rises with increasing temperature, only decreasing again at $280\,\mathrm{K}$. We have to note here however, that the sample had to be remounted on the chip carrier, due to connection problems after measuring the data at $280\,\mathrm{K}$ and before measuring the remainder of the data. Thus, the quantitative differences may also be caused by this remounting procedure.

The enhancement (suppression) of the magnon transport signal, which manifests as a peak (dip), is interpreted in Ref. [Liu+19] with a magnon scattering model. They correspond the enhancement to magnons that are scattered into the chiral surface mode, while they attribute the suppression to the four magnon scattering process also known as the second order Suhl process. However, it is found in Ref. [Rub21], that the spin pumping due to the dynamically precessing magnetization might also play a role in these enhancement/suppression effects. For this reason, we analyze the

spin pumping effects with and without applying charge current bias in more detail in the next section.

3.3 Spin Pumping Experiments

Spin pumping is for example observed, when a precessing magnetization in a FMI pumps a spin current into an adjacent NM-electrode. For electrical detection, this spin current is then converted into a charge current by the ISHE, as described in more detail in Sec. 2.2.5. Here, we present measurements of the spin pumping voltage in a wide magnetic field range and at different microwave driving field power levels. Furthermore, we analyze the results of the field-sweep spin pumping measurements while applying a DC charge current bias at one of the Pt-strips. This enables us to extract the magnon transport signal from the spin pumping voltage, using the current reversal technique described in Ref. [Güc+20].

3.3.1 Experimental Setup for the Spin Pumping Measurements

The electrical setup for the spin pumping measurements is very similar to the setup employed for the magnon transport measurements. The only change made compared to the setup described in Sec. 3.2.1 is, that we removed the AC current source, the amplifier and the lock-in detector. We now connect both Pt-strips to Keithley 2182 Nanovoltmeters. During that process, the sample mounting, wirebonding and dipstick position in the cryostat is not changed.

The described measurement setup is shown in Fig. 3.10. The same structure as before is studied and the antenna remains connected to the VNA, while the Pt-strips are both connected to Nanovoltmeters in the same manner.

For the experiments conducted in Sec. 3.3.3, one of the Nanovoltmeters is removed and a DC current source (Keithley 2400 sourcemeter) is connected in its place.

3.3.2 Field-Sweep Measurements

For the experiments reported in this section, the external magnetic field in y-direction $\mu_0 H_y$ is swept from large positive values through zero to negative values. The geometry and the measurement procedure of the field-sweep measurements are the same as in Sec. 3.2.4, but for the following experiments, we simultaneously detect the spin pumping voltages V_{SP} at both Pt-strips. We name one of them Pt1 and the second one Pt2. Measurements are conducted at the same temperatures and power levels as for the magnon transport field-sweep measurements discussed in the previous section, in order to gather comparable results.

In Fig. 3.11(a) we show an overview of the entire measured field range at a temperature of $220\,\text{K}$, a microwave frequency of $14\,\text{GHz}$ and a VNA output power of $+13\,\text{dBm}$. It is clear from the plot, that the spin pumping voltages of both Pt-strips exhibit the same overall behavior, only with a constant voltage offset. For that reason,
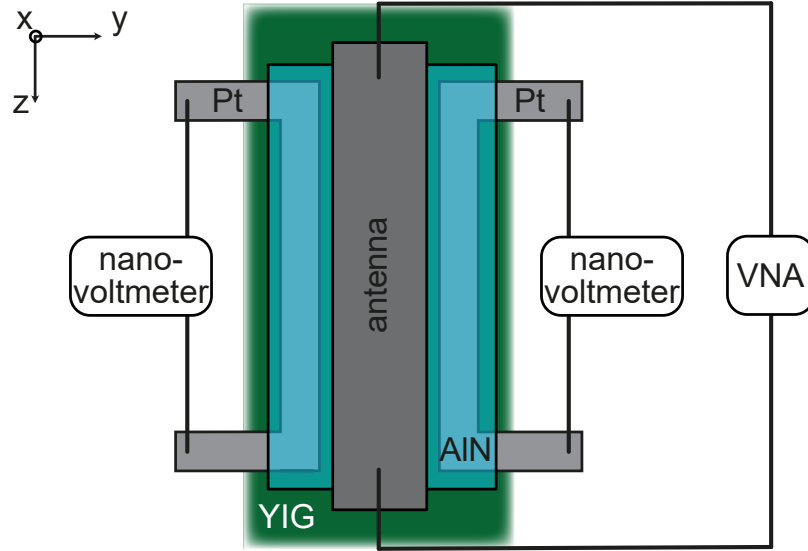
Figure 3.10: Measurement setup for the spin pumping experiments with a top down view of the measured sample geometry. Both Pt-strips are connected to separate nanovoltmeters. The microwave antenna lies on top of an insulating AlN layer, covering both Pt-strips, and is connected to the VNA. Signal and ground line of the microwave system are shorted on the sample.

the following discussion will focus on the signal from Pt1 without loss of generality. The measured voltage V_{SP} consists of a baseline due to the SSE introduced by the heating of the microwave antenna, as well as signal in the parametric- and FMR-range because of spin pumping due to the precessing magnetization. In the field range just below zero, where the magnetization of the YIG changes its direction, V_{SP} changes its polarity. This is expected due to the geometric considerations introduced in Sec. 2.1.2, as the charge current density $\mathbf{j}_c$ is perpendicular to the spin polarization, which is anti-parallel to the magnetization. Thus, inverting the magnetization direction also reverses the charge current direction. Around zero-field, the main part of the measured voltage stems from the SSE due to the heating introduced by the microwave antenna. Likewise to our experiments in Sec. 3.2.4, we once again observe a fine structure arising in the FMR- and in the parametric-range. Zoomed in depictions of V_{SP} in the FMR- and parametric-range are shown in panels (b) and (c) of Fig. 3.11. This fine structure only emerges above a certain microwave driving power in the parametric-range (cf. Fig. 3.12), again showing a similar threshold behavior as in Fig. 3.9.

Kurebayashi et al. [Kur+11] also report variations of the spin pumping voltage in the parallel pumping geometry in the parametric field range. They attribute these variations to oscillations in the threshold of the parallel pumping process. But, the
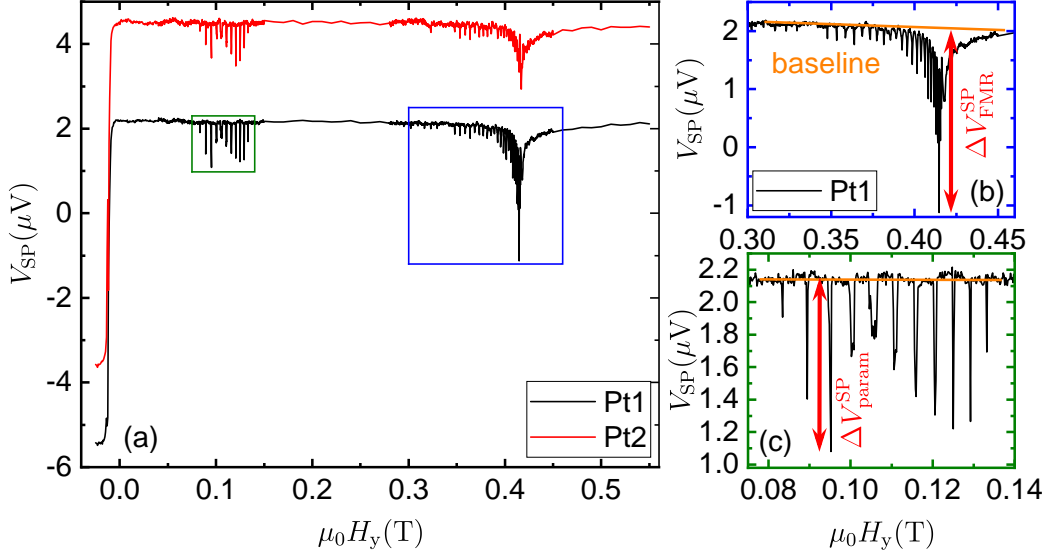
Figure 3.11: Field-sweep measurements of the spin pumping voltage V_{SP} at a temperature of $220\,\mathrm{K}$, at a microwave frequency of $14\,\mathrm{GHz}$ and with a VNA output power of $+13\,\mathrm{dBm}$. In panel **(a)**, the data for the simultaneous measurement at both Pt-strips with two separate nanovoltmeters is shown. Insets **(b)** and **(c)** depict zooms into the FMR- and the parametric-range of one of the Pt-strips, respectively. In these panels we also show the baseline (orange line) and the maximal deviation $\Delta V_{\mathrm{param}}^{\mathrm{SP}}$ and $\Delta V_{\mathrm{FMR}}^{\mathrm{SP}}$ (red arrows) of the features.

fine structure they observe is much smaller in magnitude and they also cannot relate its spacing to previously reported results [Wie+94; KKK84]. As discussed in more detail in Sec. 3.4, the comb-like fine structure observed in our measurements agrees well with the results in those two publications. The overall dip-like behavior of the spin pumping voltage V_{SP} around the FMR magnetic field is in agreement with previously reported results in similar measurements [San+10; San+11; Fan+19; Liu+19; Rub21]. Like the fine structure in the parametric-range, we correlate the comb-like fine structure in the FMR-range to PSSWs, inspired by Refs. [Kli+15; Kli+18]. A more detailed discussion of this is also given in Sec. 3.4.

In Fig. 3.12, the maximum deviations of the spin pumping voltage from the baseline $\Delta V_{\mathrm{param}}^{\mathrm{SP}}$ and $\Delta V_{\mathrm{FMR}}^{\mathrm{SP}}$ are plotted for the parametric- and the FMR-range. For the former, we only detect a signal above the noisefloor at large microwave powers, after which $\Delta V_{\mathrm{param}}^{\mathrm{SP}}$ increases linearly with microwave power. In the FMR-range however, the signal begins to increase at much lower microwave powers for all temperatures. This behavior is very similar to what we have observed in the magnon transport voltages in Sec. 3.2.4.

Furthermore, we observe a different behavior in the temperature-dependence of the spin pumping signal ΔV^{SP} compared to the magnon transport signal ΔV^{SHE} and
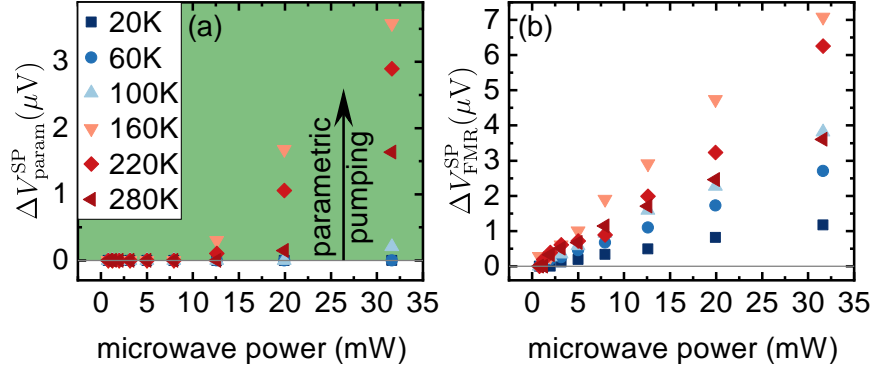
Figure 3.12: Deviation ΔV^{SP} from the baseline in the field-sweep measurements for the parametric **(a)** and the FMR **(b)** magnetic field region of the spin pumping voltage V_{SP} plotted against the microwave power applied by the VNA. Both panels depict data acquired across the entire measured temperature range.

$\Delta V^{\mathrm{therm}}$ in Sec. 3.2.4. Similarly to the magnon transport data, we again observe a peak followed by a decrease, when moving from low to high temperatures. However, for the spin pumping voltage this maximum is observed at 160 K, while it manifests at 220 K for the magnon transport measurements (cf. Fig. 3.9).

3.3.3 Spin Pumping Measurements with the Application of a DC Bias Current

In this section, we study the spin pumping voltage V_{SP} in the detector Pt-strip, while driving a DC charge current I_{bias} through the injector Pt-strip and simultaneously running a microwave charge current through the antenna. The goal of these measurements is to investigate the effect of the lock-in detection technique on the measurement. A clear separation of the signals introduced by spin pumping and by magnon transport is one of the main challenges in the data analysis, when dealing with all-electrical magnon transport measurements under the influence of an applied microwave magnetic field reported in Ref. [Rub21].

For the measurements shown in this section, one of the nanovoltmeters in Fig. 3.10 is replaced by a Keithley 2400 sourcemeter, which is used to run DC charge currents I_{bias} of varying magnitude and varying polarity through the injector Pt-strip. Likewise to the previous Sec. 3.3.2, we record the spin pumping voltage V_{SP} at the detector Pt-strip, while sweeping the external magnetic field from positive to negative values along the y-direction in the coordinate system of Fig. 3.10. We employ this approach for a number of DC charge currents at a temperature of 280 K, a microwave power of +15 dBm and a microwave frequency of 14 GHz. The results are plotted in Fig. 3.13.

We observe the same qualitative magnetic field dependence for all DC bias current measurements, but the baseline of the spin pumping voltage changes with increasing
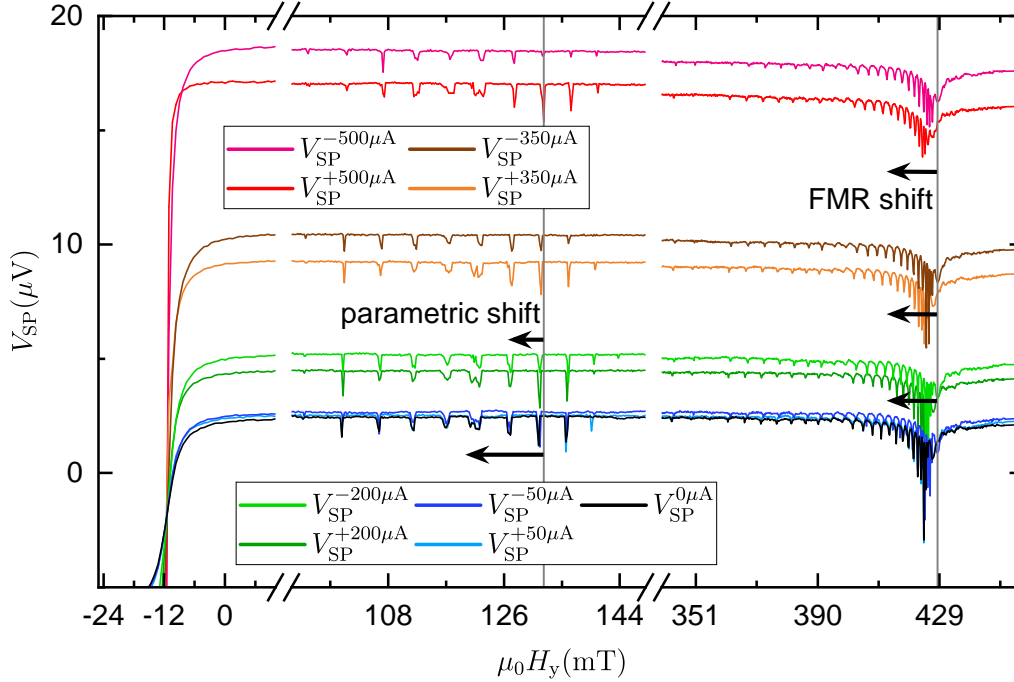
Figure 3.13: Field-sweep measurements of the spin pumping voltage V_{SP} recorded at the detector Pt-strip, while applying a DC current of varying magnitude and polarity at the injector Pt-strip. All measurements are conducted at $280\,K$ and a VNA output power of $+15\,dBm$. The gray vertical lines are introduced as a guide to the eye to compare the field positions of the observed features between the individual measurements. Arrows are introduced as a visualization of the shift in the parametric- and the FMR-range, which depend on the magnitude and the polarity of the applied DC charge current, respectively.

I_{bias}. It is expected, that the difference of the baseline in the positive magnetic field range V_{pos} and the baseline in the negative magnetic field range V_{neg} scales $\propto I_{bias}^2$, because this contribution is due to the magnons created by Joule-heating and the resulting SSE (cf. Sec. 2.1.4). Moreover, we expect the sum $V_{pos} + V_{neg}$ to scale linearly with I_{bias} as a result of the SHE induced magnon transport. In Fig. 3.14(a), both aforementioned quantities are plotted together with quadratic (blue) and linear (green) fits. From the figure it is apparent, that our theoretical considerations describe the baseline behavior very well. This leads to the conclusion, that transported magnons play a significant role on the voltage in spin pumping measurements with the simultaneous application of an injection current, as proposed in Ref. [Rub21]

We also observe a shift (FMR shift in Fig. 3.13) of the FMR-feature in the spin-pumping voltage V_{SP} in the magnetic field position, when changing the polarity of the DC current. A similar modification to the magnetic field position is also observed
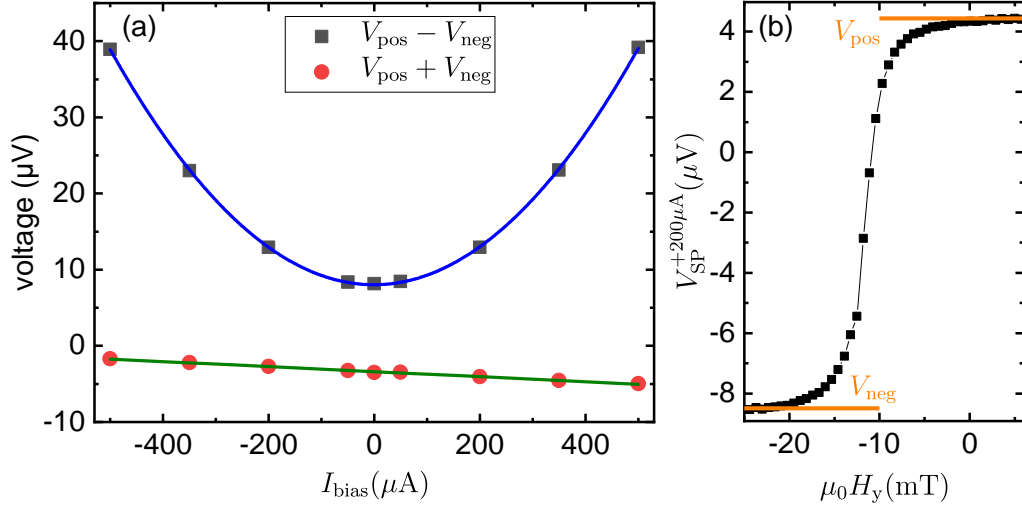
Figure 3.14: **(a)** Sum and difference of the baseline voltages in the positive magnetic field range V_{pos} and in the negative magnetic field range V_{neg}. The green and the blue lines show a linear and a quadratic fit to the data, respectively. **(b)** Baseline voltages V_{pos} and V_{neg} of the spin pumping measurement with a bias charge current of $I_{\text{bias}} = 200\,\mu\text{A}$ as an example of the baseline extraction method.

for the comb-like features in the parametric-range (parametric shift in Fig. 3.13). However, in this field range the magnitude of the DC charge current governs the magnetic field shift, while the charge current polarity does not affect the field-position of the features. From the upcoming results in the following paragraph, we attribute this variation in field-position of the FMR- and parametric-features with charge current magnitude and polarity to the magnons transported from the injector Pt-strip. The reason for this is, that the difference in peak positions leads to the signal signatures, which are identified as characteristic for the magnon transport in the following paragraph. Furthermore, we rule out Oersted-fields generated by the DC current as the origin of the observed shifts in the magnetic field position, because the generated Oersted-fields are about an order of magnitude smaller than the magnetic field shifts observed in Fig. 3.13.

Magnon Transport Analysis using the Current Reversal Technique

From the aforementioned field-sweep measurements, it is possible to conduct an analysis similar to that in Ref. [Güc+20], where the current reversal magnon transport voltages $V_{\text{dc}}^{\text{SHE,therm}}$ are compared to the magnon transport voltages measured with a lock-in measurement technique $V_{\text{det}}^{\text{SHE,therm}}$. We adapt the equations derived for the

data analysis of the current reversal technique in Ref. [Güc+20] for our case, yielding

$$V_{\text{dc}}^{\text{SHE}} = \frac{1}{2} \left(V_{\text{SP}}^{+500\mu A} - V_{\text{SP}}^{-500\mu A} \right) \tag{3.12}$$

for the SHE induced magnon transport and

$$V_{\text{dc}}^{\text{therm}} = \frac{1}{2} \left(V_{\text{SP}}^{+500\mu A} + V_{\text{SP}}^{-500\mu A} - 2V_{\text{SP}}^{0\mu A} \right) \tag{3.13}$$

for the Joule-heating induced magnon transport. Here, the superscripts represent the magnitude of the DC charge current applied at the injector Pt-strip, while measuring the spin pumping voltage V_{SP} at the detector Pt-strip. The main difference between our samples and those investigated in Ref. [Güc+20] is, that we use a microwave magnetic field for modulating the transport properties instead of a DC modulator current. Also, we only acquired these DC charge current biased spin pumping data for a single microwave power of $+15$ dBm, compared to the modulator current sweep investigated in Ref. [Güc+20].

In Fig. 3.15, a comparison between the magnon transport voltages measured with the lock-in amplifier $V_{\text{det}}^{\text{SHE}}$ and $V_{\text{det}}^{\text{therm}}$, as well as those calculated by the current reversal technique $V_{\text{dc}}^{\text{SHE}}$ and $V_{\text{dc}}^{\text{therm}}$ according to Eqs. (3.12) and (3.13) is shown. Note, that the two vertical scales differ in their absolute values, but both cover the same range of V^{SHE} and V^{therm}.

A quantitative agreement in the magnitude of the transport features within experimental uncertainty between the two measurement techniques is only found for the parametric-range of the Joule-heating induced magnon transport (Fig. 3.15(b)). There, we also need to keep in mind that the heating power output of an AC current is reduced by a factor of $\sqrt{2}$ when compared to the same DC current. This is also the reason, why the lock-in detected Joule-heating induced magnon transport voltage $V_{\text{det}}^{\text{therm}}$ is smaller in magnitude than its current reversal counterpart $V_{\text{dc}}^{\text{therm}}$. In the FMR-range of the thermal data, a good qualitative agreement is found for the signal magnitude in $V_{\text{dc}}^{\text{therm}}$ and $V_{\text{det}}^{\text{therm}}$. However, the magnitude of the signal is reduced in the lock-in data, which most likely originates from the reduced heating power of the sine-wave injection and the imperfect applied rotational correction of the signal quadratures in the lock-in signal (cf. Sec. 3.2.2).

For the SHE induced magnon transport voltage depicted in Fig. 3.15(a), we observe a qualitative agreement of the peak/dip structure induced by the PSSWs in the FMR-range, but with a much smaller feature amplitude in the lock-in data than the current reversal data. In the parametric-range, the PSSWs manifest as peaks in the lock-in data, but as dips in the current reversal data. We assume that the reason for these deviations could be the rotation of the signal phase in the lock-in measurement (cf. Sec. 3.2.2). A fraction of the signal always remains in the second channel even after the rotation, which is then discarded, reducing the signal in the channel that is plotted here.

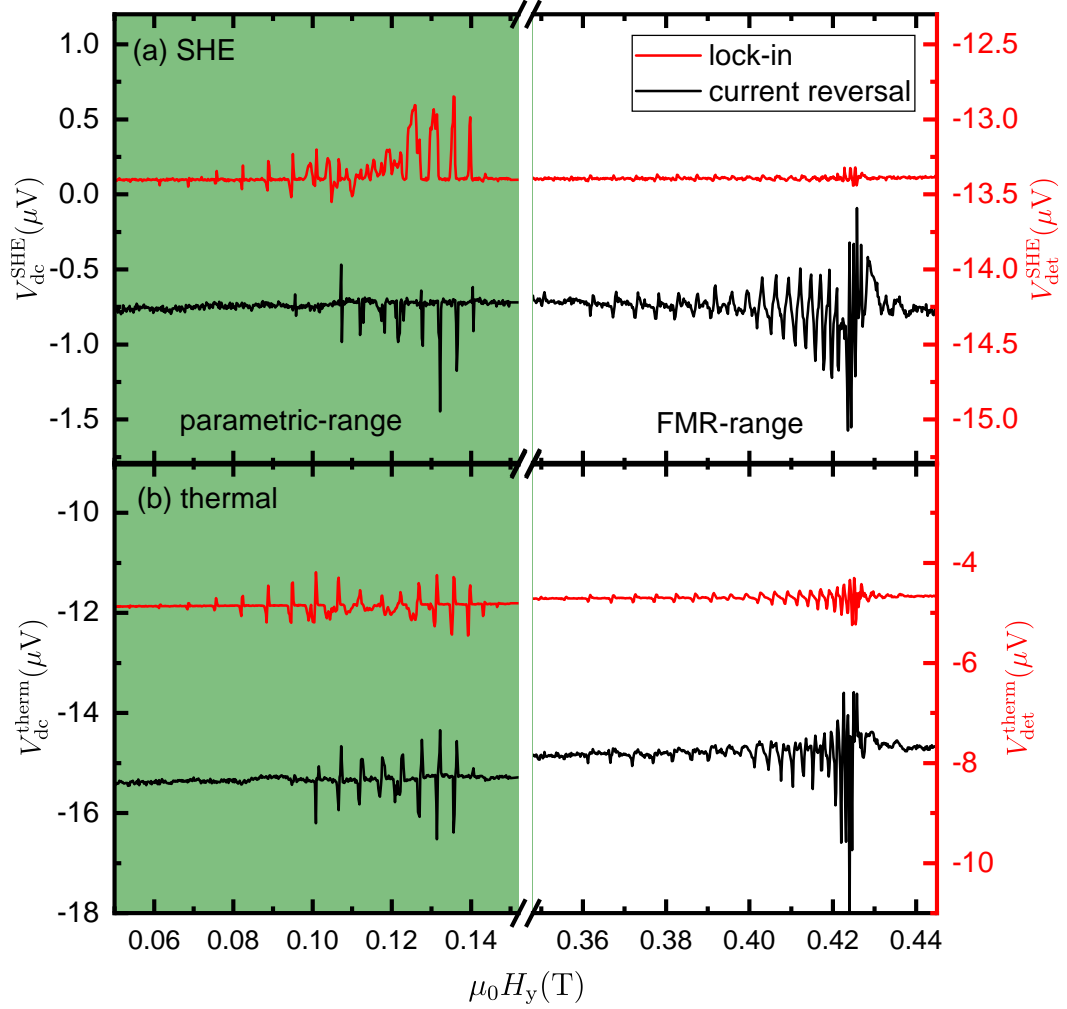Overall, a qualitative agreement is found between the two measurement techniques,

Figure 3.15: Comparison of the current reversal (black line and coordinate axis) and the lock-in (red line and coordinate axis) measurement techniques. In panel **(a)** the SHE induced magnon transport voltages $V_{\mathrm{dc,det}}^{\mathrm{SHE}}$ are depicted, while the Joule-heating induced magnon transport voltages $V_{\mathrm{dc,det}}^{\mathrm{therm}}$ are shown in panel **(b)**. For a clearer visual separation, the parametric- and the FMR-ranges are color coded green and white, respectively. All measurements are conducted at a temperature of $280\,\mathrm{K}$, a microwave output power of $+15\,\mathrm{dBm}$ and a microwave frequency of $14\,\mathrm{GHz}$.

validating the results achieved in this thesis using the lock-in measurement technique with the more basic current reversal technique. The remaining differences, which emerge between the two techniques, are not yet fully understood. In two publications [Liu+19; Rub21] utilizing a very similar measurement setup, possible shortcomings of the lock-in measurement technique are only mentioned in passing and are not analyzed in more detail. We note here, that the presence of a finite signal in the second lock-in quadrature after the phase correction cannot be excluded due to the difficult transfer of this correction from the ADMR measurements to the field-sweep measurements. This could at least partly explain the smaller signal amplitudes for the lock-in technique. From experiments with a DC modulator [Güc+20] however, we expect the lock-in and the current reversal method to yield similar quantitative results. Further comparison measurements are required for a clearer quantitative analysis of the two measurement protocols. Especially considering, that in Ref. [Güc+20] only ADMR-type measurements have been compared, whereas we analyze the results of field-sweep measurements here.

3.4 Analysis of the Fine Structure in the Field-Sweep Measurements

We now turn our focus to the fine structure, which emerges in both, magnon transport and spin pumping field-sweep FMR experiments. As already mentioned in Secs. 3.2.4 and 3.3.2, the observed comb-like fringes most likely originate from PSSWs (cf. Sec. 2.2.3). This section deals with the analysis of the observed fine structure in the parametric- and the FMR-range. Following the (different) approaches in literature for the parametric range [Wie+94; JSA72] and for the FMR-range [Kli+15], we extract the spin stiffness parameter D from the fine structure spacing and magnetic field position of the fringes. Differing from literature, we do not extract the fine structure from the S-parameters of the VNA, but from the field-sweep magnon transport voltages $V_{\mathrm{det}}^{\mathrm{SHE,therm}}$ (Figs. 3.7 and 3.8) and spin pumping voltage V_{SP} (Fig. 3.11).

For the data analysis, the magnetic field positions of the peaks/dips are extracted from the raw field-sweep data by hand for both field ranges. We start our analysis with the data extracted from the **parametric-range**, closely following the approach of Wiese et al. [Wie+94]. They find an equation for the square of the magnetic field spacing $(\delta H)^2$ of the fine structure features from the general spin wave dispersion relation given in Eq. (2.27)

$$(\delta H)^2 = C - D \left(\frac{2\pi}{d} \right)^2 H_{\mathrm{ext}}, \qquad (3.14)$$

where C is a constant, d is the thickness of the YIG and assuming that the mode number $n \gg 1$. This motivates the plot format used in Fig. 3.17, as Eq. (3.14) describes a linear dependence between the square of the fine structure spacing $(\delta H)^2$ and the external magnetic field $H_{\mathrm{ext}} = H_{\mathrm{y}}$ with a negative slope $-D(2\pi/d)^2$. Be-
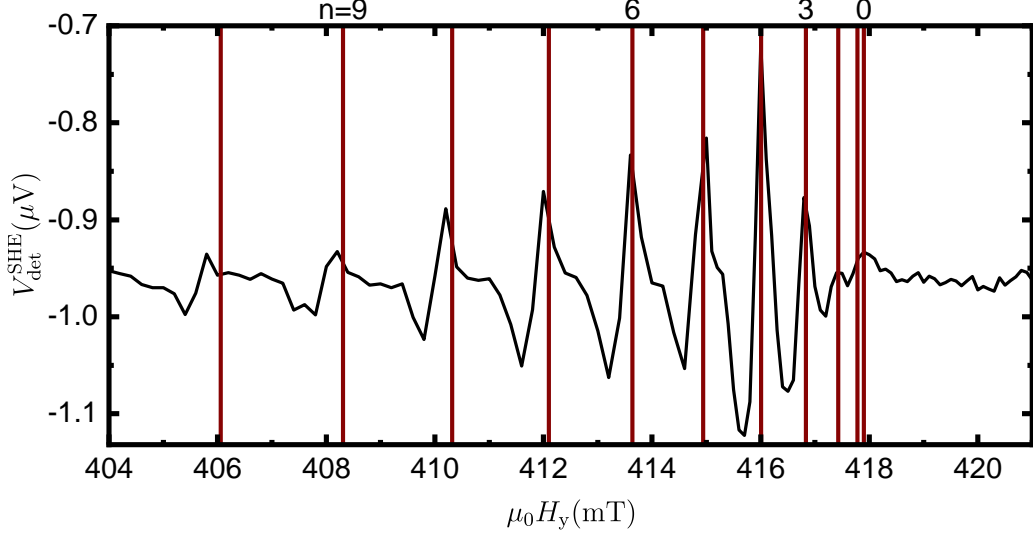
Figure 3.16: Zoom in on the region around FMR in the magnetic field-sweep measurement of the SHE induced magnon transport voltage $V_{\mathrm{det}}^{\mathrm{SHE}}$, which is also shown in Fig. 3.7. Red vertical lines show the magnetic fields, at which a PSSW resonance is expected according to Eq. (3.16), with the mode numbers n of the PSSWs given at the top of the graph.

cause we know the thickness of our YIG sample, fitting the square of the magnetic field spacing of the fringes to Eq. (3.14) allows for the extraction of the spin wave stiffness parameter D from a linear fit.

In the **FMR-range**, we follow the approach of Klingler et al. [Kli+15] to extract the spin wave stiffness parameter D from the observed fine structure around the $k = 0$ FMR-mode. They adapt and modify the established method of Schreiber and Frait [SF96], which is used to determine the spin wave stiffness parameter D from the PSSW frequency dependence on the applied out-of-plane magnetic field. Likewise, we utilize the modified method of Schreiber and Frait [Kli+15] for in-plane measurements in order to exclude the influence of internal magnetic fields. The basis for this method is to calculate the magnetic exchange field H_{ex} by subtracting the FMR resonance field $H_{\mathrm{res}}(n = 0)$ from the resonance field of the higher order PSSW modes $H_{\mathrm{res}}(n > 0)$, yielding [Kli+15]

$$\mu_0 H_{\mathrm{ex}} = \mu_0 H_{\mathrm{res}}(n) - \mu_0 H_{\mathrm{res}}(0) = D \left(\frac{\pi}{d}\right)^2 n^2. \tag{3.15}$$

From this equation, we expect a positive linear slope, when plotting the exchange magnetic field $\mu_0 H_{\mathrm{ex}}$ against the square of the mode number n^2. The slope of the fit is then equal to $D \left(\pi/d\right)^2$, from which the spin wave stiffness D can again be extracted.

In order to be able to extract the resonance fields $\mu_0 H_{\text{res}}$ as a function of the PSSW mode number n, we need to correlate peaks/dips in the magnetic field-sweep data shown in Figs. 3.7, 3.8 and 3.11 with their respective mode number n. The challenge here is, that the low order PSSW modes lie very close together in magnetic field and can not be resolved and/or the magnitude of their peak/dip is not large enough to be observed above the noisefloor. Therefore, we solve the Kalinikos-Slavin equation (2.27) for the external magnetic field $H_{\text{ext}} = H_{\text{res}}$. By inserting the expression for the PSSW wavevector $k = n\pi/d$ and in the limit $k \to 0$, which is the case for the PSSWs near FMR, we obtain

$$H_{\text{res}}(n) = \frac{1}{2}\left(-2D\left(\frac{n\pi}{d}\right)^2 - M_{\text{s}} + \frac{\sqrt{16\pi^2 f^2 + (\gamma M_{\text{s}}\mu_0)^2}}{\gamma\mu_0}\right), \qquad (3.16)$$

where $f = 14\,\text{GHz}$ is the frequency of the microwave driving field.

This equation is then used to confirm the wavenumber of the peaks observed in the field-sweep data as depicted in Fig. 3.16. There, we exemplary show the data analysis procedure for the SHE induced magnon transport voltage $V_{\text{det}}^{\text{SHE}}$. Note, that the same data analysis procedure is applied for the Joule-heating induced magnon transport voltage $V_{\text{det}}^{\text{therm}}$ and for the spin pumping voltage V_{SP} of Figs. 3.8 and 3.11. In Fig. 3.16, red vertical lines show the magnetic field positions, at which the PSSW modes are expected from Eq. (3.16). For the calculation we use a typical value for the spin wave stiffness $D = 5 \times 10^{-17}\,\text{T}\,\text{m}^2$ [Kli+15] and optimize the value of the saturation magnetization M_{s} until the $k = 0$ mode appears at the same magnetic field as the FMR peak/dip. Then, we set n in Eq. (3.16) to continuously larger integer values until the low order peaks/dips can be correlated to a mode number n. In Fig. 3.16, we observe, that the calculated resonance field and the measured peak positions start to diverge in magnetic field position at smaller magnetic fields and larger n, respectively. This is most likely due to the fact that the assumption of small k is only really valid for small n, because $k = n\pi/d$.

In Fig. 3.17 the data extracted from the fine structure in the magnetic field-sweep measurements is depicted. Panels (a)-(c) show the data from the parametric-range, where we plot the square of the fine structure spacing $(\delta H)^2$ as a function of the applied external magnetic field in y-direction $\mu_0 H_{\text{y}}$, similar to Wiese et al. [Wie+94]. Additionally, in Fig. 3.17(d)-(e), the exchange field $\mu_0 H_{\text{ex}}$ is plotted as a function of the square of the PSSW mode number n^2 as explained above. This analysis method is motivated by Ref. [Kli+15] and the supplemental material of Ref. [Kli+18]. For both, the parametric- and the FMR-range plots, the linear fit of the 220 K data is shown as an example of the fitting procedure.

By fitting the data in Fig. 3.17 for every temperature, we extract a temperature dependence of the spin stiffness parameter D using Eqs. (3.14) and (3.15), which is shown in Fig. 3.18. The error bars are calculated from the error range of the linear fits. We observe a strong deviation from the remaining data points of the spin wave stiffnesses extracted from the parametric-ranges of the SHE induced magnon
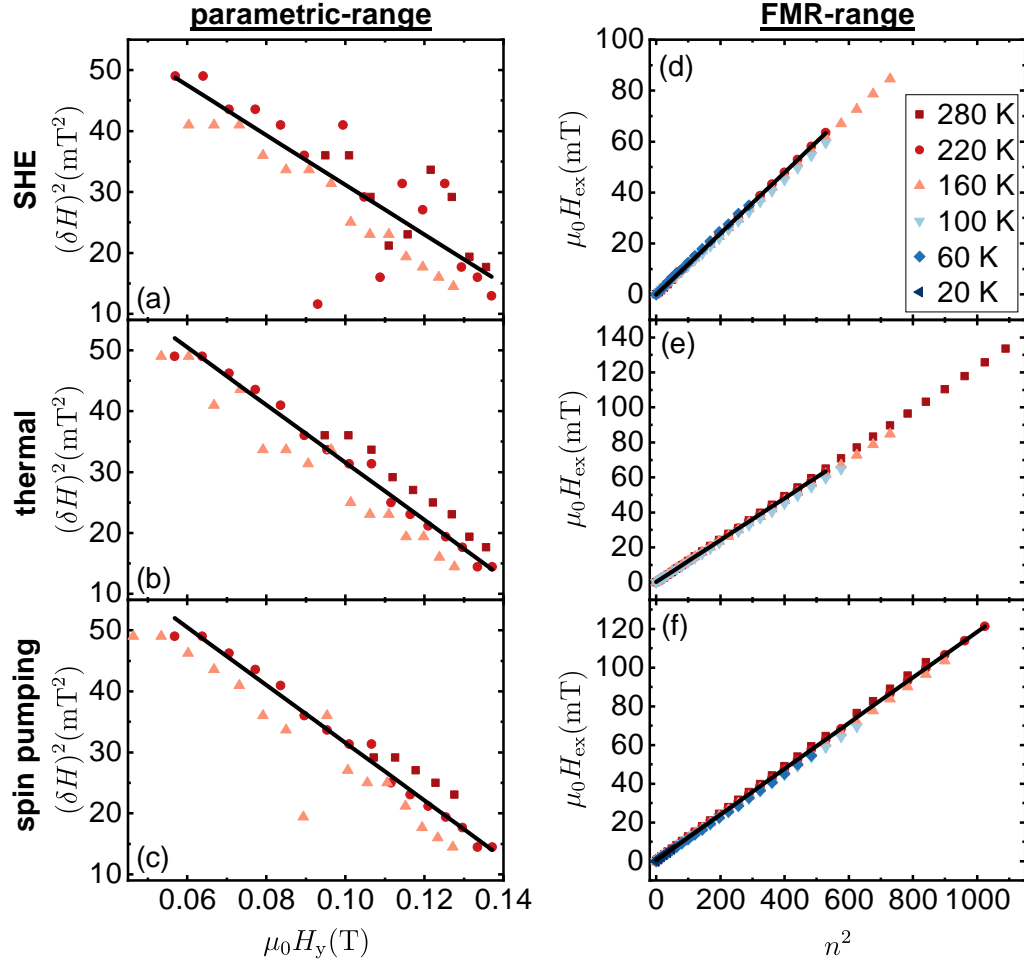
Figure 3.17: **(a)**-**(c)** Square of the fine structure spacing $(\delta H)^2$ plotted as a function of the applied magnetic field $\mu_0 H_y$ extracted from the parametric-range. **(d)**-**(f)** Exchange magnetic field $\mu_0 H_{ex}$ as a function of the square of the PSSW mode number n extracted from the FMR-range. Depicted data is extracted from the SHE (**(a)**, **(d)**) and the Joule-heating induced (**(b)**, **(e)**) magnon transport voltages V_{det}^{SHE} and V_{det}^{therm}, as well as from the spin pumping voltage V_{SP} (**(c)**, **(f)**). All panels show the data for every temperature, where a fine structure is found in the magnetic field-sweep data. Solid black lines are linear fits according to Eqs. (3.14) and (3.15) for the 220 K datasets as examples for the analysis method.
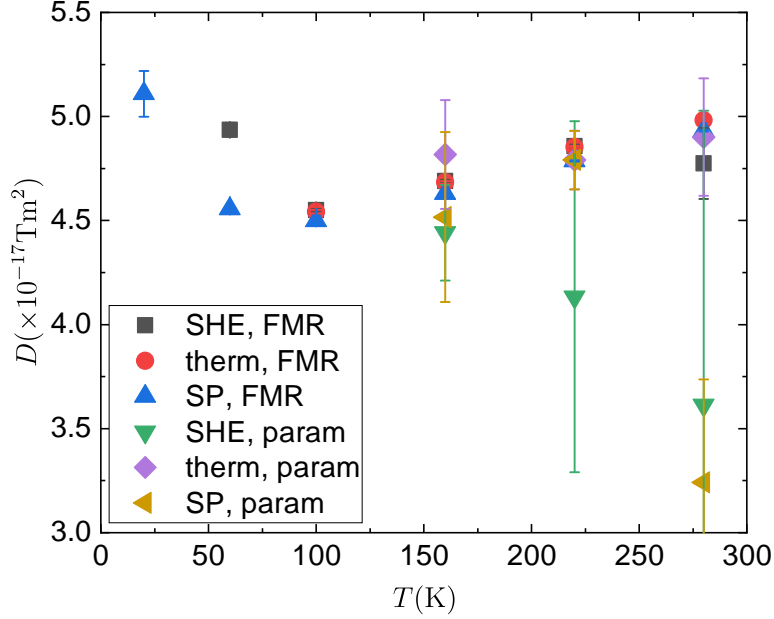
Figure 3.18: Spin wave stiffness parameters D extracted with linear fits from the data shown in Fig. 3.17 using Eqs. (3.14) and (3.15) for the parametric- and the FMR-range, respectively. The error bars are extracted from the error of the linear fits used in the analysis.

transport voltage and the spin pumping voltage. However, these data also have the largest error bars, most of which reach the rest of the data. At 280 K we extract spin stiffnesses between $D = 4.75\,\mathrm{T\,m^2}$ and $D = 5.00\,\mathrm{T\,m^2}$ from the four field-sweep measurements with reasonable error margins, which is similar to values previously reported for YIG [LW61; Wie+94; Kli+15; Kli+18] at room temperature.

For the temperature dependence of the spin wave stiffness parameter D in Fig. 3.18, we observe, that the spin wave stiffness decreases when the temperature is decreased until it appears to increase again below 100 K. In literature [LW61; SA87; CKL93], a slight decrease in D for decreasing temperature below 300 K is also reported. However, none of them report the observed increase of the spin wave stiffness parameter D at temperatures below 100 K in Fig. 3.18. A possible reason for this deviation is, that for lower temperatures, fewer PSSW resonance data points have been extracted from the magnetic field-sweep measurements, due to the smaller magnitude of the peaks/dips. This is detrimental for our analysis model and thus the error from this extraction method increases at low temperatures.
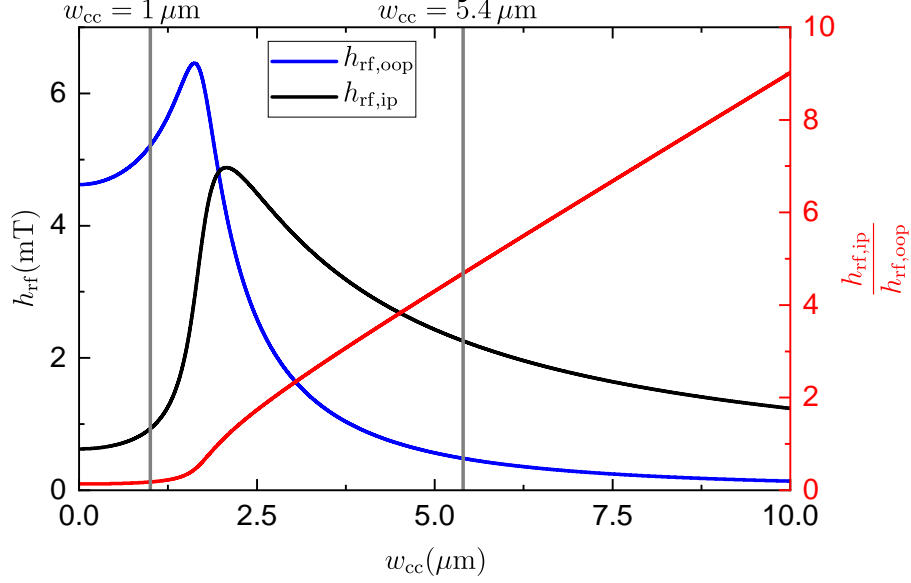
Figure 3.19: Plot of the in-plane and out-of-plane contributions to the microwave magnetic field $\mathbf{h}_{\text{rf}}$ as a function of antenna width w_{cc} according to the Karlqvist equations (2.9) at a position $x = -115\,\text{nm}$, $y = 850\,\text{nm}$ (coordinate system according to Fig. 2.5). This coordinate position represents that of the Pt/YIG-interface of the detector Pt-strip, with the x-position corresponding to the combined thickness of the AlN insulating layer and half of the antenna thickness. Also shown is the ratio of the microwave field contributions $h_{\text{rf,ip}}/h_{\text{rf,oop}}$. The vertical lines represent the experimentally realized antenna widths of $1\,\mu\text{m}$ and $5.4\,\mu\text{m}$, corresponding to the devices investigated in Secs. 3.3 and 3.5, respectively.

3.5 Spin Pumping in Structures with Antenna Covering Both Pt-Strips

The device studied in this section incorporates an antenna with a significantly larger width $w_{\text{cc}} = 5.4\,\mu\text{m}$, than the device analyzed in the previous sections. This change to the antenna design allows us to experimentally separate the in-plane ($h_{\text{rf,ip}}$) and out-of-plane ($h_{\text{rf,oop}}$) components of the magnetic microwave driving field $\mathbf{h}_{\text{rf}}$ as described by the Karlqvist equations (2.9). The effect of this changed geometry on the distribution of the microwave magnetic field is illustrated in Fig. 3.19, where the two gray vertical lines represent the width of the device discussed before ($w_{\text{cc}} = 1\,\mu\text{m}$) and the antenna width of the device measured in this section ($w_{\text{cc}} = 5.4\,\mu\text{m}$). In Fig. 3.19, the in-plane and out-of-plane components of the microwave magnetic field generated by an antenna of varying width w_{cc} are plotted using Eq. (2.9). We take the position $x = -115\,\text{nm}$, $y = 850\,\text{nm}$ at the Pt/YIG-interface of the detector Pt-strip with respect to the origin of the coordinate system at the center of the antenna

in the coordinate system introduced in Fig. 2.5. Furthermore, we assume an input impedance of $Z = 50\,\Omega$ and a microwave power of $+13\,\mathrm{dBm}$ for the calculation. The used x- and y-coordinates have been chosen to represent a point at the interface between the YIG and the Pt-strip, because the magnetization dynamics in this region governs the spin pumping signal, which is detected across the Pt-strip.

We also show the ratio $h_{\mathrm{rf,ip}}/h_{\mathrm{rf,oop}}$ in Fig. 3.19 to visualize the expected transition from a dominant oop-driving field for narrow antenna structures, to a dominant ip-driving field for structures with a wide antenna, like the antenna structure with $w_{\mathrm{cc}} = 5.4\,\mu\mathrm{m}$ used in this section. With decreasing antenna width w_{cc}, the overlap of antenna and Pt-strips decreases, thus increasing the oop-component of the magnetic driving field until it peaks, when the edge of the antenna is directly above the Pt-strip. For the $w_{\mathrm{cc}} = 1\,\mu\mathrm{m}$ wide antenna structure, the Pt-strips lie besides the antenna, which leads to a dominant oop-field contribution. Due to the inverse dependence of Eq. (2.10) on the width of the antenna w_{cc}, both $h_{\mathrm{rf,ip}}$ and $h_{\mathrm{rf,oop}}$ reduce in magnitude for large w_{cc}. This fact can be counteracted in our experiments by increasing the applied microwave power for the wider antennas. The most important result from Fig. 3.19 is the fact, that for increasing antenna widths, the in-plane component $h_{\mathrm{rf,ip}}$ of the microwave magnetic field increases relative to the out-of-plane component $h_{\mathrm{rf,oop}}$. This means, that for a good separation of the two driving field components, the antenna should be fabricated as wide as possible, while leaving the rest of the device layout unchanged.

In Fig. 3.20 an overview of the spin pumping voltage V_{SP} across the whole field range measured during the field-sweep measurements is shown for a temperature of $220\,\mathrm{K}$, a microwave frequency of $14\,\mathrm{GHz}$ and a microwave power of $+12\,\mathrm{dBm}$. As explained above, we expect a larger parallel pumping contribution in this geometry. Hence, the observed comb-like features on this sample in the parametric-range are more strongly pronounced than the features in the FMR-range. This is in contrast to the data shown in Fig. 3.11, where the peak in the FMR-range clearly dominates the fringes in the parametric-range at the same temperature. These results confirm our assumption that the comb-like features originate from PSSWs. In the parametric range, these PSSWs are mainly driven by parallel pumping, because the propagation direction of the so created spin waves is perpendicular to the effective magnetic field, as discussed in Sec. 2.2.4.

Superimposed on the comb-like structure induced by the PSSWs, we also observe a hill-like feature emerge (red line in Fig. 3.20) in the parametric-range at high microwave driving powers. This behavior is similar to previous observations in the parallel pumping regime in literature [Wie+94; AAS11; Kur+11; Man+15; Rub21]. This hill-like structure has not been observed in the spin pumping voltage of the device with the thinner antenna discussed in Sec. 3.3.2, which corroborates our assumption of a predominantly parallel pumping geometry in the relevant YIG volume of the sample with a wide antenna.

Now, we analyze the magnitude $\Delta V_{\mathrm{param}}$ and ΔV_{FMR} of the dips observed in the
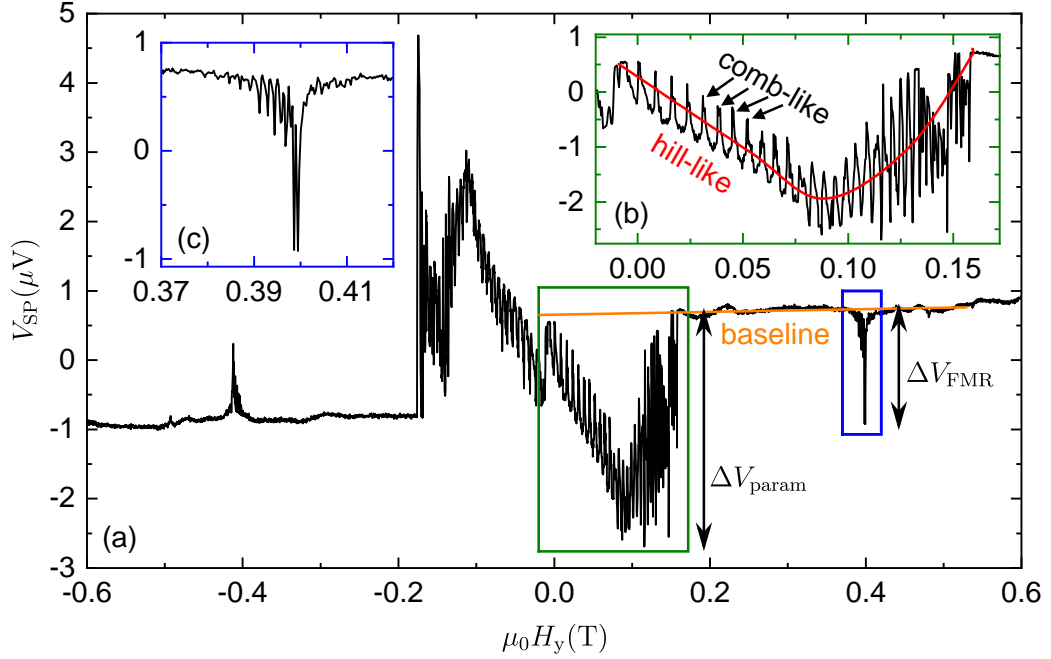
Figure 3.20: **(a)** Field-sweep measurements of the spin pumping voltage in devices with an antenna width of $w_{cc} = 5.4\,\mu m$, a Pt-strip width of $w_{Pt} = 1\,\mu m$ and an edge-to-edge distance of the two Pt-strips of $d_{Pt} = 400\,nm$. The measurement is conducted at a temperature of $220\,K$ and a microwave output power of $+12\,dBm$. Panels **(b)** and **(c)** depict zooms into the parametric- and the FMR-range respectively. In **(b)**, the hill-like and the comb-like contributions of the signal are presented as a guide for the eye.

spin pumping voltage V_{SP} in Fig. 3.20. When plotting those quantities as a function of the applied microwave driving power (Fig. 3.21), a similar behavior to that observed in Figs. 3.9 and 3.12 is observed. In the parametric magnetic field range, an increase of the magnitude only manifests at large microwave powers, while a linear increase scaling with power is observed throughout the entire experimentally investigated power range in the FMR-range. We attribute this difference in behavior to the FMR scaling linearly with the power of the driving field in the linear regime, while a threshold behavior is expected for the emergence of subsidiary peak in the parametric-range as discussed in Sec. 2.2.4.

Compared with Fig. 3.12 (narrow antenna), the subsidiary peak attributed to parallel pumping, emerges already at smaller microwave driving powers and its overall magnitude is larger, than in the data presented here in Fig. 3.21 (wide antenna). In the FMR-range, where the signal driven by the perpendicular part of the driving field, the magnitude of the dip ΔV_{FMR} is smaller than in the measurement acquired from the device using a narrow antenna structure. All of these observations are in
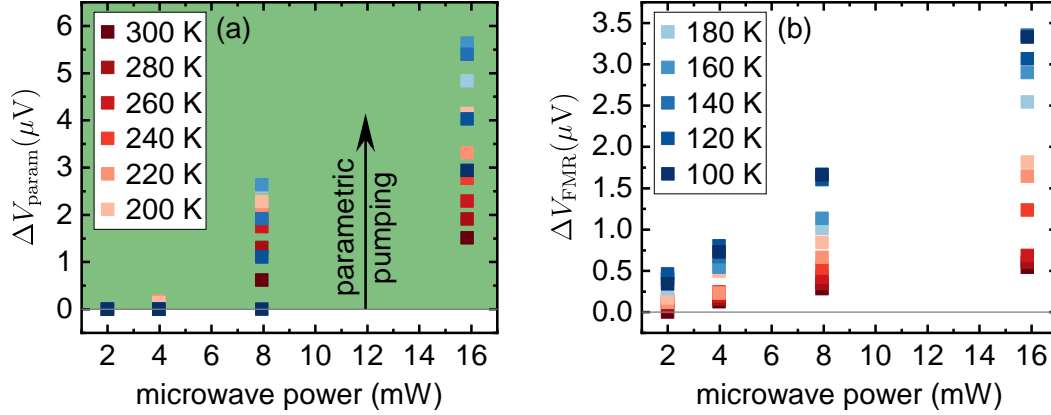
Figure 3.21: Magnitude of the dips $\Delta V_{\mathrm{param}}$ and ΔV_{FMR} extracted from the positive field branch of the spin pumping field-sweep data presented in Fig. 3.20 as a function of the applied microwave power and as a function of temperature in (a) the parametric- and (b) the FMR-range.

agreement with the aforementioned assumption from the Karlqvist equations, that a wider antenna increases the contribution from parallel pumping and decreases the contribution from perpendicular pumping. This means, that one of the main goals of this thesis, proposed in the outlook of Ref. [Rub21], has been achieved. As discussed later in the outlook (Cha. 5) however, further optimization of the fabrication is required in order to fabricate reliably working devices for magnon transport experiments with parallel pumping microwave modulation.

Finally, we turn our attention to the analysis of the comb-like fine structure, which emerges in Fig. 3.20. In Fig. 3.22, the square of the fine structure spacing $(\delta H)^2$ and the magnetic exchange field $\mu_0 H_{\mathrm{ex}}$ are plotted similar to Refs. [Wie+94; Kli+15] and Sec. 3.4, this time for a temperature series measured on the wide antenna structure. From linear fits (black lines in Fig. 3.22 exemplary show the fits for 220 K) we extract the spin wave stiffness parameters D using Eqs. (3.14) and (3.15). Then, we plot D as a function of temperature T in Fig. 3.23.

We observe from Fig. 3.23, that overall, the spin wave stiffnesses D detected on this sample are a bit smaller than the ones detected on the sample with a narrow antenna discussed in Sec. 3.4, but still very similar, considering possible experimental differences between the two samples. They are also a bit smaller than the values found in literature [Wie+94; Kli+15; Kli+18]. For the spin wave stiffnesses extracted from the FMR-range, an overall slight decrease with decreasing temperature is observed, which is in very good agreement with the trend predicted and observed in literature [LW61; SA87; CKL93]. It also matches the trend observed in our data on the structure with a narrow antenna at temperatures above 100 K (cf. Fig. 3.18). The data extracted from the parametric-range does not show a clear trend with temperature, especially considering the large error bars. The error margins are smaller for the
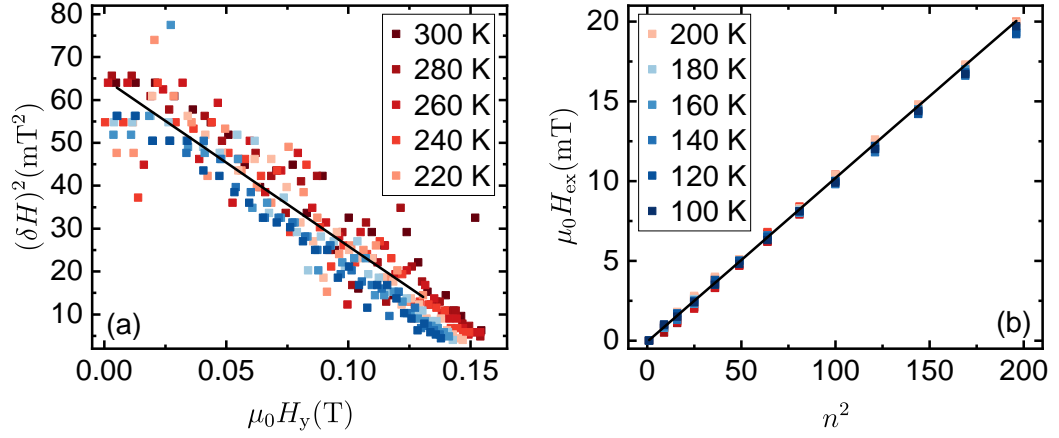
Figure 3.22: **(a)** Square of the fine structure spacing $(\delta H)^2$ plotted as a function of the applied magnetic field $\mu_0 H_\mathrm{y}$ extracted from the parametric-range. **(b)** Exchange magnetic field $\mu_0 H_\mathrm{ex}$ as a function of the square of the PSSW mode number n extracted from the FMR-range. Depicted data is extracted from field-sweep data of the spin pumping voltage V_SP as shown in Fig. 3.20. Both panels show the data for every temperature, where a fine structure is found in the magnetic field-sweep data. Solid Black lines are linear fits according to Eqs. (3.14) and (3.15) for the 220 K datasets as examples for the analysis method.
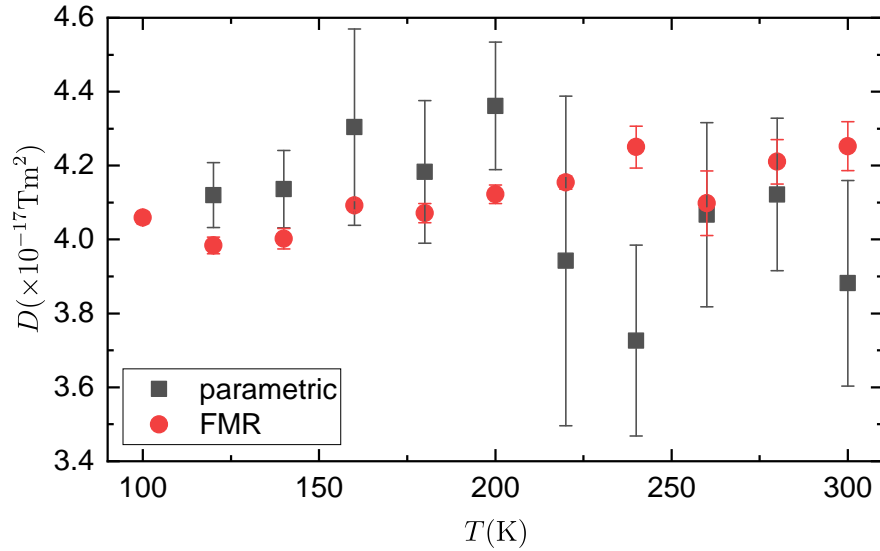

Figure 3.23: Spin wave stiffness parameters D extracted with linear fits from the data shown in Fig. 3.22 using Eqs. (3.14) and (3.15) for the parametric- and the FMR-range, respectively. The error bars stem from the error margin of the linear fits.

FMR-range compared to the parametric-range, due to the comparatively less precise peak position readout in the comb-structure of the parametric-range compared to the readout of the PSSW resonance positions in the FMR-range.

Chapter 4

Summary

In this thesis, the magnon transport and spin pumping properties, when applying microwave magnetic fields of various power levels, were investigated in three terminal all-electrical magnon transport devices on a 2 μm thick YIG layer. To this end, a great effort was put into the optimization of the sample design. In particular, we have fabricated all-electrical magnon transport devices with much wider antennas than in a previous work [Rub21] to enhance the parallel pumping efficiency, which is essential for the creation of a magnon BEC [Dem+06] and an analysis of its magnon transport properties. For the characterization of the device properties, we used the well established ADMR measurement technique, as well as field-sweep measurements of the magnon transport and spin pumping voltages. Measurements were conducted on various devices with multiple different layouts of the individual on-chip components.

As a first step, in Sec. 3.1, we have described our efforts to fabricate devices, where the main contribution to the microwave driving field generated by the antenna lies in-plane in the relevant YIG volume. This is achieved by fabricating the microwave antenna on top of an insulating spacer layer for the electronic separation of the microwave antenna from the Pt-strips serving as injector and detector of the all-electrical magnon transport experiments. Here, we found that the implementation of antennas, which overlap with the Pt-strips, is more challenging than previously expected, despite of the inclusion of a rather thick insulating layer. We suspect, that the observed breakdown of these types of devices originates from a capacitive coupling between the Pt-strips and the antenna. This experimental drawback greatly restricts the use of devices with a wide antenna in microwave modulated magnon transport experiments. However, our devices with a wider microwave antenna than in Ref. [Rub21], without overlapping with the Pt strips, already enable a much improved microwave driving field geometry. The results acquired from these devices are summed up in the following, as well as our spin pumping results from a device with a very wide antenna, pushing toward an even cleaner parallel pumping geometry.

In Sec. 3.2, we analyze the magnon transport properties of one of our devices using a lock-in detection technique. First, we quantify the efficiency of the magnon transport in our sample using the well established ADMR measurement technique, where the external magnetic field is rotated in the sample plane and the magnon transport voltages are simultaneously measured. There, we find, that the amplitudes of the transport voltages are large in comparison with literature values obtained

on comparable devices. This is a promising result for the implementation of future three terminal devices incorporating a microwave antenna, with an insulating layer patterned between the Pt-strips. On top of that, we observe an unexpected sine-contribution to the first harmonic signal of the lock-in amplifier, where a pure $\sin^2$-shape is expected. We attribute this effect to either a leakage of the Joule-heating induced magnon transport signal into the first harmonic of the lock-in amplifier or to the spin Peltier effect influencing the signal. However, further investigations into this unexpected behavior are required to discern a clear physical origin. In these ADMR measurements, we find, that the applied microwave power does not have a significant impact on the transport properties at $50\,\mathrm{mT}$. After the quantification of the magnon transport properties of our sample, we discuss the field-sweep measurements of the magnon transport voltages. There, we discover that at high microwave driving field powers, the parallel pumping regime is reached in our experiments, while we do not observe evidence of reaching the threshold for the second order Suhl instability. This opens up possibilities for future experiments on magnon transport through areas with high magnon concentrations. We also observe a comb-like fine structure in the parametric- and the FMR-range, which was not reported in previous publications [Liu+19; Rub21] and is investigated more in depth later.

Next, we analyze the spin pumping properties of our devices in Sec. 3.3. There, we measured the spin pumping voltage V_{SP} as a function of the applied magnetic field $\mu_0 H_{\mathrm{y}}$. In a first step, we show data for a simultaneous spin pumping measurement on both Pt-strips. There, we find that the overall shape of the signal agrees well with previous results [Liu+19; Rub21]. However, we again observe a comb-like fine structure superimposed on the signal in the parametric- and the FMR-range, which is not present in this literature. In a second part, we study the leakage signals observed in our results and and in Ref. [Rub21] in more detail. Therefore, we investigate the effect of applying a DC-charge current to one of the Pt-strips while again measuring the spin pumping voltage V_{SP} in the second Pt-strip. We notice that, by applying a current reversal analysis technique [Güc+20] to our data, the magnon transport voltages $V_{\mathrm{DC}}^{\mathrm{SHE}}$ and $V_{\mathrm{DC}}^{\mathrm{therm}}$ can be extracted from the spin pumping voltage V_{SP}. This confirms the assumption in Ref. [Rub21], that the magnon transport signal can not be clearly separated from the spin pumping signal, when both of those signals are measured at the same time. Furthermore, we conclude that a magnetic field shift of the features observed in the spin pumping voltage is about an order of magnitude larger than the expected shift from the Oersted-field generated by the DC-current. Therefore, we deduce, that this shift is induced by magnon transport effects.

In Sec. 3.4 the comb-like fine structure, observed in all field-sweep measurements of this thesis, is investigated in more detail, because it was not observed in the very similar measurements conducted in Refs. [Liu+19; Rub21]. We find, that the fine structure we observe originates from PSSWs and we are able to extract values for the spin wave stiffness parameter D, which are similar to previously reported values across a large temperature range [LW61; CKL93; Kli+18]. For this analysis, we use

methods previously used on VNA S-parameter data in the parametric- [Wie+94] and FMR-range [Kli+15]. We show, that these same methods are also valid for data obtained using magnon transport and spin pumping type experiments.

Finally, we close the overview of the experimental results, by comparing the afore-mentioned spin pumping data from a narrow antenna structure to data obtained on a device with a much wider antenna in Sec. 3.5. Those structures with a wider microwave antenna are expected to be favorable for parallel pumping experiments [Rub21], which is desirable for reaching magnon BECs. Here, we show, that a wider antenna does indeed increase the parallel pumping contribution as expected from the Karlqvist equations (2.9) in the spin pumping voltage V_{SP}. In these measurements, we also observe a hill-like feature in the parametric-range, which was previously also reported in parallel pumping experiments [Kur+11; Liu+19; Rub21]. These results are an important step towards the separation of the parallel pumping contribution from the perpendicular pumping contribution in all-electrical magnon transport experiments.

In conclusion, our experimental results mark an important step for the implementation of three terminal devices with wide microwave antennas. These devices are an important building block for the realization of all-electrical magnon transport experiments in a parallel pumped magnon BEC. However, our experiments also raise interesting questions for future investigations, as discussed in more detail in the following outlook section.

Chapter 5

Outlook

Separating Parallel and Perpendicular Pumping

The results presented in this thesis constitute a significant advance toward the goal of separating the effects of parallel and perpendicular pumping on the magnon transport and on spin pumping. However, experimental challenges emerged when measuring structures with antennas overlapping the Pt-strips as discussed in detail in Sec. 3.1.2. As we could show by comparing the spin pumping data of the narrow antenna structure (Sec. 3.3.2) and the wide antenna structure (Sec. 3.5), a more parallel distribution of the driving microwave field is achieved with a wider antenna. This is favorable for a separation of the effects driven by the in-plane microwave field $h_{\mathrm{rf,ip}}$ from those driven by the out-of-plane microwave field $h_{\mathrm{rf,oop}}$. In future samples an even better separation can be achieved by fabricating devices with even wider antennas than those shown in this thesis.

However, in order to be able to not only measure spin pumping but also magnon transport in these devices, the challenges listed in Sec. 3.1.2 have to be overcome. Therefore, we suggest the usage of a thicker insulating layer, in order to increase the capacitor's breakdown voltage.

With working devices employing a very wide antenna, the requirements for the microwave power level necessary to achieve the same microwave magnetic fields inside the YIG increase with the antenna width (cf. Fig. 3.19). A further increase of the power levels requires additional microwave components like amplifiers and microwave sources capable of generating a larger maximum output power. One could also improve upon the impedance matching of the on chip antenna, to further increase the power levels at the antenna. In this manner, very high magnon densities can be reached in the parallel pumping regime, with the ultimate goal of creating a magnon BEC [Dem+06; Ser+14; Cla+15]. This would allow for the investigation of magnon transport within a magnon BEC. Furthermore, it enables the comparison of this transport with well established DC current modulated magnon transport experiments [Wim+19a; Güc+20; Güc+21].

Comparison of Measurement Techniques

A comparison between the lock-in and the current reversal measurement techniques for field-sweep measurements of the magnon transport voltages is introduced in this thesis. We find in Sec. 3.3.3, that the two methods of measurement do match qualitatively, but not quantitatively. We suggest future experiments conducting a similar

analysis as in Gückelhorn et al. [Güc+20], but using a microwave magnetic field instead of a DC current as a modulator like in our experiments. The results from these measurements are essential for the understanding of signal leakages from the magnon transport signal into the spin pumping signal. This would also aid a better understanding of the measurement artifacts already reported with the lock-in technique in Ref. [Rub21].

Novel Device Layouts

A clear separation of the effects of the SHE induced magnon transport, Joule-heating induced magnon transport, spin pumping and Oersted-fields represents another major challenge for future experiments. Within the framework of this thesis, some progress has been made in this direction, but as discussed in multiple sections of this thesis, a quantitative analysis remains challenging. Therefore one proposal for future experiments is to use more sophisticated device layouts, incorporating materials with opposite spin Hall angle polarities. One possible candidate is Tantalum (Ta), because of its negative spin Hall angle [Mor+11] and its availability in the SUPERBOWL sputtering system at WMI. Another possible material for these experiments would be Vanadium, where a negative spin Hall angle of similar magnitude as in Pt has been reported [Wan+17], which increases the signal differentiation of the following discussion even more. One could also use an Al-injector to "shut off" the SHE induced magnon injection, because Aluminum possesses a vanishingly small spin Hall angle, leaving only the Joule-heating induced magnon transport. In the following discussion we focus on devices with a dual-injector setup, consisting of Ta and Pt.

A first sample with a novel device layout combining Pt- and Ta-strips in the same device has already been manufactured, but could not be measured in more detail in this thesis. In Fig. 5.1 the device layout is shown schematically. Here, one long detector Pt-strip is separated by an antenna from the injection Pt- and Ta-strips. The injector strips are electrically connected such that running a current through them will result in an antiparallel current flow through the strips. For these devices, the antenna is not fabricated on top of an insulating spacer layer, but rather directly on top of the YIG in between the strips. A different material stack of $Ru(7\,nm)/Cu(75\,nm)/Ta(3\,nm)$ is used for this antenna the same reasons as in Ref. [Rub21]. For future devices, the fabrication of the microwave antenna on top of an insulating layer in a similar fashion to the other devices investigated in this thesis could be envisioned. By running charge currents of opposite directions through the injector strips, the total SHE-induced magnon injection is enhanced for one charge current polarity, while the magnon depletion is enhanced for the other charge current polarity. This is due to the different signs of the spin Hall angles of Pt and Ta, canceling out the different signs due to the opposite current directions in Eq. (2.3), while the magnetic Oersted-fields surrounding the two injector strips are oriented in opposite directions. Therefore we expect their effects on the detector side to cancel each other out, enabling the separation of the Oersted signal from the magnon transport signals.
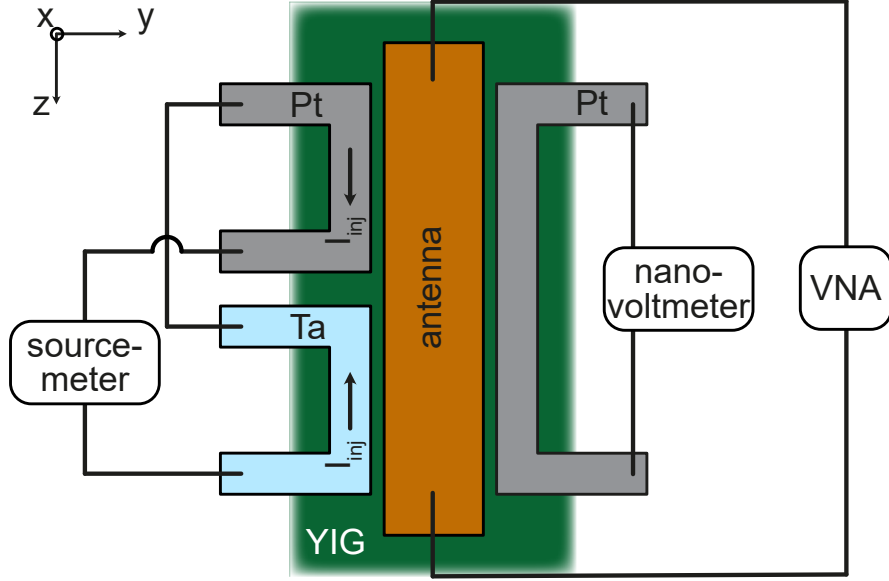
Figure 5.1: Schematic overview of the device layout with a combination of Pt- and Ta-strips. Also shown is the electronic setup proposed to generate antiparallel injector currents in the left Pt- and Ta-strips. The antenna is fabricated as a multi-layer stack of $Ru(7\,nm)/Cu(75\,nm)/Ta(3\,nm)$, which is sputtered directly onto the YIG. The second Pt-strip is connected to a nanovoltmeter for the detection of the magnons via the ISHE.

Following up on this, we envision the realization of a large range of these devices with multiple different injector/detector materials. For example, in a similar device with two identical injector Pt-Strips, the SHE induced magnon injection should be completely suppressed.

In conclusion, the results presented in this thesis further the understanding of microwave manipulated magnon transport and spin pumping in three terminal devices, while also provoking many new questions for future exploration.

Bibliography

[AAS11]   K. Ando, T. An and E. Saitoh. 'Nonlinear spin pumping induced by parametric excitation'. In: *Applied Physics Letters* 99 (2011), p. 092510.

[Alt+13]   Matthias Althammer, Sibylle Meyer, Hiroyasu Nakayama, Michael Schreier, Stephan Altmannshofer, Mathias Weiler, Hans Huebl, Stephan Geprägs, Matthias Opel, Rudolf Gross, Daniel Meier, Christoph Klewe, Timo Kuschel, Jan-Michael Schmalhorst, Günter Reiss, Liming Shen, Arunava Gupta, Yan-Ting Chen, Gerrit E. W. Bauer, Eiji Saitoh and Sebastian T. B. Goennenwein. 'Quantitative study of the spin Hall magnetoresistance in ferromagnetic insulator/normal metal hybrids'. In: *Physical Review B* 87 (2013), p. 224401.

[Alt18]   Matthias Althammer. 'Pure spin currents in magnetically ordered insulator/normal metal heterostructures'. In: *Journal of Physics D: Applied Physics* 51 (2018), p. 313001.

[Ber96]   L. Berger. 'Emission of spin waves by a magnetic multilayer traversed by a current'. In: *Physical Review B* 54 (1996), pp. 9353–9358.

[Bha+17]   Sabpreet Bhatti, Rachid Sbiaa, Atsufumi Hirohata, Hideo Ohno, Shunsuke Fukami and S. N. Piramanayagam. 'Spintronics based random access memory: a review'. In: *Materials Today* 20 (2017), pp. 530–548.

[BPH17]   T. Brächer, P. Pirro and B. Hillebrands. 'Parallel pumping for magnon spintronics: Amplification and manipulation of magnon spin currents on the micron-scale'. In: *Physics Reports* 699 (2017), pp. 1–34.

[Bra+20]   Arne Brataas, Bart van Wees, Olivier Klein, Grégoire de Loubens and Michel Viret. 'Spin insulatronics'. In: *Physics Reports*. Spin Insulatronics 885 (2020), pp. 1–27.

[BT15]   Scott A. Bender and Yaroslav Tserkovnyak. 'Interfacial spin and heat transfer between metals and magnetic insulators'. In: *Physical Review B* 91 (2015), p. 140402.

[BW54]   N. Bloembergen and S. Wang. 'Relaxation Effects in Para- and Ferromagnetic Resonance'. In: *Physical Review* 93 (1954), pp. 72–83.

[Che+13]   Yan-Ting Chen, Saburo Takahashi, Hiroyasu Nakayama, Matthias Althammer, Sebastian T. B. Goennenwein, Eiji Saitoh and Gerrit E. W. Bauer. 'Theory of spin Hall magnetoresistance'. In: *Physical Review B* 87 (2013), p. 144411.

[CKL93]   Vladimir Cherepanov, Igor Kolokolov and Victor L'vov. 'The saga of YIG: Spectra, thermodynamics, interaction and relaxation of magnons in a complex magnet'. In: *Physics Reports* 229 (1993), pp. 81–144.

[Cla+15]   P. Clausen, D. A. Bozhko, V. I. Vasyuchka, B. Hillebrands, G. A. Melkov and A. A. Serga. 'Stimulated thermalization of a parametrically driven magnon gas as a prerequisite for Bose-Einstein magnon condensation'. In: *Physical Review B* 91 (2015), p. 220402.

[Coe10]   J. M. D. Coey. 'Magnetism and Magnetic Materials'. Cambridge: Cambridge University Press, 2010. ISBN: 978-0-521-81614-4.

[Cor+15]   L. J. Cornelissen, J. Liu, R. A. Duine, J. Ben Youssef and B. J. van Wees. 'Long-distance transport of magnon spin information in a magnetic insulator at room temperature'. In: *Nature Physics* 11 (2015), pp. 1022–1026.

[Cor+16]   L. J. Cornelissen, K. J. H. Peters, G. E. W. Bauer, R. A. Duine and B. J. van Wees. 'Magnon spin transport driven by the magnon chemical potential in a magnetic insulator'. In: *Physical Review B* 94 (2016), p. 014412.

[Cor+18]   L. J. Cornelissen, J. Liu, B. J. van Wees and R. A. Duine. 'Spin-Current-Controlled Modulation of the Magnon Spin Conductance in a Three-Terminal Magnon Transistor'. In: *Physical Review Letters* 120 (2018), p. 097702.

[CSH14]   A. V. Chumak, A. A. Serga and B. Hillebrands. 'Magnon transistor for all-magnon data processing'. In: *Nat Commun* 5 (2014), p. 4700.

[Cze11]   Franz Dominik Czeschka. 'Spin Currents in Metallic Nanostructures'. PhD-Thesis. 2011.

[Dam53]   R. W. Damon. 'Relaxation Effects in the Ferromagnetic Resonance'. In: *Reviews of Modern Physics* 25 (1953), pp. 239–245.

[Dem+06]   S. O. Demokritov, V. E. Demidov, O. Dzyapko, G. A. Melkov, A. A. Serga, B. Hillebrands and A. N. Slavin. 'Bose-Einstein condensation of quasi-equilibrium magnons at room temperature under pumping'. In: *Nature* 443 (2006), pp. 430–3.

[DP71]   M. I. Dyakonov and V. I. Perel. 'Current-induced spin orientation of electrons in semiconductors'. In: *Physics Letters A* 35 (1971), pp. 459–460.

[Fan+19]   Yabin Fan, Justin T. Hou, Joseph Finley, Se Kwon Kim, Yaroslav Tserkovnyak and Luqiao Liu. 'Electrical manipulation of spin pumping signal through nonlocal thermal magnon transport'. In: *Applied Physics Letters* 115 (2019), p. 172405.

[Fli+14]   J. Flipse, F. K. Dejene, D. Wagenaar, G. E. W. Bauer, J. Ben Youssef and B. J. van Wees. 'Observation of the Spin Peltier Effect for Magnetic Insulators'. In: *Physical Review Letters* 113 (2014), p. 027601.

[Gan+16]   Kathrin Ganzhorn, Stefan Klingler, Tobias Wimmer, Stephan Geprägs, Rudolf Gross, Hans Huebl and Sebastian T. B. Goennenwein. 'Magnon-based logic in a multi-terminal YIG/Pt nanostructure'. In: *Applied Physics Letters* 109 (2016), p. 022405.

[Gan+17]   Kathrin Ganzhorn, Tobias Wimmer, Joel Cramer, Richard Schlitz, Stephan Geprägs, Gerhard Jakob, Rudolf Gross, Hans Huebl, Mathias Kläui and Sebastian T. B. Goennenwein. 'Temperature dependence of the non-local spin Seebeck effect in YIG/Pt nanostructures'. In: *AIP Advances* 7 (2017), p. 085102.

[Gil04]   T.L. Gilbert. 'Classics in Magnetics A Phenomenological Theory of Damping in Ferromagnetic Materials'. In: *IEEE Transactions on Magnetics* 40 (2004), pp. 3443–3449.

[GM18]   Rudolf Gross and Achim Marx. 'Festkörperphysik'. De Gruyter, 2018. ISBN: 978-3-11-055918-7.

[Gmb22]   GenISys GmbH. *BEAMER, TRACER*. 2022.

[Goe+15]   Sebastian T. B. Goennenwein, Richard Schlitz, Matthias Pernpeintner, Kathrin Ganzhorn, Matthias Althammer, Rudolf Gross and Hans Huebl. 'Non-local magnetoresistance in YIG/Pt nanostructures'. In: *Applied Physics Letters* 107 (2015), p. 172405.

[Güc+20]   J. Gückelhorn, T. Wimmer, S. Geprägs, H. Huebl, R. Gross and M. Althammer. 'Quantitative comparison of magnon transport experiments in three-terminal YIG/Pt nanostructures acquired via dc and ac detection techniques'. In: *Applied Physics Letters* 117 (2020), p. 182401.

[Güc+21]   J. Gückelhorn, T. Wimmer, M. Müller, S. Geprägs, H. Huebl, R. Gross and M. Althammer. 'Magnon transport in Y3Fe5O12 nanostructures with reduced effective magnetization'. In: *Physical Review B* 104 (2021), p. L180410.

[Guo+16]   Er-Jia Guo, Joel Cramer, Andreas Kehlberger, Ciaran A. Ferguson, Donald A. MacLaren, Gerhard Jakob and Mathias Kläui. 'Influence of Thickness and Interface on the Low-Temperature Enhancement of the Spin Seebeck Effect in YIG Films'. In: *Physical Review X* 6 (2016), p. 031012.

[Hei26]   W. Heisenberg. 'Mehrkörperproblem und Resonanz in der Quantenmechanik'. de. In: *Zeitschrift für Physik* 38 (1926), pp. 411–426.

[Hen+73]   R. Henry, P. Besser, D. Heinz and J. Mee. 'Ferromagnetic resonance properties of LPE YIG films'. In: *IEEE Transactions on Magnetics* 9 (1973), pp. 535–537.

[Hir99]   J. E. Hirsch. 'Spin Hall Effect'. In: *Physical Review Letters* 83 (1999), pp. 1834–1837.

[IU18]   Ryo Iguchi and Ken-ichi Uchida. 'Charge-current angle and frequency dependences of the spin Peltier effect induced by the spin Hall effect'. In: *Japanese Journal of Applied Physics* 57 (2018), 0902B6.

[JSA72]   W. Jantz, J. Schneider and B. Andlauer. 'Fine structure of the parallel pump instability in YIG'. In: *Solid State Communications* 10 (1972), pp. 937–940.

[Kar54]   O. Karlqvist. 'Calculation of the Magnetic Field in the Ferromagnetic Layer of a Magnetic Drum'. Acta polytechnica. Elanders boktr.; [H. Lindståhls bokhandel i distribution, 1954.

[Kat+04]   Y. K. Kato, R. C. Myers, A. C. Gossard and D. D. Awschalom. 'Observation of the Spin Hall Effect in Semiconductors'. In: *Science* 306 (2004), pp. 1910–1913.

[Kit48]   Charles Kittel. 'On the Theory of Ferromagnetic Resonance Absorption'. In: *Physical Review* 73 (1948), pp. 155–161.

[KKK84]   B. A. Kalinikos, N. G. Kovshikov and N. V. Kozhus. 'Determination of the instability threshold of standing spin waves in YIG films subjected to longitudinal pumping'. In: *Sov. Phys. Solid State* 27 (1984), p. 1681.

[Kli+15]   S. Klingler, A. V. Chumak, T. Mewes, B. Khodadadi, C. Mewes, C. Dubs, O. Surzhenko, B. Hillebrands and A. Conca. 'Measurements of the exchange stiffness of YIG films using broadband ferromagnetic resonance techniques'. In: *Journal of Physics D: Applied Physics* 48 (2015), p. 015001.

[Kli+17]   S. Klingler, H. Maier-Flaig, C. Dubs, O. Surzhenko, R. Gross, H. Huebl, S. T. B. Goennenwein and M. Weiler. 'Gilbert damping of magnetostatic modes in a yttrium iron garnet sphere'. In: *Applied Physics Letters* 110 (2017), p. 092409.

[Kli+18]   Stefan Klingler, Vivek Amin, Stephan Geprägs, Kathrin Ganzhorn, Hannes Maier-Flaig, Matthias Althammer, Hans Huebl, Rudolf Gross, Robert D. McMichael, Mark D. Stiles, Sebastian T. B. Goennenwein and Mathias Weiler. 'Spin-Torque Excitation of Perpendicular Standing Spin Waves in Coupled YIG/Co Heterostructures'. In: *Physical Review Letters* 120 (2018), p. 127201.

[KS86]   B. A. Kalinikos and A. N. Slavin. 'Theory of dipole-exchange spin wave spectrum for ferromagnetic films with mixed exchange boundary conditions'. In: *Journal of Physics C: Solid State Physics* 19 (1986), pp. 7013–7033.

[Kur+11]   H. Kurebayashi, O. Dzyapko, V. E. Demidov, D. Fang, A. J. Ferguson and S. O. Demokritov. 'Spin pumping by parametrically excited short-wavelength spin waves'. In: *Applied Physics Letters* 99 (2011), p. 162502.

[Lee+16]   Seongjae Lee, Scott Grudichak, Joseph Sklenar, C. C. Tsai, Moongyu Jang, Qinghui Yang, Huaiwu Zhang and John B. Ketterson. 'Ferromagnetic resonance of a YIG film in the low frequency regime'. In: *Journal of Applied Physics* 120 (2016), p. 033905.

[Lie21]   Lukas Liensberger. 'Magnon Hybrid Dynamics'. PhD-Thesis. 2021.

[Liu+19]   J. Liu, F. Feringa, B. Flebus, L. J. Cornelissen, J. C. Leutenantsmeyer, R. A. Duine and B. J. van Wees. 'Microwave control of thermal-magnon spin transport'. In: *Physical Review B* 99 (2019), p. 054420.

[LL65]   Landau and Lifshitz. 'On the Theory of the Dispersion of Magnetic Permeability in Ferromagnetic Bodies'. In: *Collected Papers of L.D. Landau*. Elsevier, 1965, pp. 101–114. ISBN: 978-0-08-010586-4.

[LW61]   R. C. LeCraw and L. R. Walker. 'Temperature Dependence of the Spin-Wave Spectrum of Yttrium Iron Garnet'. In: *Journal of Applied Physics* 32 (1961), S167–S168.

[Man+15]   S. A. Manuilov, C. H. Du, R. Adur, H. L. Wang, V. P. Bhallamudi, F. Y. Yang and P. C. Hammel. 'Spin pumping from spinwaves in thin film YIG'. In: *Applied Physics Letters* 107 (2015), p. 042405.

[Mar+11]   S. Marauska, T. Dankwort, H. J. Quenzer and B. Wagner. 'Sputtered thin film piezoelectric aluminium nitride as a functional MEMS material and CMOS compatible process integration'. In: *Procedia Engineering*. EurosensorsXXV 25 (2011), pp. 1341–1344.

[MD66]   R. Moskowitz and E. Della Torre. 'Theoretical aspects of demagnetization tensors'. In: *IEEE Transactions on Magnetics* 2 (1966), pp. 739–744.

[Moo06]   Gordon E. Moore. 'Cramming more components onto integrated circuits, Reprinted from Electronics, volume 38, number 8, April 19, 1965, pp.114 ff.' In: *IEEE Solid-State Circuits Society Newsletter* 11 (2006), pp. 33–35.

[Mor+11]   M. Morota, Y. Niimi, K. Ohnishi, D. H. Wei, T. Tanaka, H. Kontani, T. Kimura and Y. Otani. 'Indication of intrinsic spin Hall effect in 4 d and 5 d transition metals'. In: *Physical Review B* 83 (2011), p. 174405.

[Mos+10]   O. Mosendz, J. E. Pearson, F. Y. Fradin, G. E. W. Bauer, S. D. Bader and A. Hoffmann. 'Quantifying Spin Hall Angles from Spin Pumping: Experiments and Theory'. In: *Physical Review Letters* 104 (2010), p. 046601.

[Mül+21]   M. Müller, L. Liensberger, L. Flacke, H. Huebl, A. Kamra, W. Belzig, R. Gross, M. Weiler and M. Althammer. 'Temperature-Dependent Spin Transport and Current-Induced Torques in Superconductor-Ferromagnet Heterostructures'. In: *Physical Review Letters* 126 (2021), p. 087201.

[Pol49]   D. Polder. 'VIII. On the theory of ferromagnetic resonance'. In: *The London, Edinburgh, and Dublin Philosophical Magazine and Journal of Science* 40 (1949), pp. 99–115.

[RA90]   S. M. Rezende and F. M. de Aguiar. 'Spin-wave instabilities, auto-oscillations, and chaos in yttrium-iron-garnet'. In: *Proceedings of the IEEE* 78 (1990), pp. 893–908.

[Rub21]   Korbinian Rubenbauer. 'Spin Excitations in Nanostructures'. MA thesis. TUM, 2021.

[SA87]   C M Srivastava and R Aiyar. 'Spin wave stiffness constants in some ferrimagnetics'. In: *Journal of Physics C: Solid State Physics* 20 (1987), pp. 1119–1128.

[San+10]   C. W. Sandweg, Y. Kajiwara, K. Ando, E. Saitoh and B. Hillebrands. 'Enhancement of the spin pumping efficiency by spin wave mode selection'. In: *Applied Physics Letters* 97 (2010), p. 252504.

[San+11]   C. W. Sandweg, Y. Kajiwara, A. V. Chumak, A. A. Serga, V. I. Vasyuchka, M. B. Jungfleisch, E. Saitoh and B. Hillebrands. 'Spin pumping by parametrically excited exchange magnons'. In: *Phys Rev Lett* 106 (2011), p. 216601.

[San+17]   D Sander, S O Valenzuela, D Makarov, C H Marrows, E E Fullerton, P Fischer, J McCord, P Vavassori, S Mangin, P Pirro, B Hillebrands, A D Kent, T Jungwirth, O Gutfleisch, C G Kim and A Berger. 'The 2017 Magnetism Roadmap'. In: *Journal of Physics D: Applied Physics* 50 (2017), p. 363001.

[Sch+21]   Richard Schlitz, Sergey Granovsky, Darius Pohl, Andy Thomas, Bernd Rellinghaus and Sebastian T. B. Goennenwein. 'Nonlocal magnon-based transport in yttrium-iron-garnet–platinum heterostructures at high temperatures'. In: *Physical Review B* 103 (2021), p. 214434.

[Sch+22]   Matthias R. Schweizer, Alexander J. E. Kreil, Georg von Freymann, Burkard Hillebrands and Alexander A. Serga. 'Confinement of Bose–Einstein magnon condensates in adjustable complex magnetization landscapes'. In: *Journal of Applied Physics* 132 (2022), p. 183908.

[Sei+18] Tom S. Seifert, Samridh Jaiswal, Joseph Barker, Sebastian T. Weber, Ilya Razdolski, Joel Cramer, Oliver Gueckstock, Sebastian F. Maehrlein, Lukas Nadvornik, Shun Watanabe, Chiara Ciccarelli, Alexey Melnikov, Gerhard Jakob, Markus Münzenberg, Sebastian T. B. Goennenwein, Georg Woltersdorf, Baerbel Rethfeld, Piet W. Brouwer, Martin Wolf, Mathias Kläui and Tobias Kampfrath. 'Femtosecond formation dynamics of the spin Seebeck effect revealed by terahertz spectroscopy'. In: *Nature Communications* 9 (2018), p. 2899.

[Ser+14] A. A. Serga, V. S. Tiberkevich, C. W. Sandweg, V. I. Vasyuchka, D. A. Bozhko, A. V. Chumak, T. Neumann, B. Obry, G. A. Melkov, A. N. Slavin and B. Hillebrands. 'Bose-Einstein condensation in an ultra-hot gas of pumped magnons'. In: *Nat Commun* 5 (2014), p. 3452.

[SF96] F. Schreiber and Z. Frait. 'Spin-wave resonance in high-conductivity films: The Fe-Co alloy system'. In: *Physical Review B* 54 (1996), pp. 6473–6480.

[Sin+15] Jairo Sinova, Sergio O. Valenzuela, J. Wunderlich, C. H. Back and T. Jungwirth. 'Spin Hall effects'. In: *Reviews of Modern Physics* 87 (2015), pp. 1213–1260.

[Slo89] J. C. Slonczewski. 'Conductance and exchange coupling of two ferromagnets separated by a tunneling barrier'. In: *Physical Review B* 39 (1989), pp. 6995–7002.

[Suh57] H. Suhl. 'The theory of ferromagnetic resonance at high signal powers'. In: *Journal of Physics and Chemistry of Solids* 1 (1957), pp. 209–227.

[TBB02a] Y. Tserkovnyak, A. Brataas and G. E. Bauer. 'Enhanced gilbert damping in thin ferromagnetic films'. In: *Phys Rev Lett* 88 (2002), p. 117601.

[TBB02b] Yaroslav Tserkovnyak, Arne Brataas and Gerrit E. W. Bauer. 'Spin pumping and magnetization dynamics in metallic multilayers'. In: *Physical Review B* 66 (2002), p. 224403.

[Uch+10] K. Uchida, J. Xiao, H. Adachi, J. Ohe, S. Takahashi, J. Ieda, T. Ota, Y. Kajiwara, H. Umezawa, H. Kawai, G. E. W. Bauer, S. Maekawa and E. Saitoh. 'Spin Seebeck insulator'. In: *Nature Materials* 9 (2010), pp. 894–897.

[Wal16] M. Mitchell Waldrop. 'The chips are down for Moore's law'. In: *Nature News* 530 (2016), p. 144.

[Wan+17] T. Wang, W. Wang, Y. Xie, M. A. Warsi, J. Wu, Y. Chen, V. O. Lorenz, X. Fan and J. Q. Xiao. 'Large spin Hall angle in vanadium film'. In: *Scientific Reports* 7 (2017), p. 1306.

[Wei+22]   X.-Y. Wei, O. Alves Santos, C. H. Sumba Lusero, G. E. W. Bauer, J. Ben Youssef and B. J. van Wees. 'Giant magnon spin conductivity in ultrathin yttrium iron garnet films'. In: *Nature Materials* 21 (2022), pp. 1352–1356.

[Wei19]   Mathias Weiler. 'Magnetization Dynamics and Spin Torques in Exchange-Coupled Systems'. Habilitation. TUM, 2019.

[Wie+94]   G. Wiese, L. Buxman, P. Kabos and C. E. Patton. 'Parallel pumping fine structure at 9.4 GHz for in-plane magnetized yttrium iron garnet thin films'. In: *Journal of Applied Physics* 75 (1994), pp. 1041–1046.

[Wim+19a]   T. Wimmer, M. Althammer, L. Liensberger, N. Vlietstra, S. Geprägs, M. Weiler, R. Gross and H. Huebl. 'Spin Transport in a Magnetic Insulator with Zero Effective Damping'. In: *Physical Review Letters* 123 (2019), p. 257201.

[Wim+19b]   T. Wimmer, B. Coester, S. Geprägs, R. Gross, S. T. B. Goennenwein, H. Huebl and M. Althammer. 'Anomalous spin Hall angle of a metallic ferromagnet determined by a multiterminal spin injection/detection device'. In: *Applied Physics Letters* 115 (2019), p. 092404.

[Wim21]   Tobias Wimmer. 'Control and Manipulation of Magnonic Spin Currents in Magnetic Insulators'. PhD-Thesis. TUM, 2021.

[Wun+05]   J. Wunderlich, B. Kaestner, J. Sinova and T. Jungwirth. 'Experimental Observation of the Spin-Hall Effect in a Two-Dimensional Spin-Orbit Coupled Semiconductor System'. In: *Physical Review Letters* 94 (2005), p. 047204.

[Xia+10]   Jiang Xiao, Gerrit E. W. Bauer, Ken-chi Uchida, Eiji Saitoh and Sadamichi Maekawa. 'Theory of magnon-driven spin Seebeck effect'. In: *Physical Review B* 81 (2010), p. 214418.

[ZZ12a]   Steven S.-L. Zhang and Shufeng Zhang. 'Magnon Mediated Electric Current Drag Across a Ferromagnetic Insulator Layer'. In: *Physical Review Letters* 109 (2012), p. 096603.

[ZZ12b]   Steven S.-L. Zhang and Shufeng Zhang. 'Spin convertance at magnetic interfaces'. In: *Physical Review B* 86 (2012), p. 214424.

Acknowledgements
Danksagung

Im letzten Jahr, das geprägt war von vielen neuen Erkenntnissen und Erfahrungen, durfte ich in der Magnetiker-Gruppe des Walther-Meißner-Instituts (WMI) meine wissenschaftliche Grundausbildung abschließen. Ohne der großartigen Hilfe von so vielen Menschen wäre das alles nicht möglich gewesen. Insbesondere möchte ich mich bedanken bei:

- Prof. Dr. Rudolf Gross für das Vertrauen und die Möglichkeit, meine Masterarbeit am WMI anfertigen zu dürfen.

- Dr. Matthias Althammer für die Themenstellung und deine stets hilfreichen und einleuchtenden Erklärungen für alle Fragen theoretischer wie experimenteller Natur. Vielen Dank für deine Geduld, deine Hilfe bei den Messungen, bei der Interpretation der Daten und deine hilfreichen Anregungen zu dieser Arbeit.

- Dr. Hans Huebl für deine Beiträge zu den Diskussionen über meine Daten, die vor allem am Anfang nicht leicht zu interpretieren waren, sowie für deine Hilfe bei den Mikrowellenmessungen.

- Dr. Matthias Opel und Dr. Stephan Geprägs für die zahlreichen wissenschaftlichen Diskussionen nach Seminarvorträgen und im allwöchentlichen DC-Meeting.

- Manuel Müller für deine geduldige Hilfe, wenn ich mal wieder gar nicht weiter wusste, ob im Labor, im SUPERBOWL oder in der Theorie. Ohne deiner großartigen Hilfe wäre keine der Mikrowellenmessungen dieser Arbeit möglich gewesen. Außerdem natürlich auch für die zahllosen Kommentare beim Korrekturlesen dieser Arbeit.

- Janine Gückelhorn für die Einarbeitung in die Fabrikation und deine Hilfe bei den Magnontransport Messungen. Ohne deine Hilfe hätte ich keine einzige Probe herstellen und keine der ADMR-Messungen auswerten können.

- Korbinian Rubenbauer für die Diskussionen zu Theorie und Experiment, sowie vor allem für die Vorarbeit zu meinem Thema im Rahmen deiner Masterarbeit.

- Monika Scheufele für deine Hilfe in Rat und Tat, wenn die anderen Doktoranden gerade nicht da waren.